ALMA MATER STUDIORUM · UNIVERSITÀ DI BOLOGNA

DOTTORATO DI RICERCA IN
INGEGNERIA ELETTRONICA, TELECOMUNICAZIONI E
TECNOLOGIE DELL'INFORMAZIONE

CICLO XXX

Settore concorsuale: 09/E3
Settore scientifico disciplinare: ING-INF/01

Modeling and Characterization of Semiconductor Devices for Energy Efficiency

Presentata da: Massimo Nicolai

Coordinatore Dottorato
Prof. Alessandro Vanelli Coralli

Supervisore
Prof. Claudio Fiegna

Esame finale anno 2018

Abstract

Photovoltaics is among the most important technologies aimed at producing electrical energy from renewable and sustainable energy sources. Since the global photovoltaic market demands more and more efficient and cost-effective technologies, the photovoltaic research is driven by the need of investigating solar cell architectures in order to enhance the conversion efficiency guaranteeing, at the same time, low-cost manufacturing. As a matter of fact, a trade-off between production costs and conversion efficiency always exists. A comprehensive analysis of the different loss mechanisms which limit the photovoltaic energy conversion is extremely important in order to optimize costs per watt-peak. In this context, numerical device simulation allows understanding the link between new cell's architecture and physical structure, and the undelying physical mechanisms. Moreover, an advanced modeling may be suitable for identifying and analyzing promising solutions focused on the fulfillment of the photovoltaic market requirements.

This thesis aims at improving existing solar-cell simulation approaches and developing new ones. Furthermore, one of the challenges tackled by the presented work is to explain several behaviors revealed by the experimental characterization of different solar cell architectures (or concepts) and to provide useful findings to the industrial and experimental reasearch partners through an advanced numerical modeling.

This work, reports detailed simulation analyses performed on solar cell designs featuring different characteristics. Among them, the Emitter Wrap Through with Deep Grooved Base (EWT-DGB) solar cell is conceived for concentration photovoltaic applications, while both the well-known Passivated Emitter and Rear Cell (PERC) and the promising solar cell featuring passivated carrier-selective contacts are suitable for 1-sun illumination conditions.

In particular, this thesis provides the following contributions:

- the analysis of a new solar cell design conceived for low–medium concentrator photovoltaic applications, the EWT-DGB solar cell. Three-dimensional numerical simulations, calibrated starting from experimental data, are carried out to

investigate the performance under concentrated light and the potentials considering possible realistic improvements with respect to the fabricated devices;

- the role of top/rear poly-Si/SiO$_\mathrm{x}$ selective contact applied on front emitter silicon solar cells is investigated by means of simulation studies performed by using physical models calibrated on the basis of experimental data. A rear junction design which desensitizes the Fill Factor (FF) to top electrode resistivity is also proposed, addressing the possibility to omit the transparent conductive oxide (TCO) allowing promising conversion efficiency of silicon solar cells with carrier-selective contacts.

In the field of the modeling of advanced concepts applied on well-known high-efficiency solar cells, three different subtopics are considered:

- the impact of a rear point contact (RPC) scheme in metal wrap through (MWT) solar cells with passivated base adopting a modeling methodology which avoids cpu and memory intensive simulations of the whole true three-dimensional solar cell;
- the reproduction, through to a proper numerical simulations flow, of the experimental measured values of figures of merit (FOMs) of four different Cz-PERC solar cell lots subjected to a degradation and two regeneration processes, in order to study the well-known Light-Induced Degradation (LID) effect. In such study, the recombination centres in bulk and the Boron-Oxygen complexes (B-O) are modeled by means of two trap levels tuned on the basis of experimental data.
- electro-optical simulations of multi-wire (MW) and busbars (BBs) based solar cells in order to calculate the effective optical shading factor, the enhancement of conversion efficiency and the saving of contact-paste of the MW approach with respect to the BBs design. Specifically, by means of a ray-tracing simulation tool the significant impact of the front contact grid geometry, of the encapsulation layer thickness and of the optical properties of the cell front interface on the effective optical shading are studied;

List of publications

Peer-Reviewed Journal Papers

M. Nicolai, M. Zanuccoli, P. Magnone, D. Tonini, E. Sangiorgi and C. Fiegna. Theoretical study of the impact of rear interface passivation on MWT silicon solar cells. *Journal of Computational Electronics*, v. 15, pp. 277-286, 2016.

G. Paternoster, **M. Nicolai**, G. de Ceglia, M. Zanuccoli, P. Bellutti, L. Ferrario, E. Sangiorgi, and C. Fiegna. Fabrication, simulation and experimental characterization of EWT solar cells with Deep Grooved Base contact. *IEEE Journal of Photovoltaics*, v. 6, pp. 1072-1079, 2016.

M. Nicolai, G. Paternoster, M. Zanuccoli,G. de Ceglia, P. Bellutti, L. Ferrario, E. Sangiorgi and C. Fiegna. Analysis of the EWT-DGB solar cell at low and medium concentration and comparison with a PESC architecture. *Progress in Photovoltaics: Research and Applications*, v. 25, pp. 417-430, 2017.

M. Nicolai, M. Zanuccoli, F. Feldmann, M. Hermle, and C. Fiegna. Analysis of silicon solar cells with poly-Si/SiO$_\mathrm{x}$ carrier-selective base- and emitter-contacts. *IEEE Journal of Photovoltaics*, v. 8, pp. 103-109, 2018.

International Conferences

Poster Presentations by the Author Including Refereed Conference Papers

M. Nicolai, M. Zanuccoli, P. Magnone, M. Galiazzo, D. Tonini, M. Bertazzo, E. Sangiorgi and C. Fiegna. Simulation Study of Multi-wire front Contact Grids for Silicon Solar Cells. *Energy Procedia*, v. 77, pp. 129-138, 2015.

M. Nicolai, M. Zanuccoli, M. Galiazzo, M. Bertazzo, E. Sangiorgi and C. Fiegna. Simulation Study of Light-induced, Current-induced Degradation and Recovery on PERC Solar Cells. *Energy Procedia*, v. 92, pp. 153-159, 2016.

M. Nicolai, M. Zanuccoli, G. Paternoster, G. de Ceglia, L. Ferrario, P. Bellutti, E. Sangiorgi and C. Fiegna. Numerical Simulation and Experimental Characterization of Emitter Wrap through Solar Cells with Deep Grooved Base Contact (EWT-DGB). *Energy Procedia*, v. 92, pp. 160-169, 2016.

F. Feldmann, **M. Nicolai**, R. Müller, C. Reichel and M. Hermle. Optical and electrical characterization of poly-Si/SiO$_x$ contacts and their implications on solar cell design. *Energy Procedia*, v. 124, pp. 31-37, 2017.

Contents

Chapter 1

Introduction, goals and motivation to the research activity

The unceasing growth of the use of renewable and sustainable energy sources and the challenge of reducing environmental pollution from fossil-fuel energy systems mainly stem from the continuous increase in power needs. Among the technologies aimed at producing electrical energy from "zero-carbon" energy sources, the photovoltaic (PV) technology represents a massive pillar. Such technology exploits the basic process, called photovoltaic effect, in which sunlight is converted into electricity.

The considerable technical progress achieved so far, along with scaling effects of mass production, have led to a reduction in the levelized cost of electricity from PV, resulting in a global growth of this market.

In 2016, a global power generation close to 2500 TWh was reported [1], with a worldwide PV power consumption of 333 TWh [2] and a cumulative PV installed capacity of 306.5 GW [3]. Morevoer, the Fraunhofer Institute for Solar Energy Systems (Fraunhofer ISE) reported a compound annual growth rate (CAGR) of 40% in PV installations from 2010 to 2016 [2]. Fig. 1.1(a) illustrates the percentage of cumulative photovoltaic plant installations in 2016 for the different countries reported. It is possible to observe that although China (23%), the USA (14%), and Japan (14%) lead the global PV installations, some European states do not lag far behind. In particular, Germany's contribution (13%) almost equals that of the USA and Japan, while Italy (6%) plays a moderate role. Furthermore, up-to-date forecasts of the expected investments in zero-fossil energy sources for 2017–2040 predict that solar energy sources will receive significant attention. In this regard, Fig. 1.1(b) displays the estimated data published by Bloomberg New Energy Finance [4]. The global PV market constantly demands more efficient and cost-effective technology. Several materials and technologies have been proposed by the PV community in an

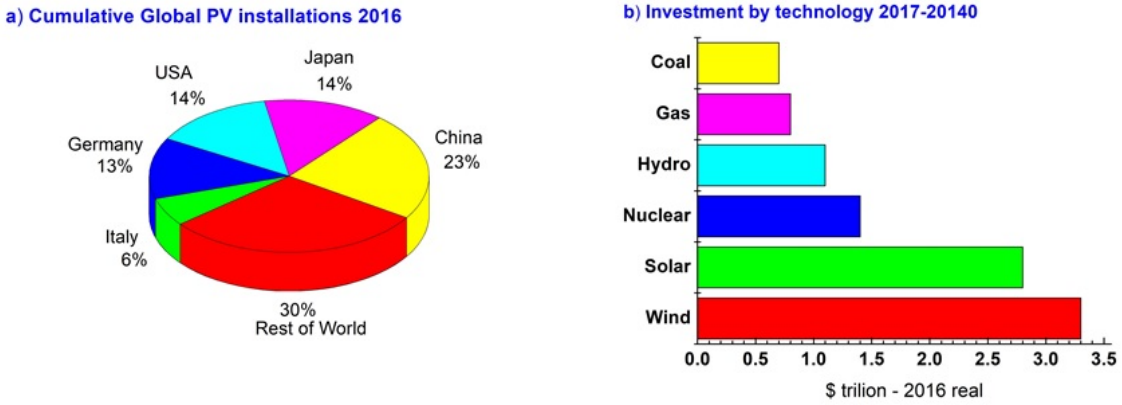

Figure 1.1: Percentage of cumulative global PV installations for 2016 (a) and expected investment by type of technology for 2017–2040 (b) [4].

attempt to continually increase performance. The conversion efficiency (at research-cell level) chart published by the National Renewable Energy Laboratory (NREL) [5] and depicted in Fig. 1.2 clearly presents the continuous performance improvements of a wide spectrum of PV technologies. Although recently the adoption of new materials is an attractive topic of the PV research community (Fig. 1.2 reports also the performance achieved by "emerging PV" technologies), silicon-based solar cells still represent the technology most widely used in PV, with a market share of around 93% in 2016 [2]. Among them, crystalline silicon (c-Si) solar cells cover a

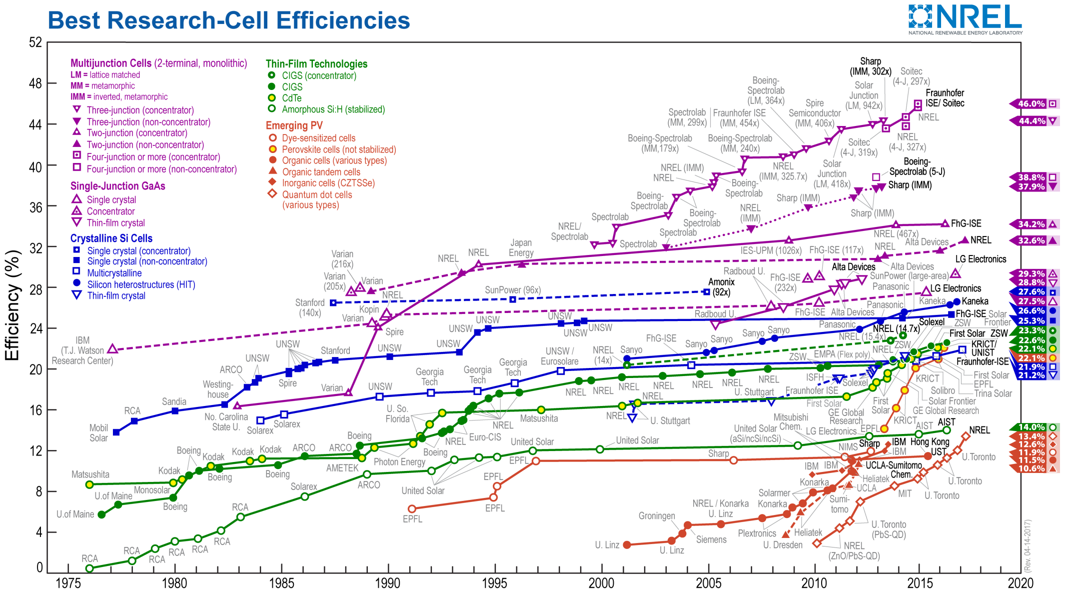

Figure 1.2: Best research-cell efficiency chart published by the NREL in 2017 [5].

significant percentage thanks to their considerable conversion efficiency obtainable limiting the costs of generated power. On the contrary, thin-film technologies present a lower conversion efficiency and a significantly reduction of their large-scale use. A summary of the record efficiencies obtained at laboratory level for silicon-based solar cells is reported in Fig. 1.3, which plots the data published by Green et al. [6]. It is worth noting that the conversion efficiency record for c-Si-based solar cell is 26.7% and was obtained by Kaneka [7].

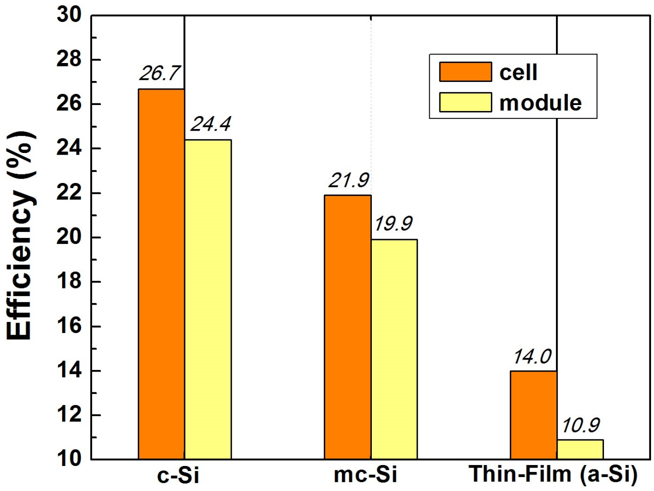

Figure 1.3: Record efficiencies at a cell level (orange) and at a module level (light yellow) for silicon-based solar cells. (Data from [6]).

During the last decads, the PV community has been driven by the goal of reducing the cost-per-watt ratio in order to make PV an increasingly competitive technology. In order to reach this objective, focalizing and working at cell level is essential, since this single device is where the photoelectric conversion occurs and, in addition, it involves the main part of the overall cost [8].

In the light of this, the identification and the analysis of promising high-efficiency solar cell architectures by reducing time and cost efforts represent a key factors of PV research. To this aim, numerical simulations of solar cells play a fundamental role. The ability of accurately describe the electrical performance and the physical mechanisms of a solar cell by means of an advanced numerical modelling may lead to valuable indications useful for the design of the device. Furthermore, the adoption of novel physical concepts and the development of studies focused on further improving existing, often non-optimized, technical solutions may result feasible tasks.

In recent years, by exploiting the countinous improvements in terms of computing availability, solar cell modelling has become one of the most attractive topics of the PV research field.

1.1 Objective of this Thesis

This work concerns the activities performed during the three-years Doctorate programme.

The objective of this thesis is to provide a contribution to the PV research by mainly focusing on the modelling of advanced silicon solar cells. In particular, this work proposes numerical simulations studies aimed at providing an overall understanding of several solar cell designs and concepts, conceived to improve the conversion efficiency. All the simulation results have been obtained with a state-of-the-art Technology Computer Aided Design (TCAD) simulator (Sentaurus tool) by using up-to-date physical models [9], [10] and by efficiently handling one-, two- and three-dimensional geometries (1-D, 2-D and 3-D, respectively).

The presented simulation activities were developed in continuous interaction with the experimental ones. In fact, the calibration of the physical and electrical models adopted in the simulations, typically obtained by comparing simulated and experimental results, is extremely important for the successful usage of the modelling approach. In addition, an accurate and predictive modelling may also represent an useful guideline for the technological and manufacturing part, leading to a time reducing and otherwise unavoidable cost efforts. These are the reasons why the totality of the studies reported in this thesis have been undertaken in close collaboration with different technological partners that have provided results of the experimental characterization of the solar cells under investigation.

One example is the 3-D simulation setup discussed in Chapter 4, performed in order to study the Emitter Wrap Through solar cell with Deep Grooved Base (EWT-DGB), which was conceived and fabricated by Fondazione Bruno Kessler (FBK, Trento, Italy). In such case, numerical simulations provide useful information on the impact of the main available technological options, as well as a detailed analysis of the potentialities of such solar cell under concentrated light, underlying the main differences respect to a simpler PESC structure.

In collaboration with Fraunhofer ISE's Department of Characterization and Modeling of silicon Solar Cells (Freiburg, Germany) an advanced modelling has been carried out in order to enable the investigation of the carrier transport governed by tunneling mechanisms, which comes into play in Solar Cells featuring tunneling carrier-selective contacts. The results of such activities are reported in Chapter 5. The main interesting finding is that solar cell featuring both base- and emitter-selective contact adopting a rear junction (RJ) design are able to desensitize the FF to the resistivity of the top electrode.

Promising concepts that aim to improve the performance of standard high-efficiency solar cells have been successfully analyzed in Chapter 6, by means of numerical simulations based on experimental data provided by Applied Materials Italia s.r.l. (San Biagio di Callalta, Italy).

To summarize, the following topics have been studied: i) modeling of the rear point contact (RPC) concept applied on Metal Wrap Through (MWT) solar cells by significantly reducing the computational effort; ii) electrical analyses aimed at understanding and properly reproducing light-induced and current-induced degradation (LID-CID) effects on PERC solar cells; iii) studies of PERC solar cells featuring an alternative front-grid pattern composed of ribbon multi-wires in order to evaluate possible optical advantages.

1.2 Thesis outline

The thesis is organized as follows.

Chapter 2 discusses the basis of the PV effect and the main features of a standard solar cell, such as the figures of merit (FOMs) and recombination mechanisms. Moreover, an overview of advanced silicon-based solar cell schemes, of innovative concepts and of the concentrator photovoltaic is introduced.

Chapter 3 presents the basic concepts of numerical simulation of silicon-based solar cells. The main optical and electrical methods adopted in the studies addressed in the subsequent chapters are also reported.

Chapter 4 introduces the EWT-DGB solar cell, manufactured by Fondazione Bruno Kessler (FBK) and conceived for concentration photovoltaic (CPV) applications. An advanced 3-D numerical modelling of this solar cell is implemented, and the results are compared to the experimental data. Moreover, the performance of the EWT-DGB solar cell and its potential under concentrated light are investigated by means of numerical simulations that demonstrate its improved sensitivity to the substrate quality and resistivity respect to a standard Passivated Emitter Solar Cell.

In Chapter 5 a solar cell design with poly-Si/SiO_x contacts at both the top and rear sides is investigated by starting from experimental results provided by Fraunhofer ISE. Thanks to an opportunely calibrated simulation flow, a rear junction approach is deeply analyzed as well as the influence of the effective tunneling mass values adopted in the simulation.

Finally, Chapter 6 outlines three simulation studies aimed at analyzing some promising architectures for silicon solar cells: the implementation of a rear point contact design on Metal Wrap Through (MWT) solar cells (section 6.1), the understanding of the LID-CID effect due to the activation of B-O complexes occuring in Passivated Emitter Rear Contact (PERC) solar cells (section 6.2), and the adoption of ribbon multi-wires instead of silver busbars as front contact grid (section 6.3).

1. INTRODUCTION, GOALS AND MOTIVATION TO THE RESEARCH ACTIVITY

Chapter 2

Solar Cells: operating principles and state-of-the-art

After introducing the basis of the PV effect, this chapter reports the fundamental equations that describe this phenomenon. In addition, it describes the operating principles of a standard solar cell and the meaning of the so-called figures of merit (FOMs). The principal loss mechanisms, such as recombination losses, optical and electrical losses, are discussed thereafter. Lastly, an overview of advanced silicon-based solar cell schemes, of innovative concepts and of the concentrator photovoltaic is proposed so as to provide the basic concepts needed to understand the studies outlined in this thesis.

2.1 Photovoltaic effect

A solar cell may be defined as a device whereby solar radiation is converted into electrical energy. This thesis only considers silicon-based solar cells; however, the basic operating principle is the same for all possible semiconductor materials.

The PV process can be summarized in three main mechanisms, without which energy conversion cannot occur: i) interaction between solar radiation and the absorber material; ii) generation of free electron-hole pairs (photogenerated carriers) through the excitation of electrons over the band-gap; and iii) separation of the photogenerated carriers and their transport toward the external circuit.

The PV effect is among the phenomena described by the corpuscular property of light. Indeed, a photon provides the energy required to activate the conversion. Concerning the last two mechanisms previously listed, relevant to charge carriers, the properties of the material exposed to solar radiation are fundamental. Both the creation of (photogenerated) charge carriers and their separation are possible,

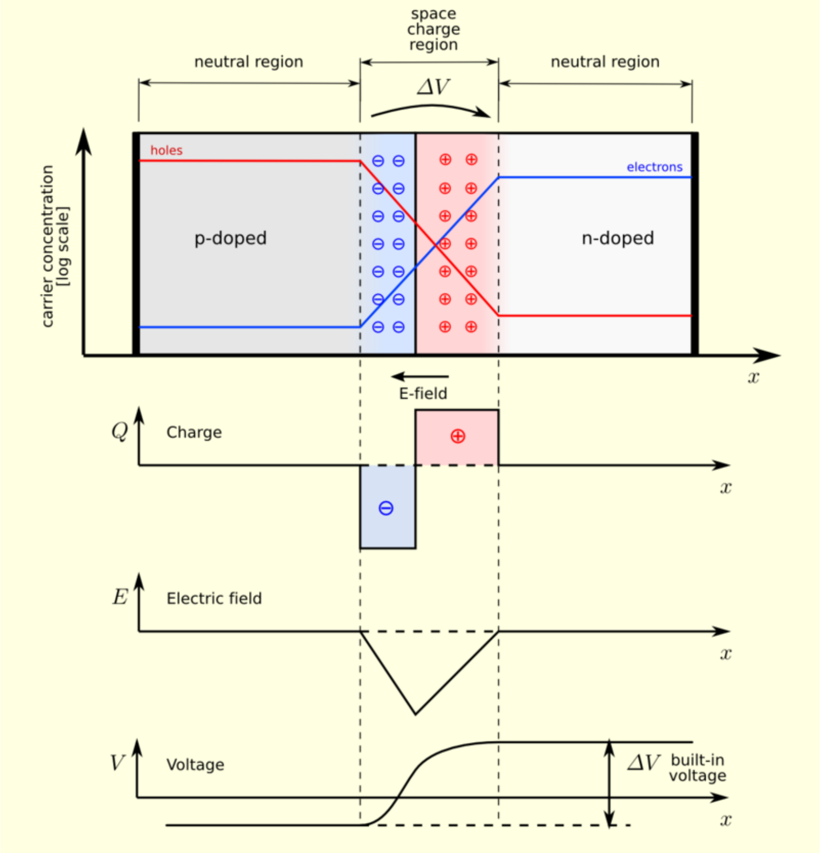

Figure 2.1: Example of pn-junction in thermal equilibrium with zero-bias voltage applied and related plots of charge density, electric field and voltage.

typically by exploiting local asymmetries (e.g. the pn-junction [11], Fig. 2.1), to guarantee their collection and thus a source of electrical energy through metal electrodes.

In order to ensure an adequate design of a PV device it is extremely important to know the properties of the solar energy incident on it. Although the maximum solar radiated power is approximately 170 PW, the resulting energy flux is more diluted and intermittent. In facts, the radiation incident on the Earth's surface is not constant, since the result depends strongly on several effects, such as absorption mechanisms or scattering, that arise from its passage through the atmosphere. Moreover, the solar radiation incident changes depending on the latitude, the seasons and the time of the day.

To better understand the solar energy spectrum, the path through which sunlight hits the Earth's surface has to be studied. Such a path is commonly denoted as air mass (AM). Generally, the solar radiation spectrum measured at one point of the Earth's surface is related to the AM specific for such point (Fig. 2.2). When the

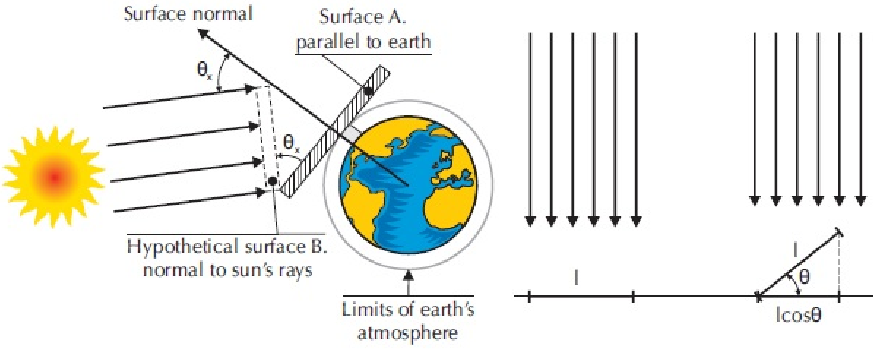

Figure 2.2: Sketch of the cosine effect. More details can be found in [11].

angle created by the sun respect to the zenith is 0° and 60°, the AM is defined as AM1 and AM2, respectively. Furthermore, the spectrum measured in space, outside the atmosphere, is indicated as AM0. The standard irradiance condition for PV tests is AM1.5, which corresponds to latitude 48.2º. As previously stated and as illustrated in Fig. 2.3, the radiation for particular wavelengths at AM1.5 is affected by a scattering phenomenon due to the presence of particles such as oxygen, carbon dioxide, carbon, ozone and water vapor within the Earth's atmosphere [12].

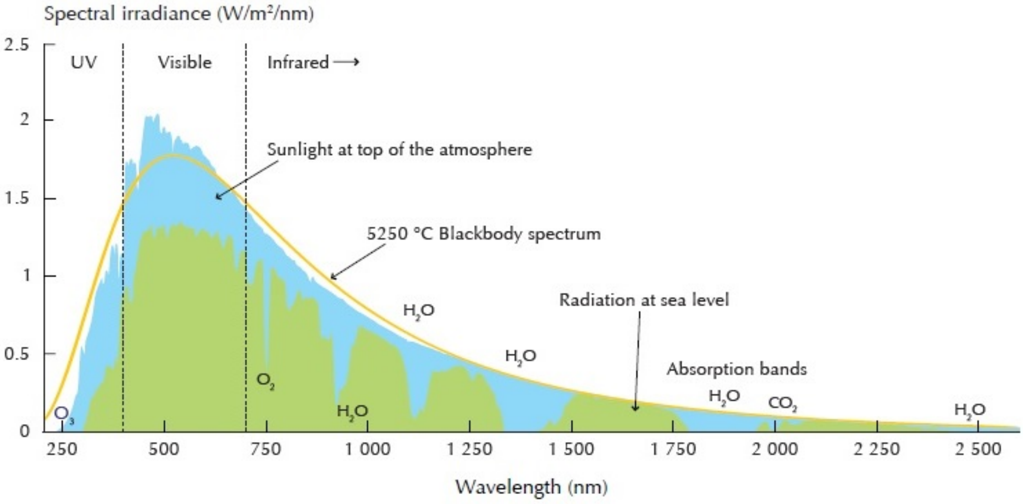

Figure 2.3: Example of the solar spectrum [12].

Considering the entire spectrum, the charge carriers inside the device are photo-generated by the wavelength referred to as the visible part of the spectrum. This is ascribed to an energetic balance. In fact, in order to study the effect of the interaction between sunlight and a material, it is necessary to recall the Plank's law.

The energy E of the solar radiation can only assume discretized or quantized values, multiple of Plank's constant $h = 6.626 \cdot 10^{-34}$ J·s.

$$E = h\nu \tag{2.1}$$

Given the relationship between frequency ν and wavelength λ:

$$\lambda = \frac{c}{\nu} \tag{2.2}$$

where $c = 3 \cdot 10^8$ m/s, the conclusion is that energy and wavelength are inversely proportional to each other:

$$\lambda = \frac{hc}{E} \tag{2.3}$$

For silicon light absorber, photons in the range of 300 - 1200 nm are responsible for generating charge carriers (electron-hole pairs, photogenerated carriers).

2.1.1 Fundamental equations for the photovoltaic conversion analysis

The physical and electrical behavior of the most common semiconductor devices, in particular solar cells, can be described by a set of equations. This section only describes one-dimensional (1-D) cases. The relative three-dimensional (3-D) equations can be obtained by introducing the divergence operator for the vector quantities and the gradient operator for the scalar ones.

2.1.1.1 Poisson's equation

The 1-D form is expressed as:

$$\frac{\partial E}{\partial x} = \frac{\rho}{E} \tag{2.4}$$

Equation (2.4) allows us to relate the divergence of the electric field E with the local carrier density ρ. For each given unit of volume, the carrier density in a semiconductor can be described by the relationship:

$$\rho = q\big(p - n + N_D^+ - N_A^-\big) \tag{2.5}$$

where $N_D{}^+$ and $N_A{}^-$ represent the ionized donor and acceptor concentrations, respectively. At room temperature, impurities are almost totally ionized; the following relationships are therefore valid:

$$N_D^+ \approx N_D, \qquad N_A^- \approx N_A \tag{2.6}$$

2.1.1.2 Current density equation

The flux of the current inside the semiconductor is mainly ascribed to effects such as the diffusion mechanism and transport governed by the electric field. By considering these two mechanisms simultaneously, for electrons (J_e) and holes (J_h), we obtain:

$$J_e = q\mu_e nE + qD_n\frac{\partial n}{\partial x}, \quad J_h = q\mu_h pE + qD_p\frac{\partial p}{\partial x}, \tag{2.7}$$

where the mobility μ and the diffusion constant D are related to the Einstein's equations:

$$D_e = \left(\frac{kT}{q}\right)\mu_e, \quad D_h = \left(\frac{kT}{q}\right)\mu_h \tag{2.8}$$

with k the Boltzman's constant of $8.617 \cdot 10^{-5}$ eV·K^{-1}.

2.1.1.3 Continuity equation

Given a volume element featuring a length x and a section area A, the continuity equation establishes that a variation in terms of the electron concentration within such a volume is determined by the sum of two differences. The first one is the difference between the electrons penetrating the element and those escaping it. The second one is the balance between the electrons generated inside the volume and the loss of electrons via recombination. For the electrons, by indicating with G the optical generation rate and with U the recombination rate, we obtain the following equation:

$$\frac{\partial n}{\partial t} = -\frac{1}{q}\frac{\partial J_e}{\partial x} + U - G \tag{2.9}$$

by adopting the same approach for the holes, we obtain:

$$\frac{\partial p}{\partial t} = -\frac{1}{q}\frac{\partial J_h}{\partial x} + G - U \tag{2.10}$$

2.2 Solar cells: operating principles

As reported in section 2.1, semiconductor-based solar cells are devices described as a simpler pn-junction. Fig. 2.4 illustrates a classical scheme of a silicon-based solar

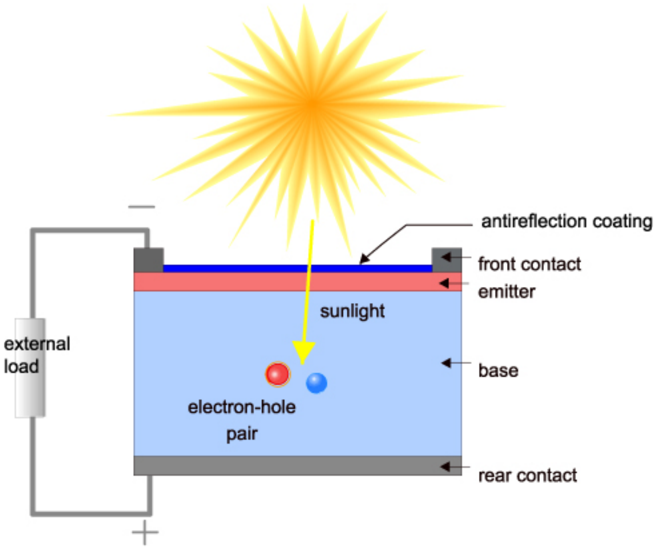

Figure 2.4: Sketch of a cross section of a typical solar cell, from [13].

cell. The light absorber region (the base in Fig. 2.4, of c-Si material in this work) and the emitter region are alternatively doped in order to create the pn-junction that separates the photogenerated carriers (Fig. 2.1). Such carriers (free electrons and holes) have to be collected at the contacts, avoiding (or at least limiting) the recombination mechanisms that take place. In fact, as discussed in detail afterwards, it is necessary to take into account for the presence of several mechanisms that compete with the generation of free carriers. The system, once externally disturbed by solar radiation, tends to reach an equilibrium state, by recombining a free electron with a free hole. However, this effect reduces the availability of free carriers, which must therefore be collected at the electrodes to create an electrical current before recombining them.

2.2.1 Anti-reflection coating and light trapping techniques

In order to increase the absorption within the light absorber, solar cells typically feature an anti-reflective coating (ARC) layer composed by one or more dielectric materials (e.g. $\mathrm{SiN_x}$, $\mathrm{SiO_2}$, MgF, $\mathrm{Al2O_3}$) of thickness properly chosen to reduce the amount of reflected rays. In fact, in addition to its excellent passivation properties (the surface recombination velocity (SRV) at the ARC/Si interface is significantly lower than the SRV at the metal/Si interface), by adopting an ARC the reflectance at the external interface can be markedly minimized. These layers and their interference effects lead to a phase shift between the wave reflected from the ARC and thae wave reflected from the semiconductor surfaces. When the destructively interference between the two waves occurs, a null reflected energy may be obtained.

Light trapping techniques are aimed at maximizing the optical path within the absorbing material. One of the most common example of light trapping technique is a back reflector, typically a back aluminum plate, which is able to redouble the optical path.

Furthermore, advanced solar cells present a properly texturized interface morphology. Texturing increases the light absorption in the cell due to the different scattering angles and multiple reflection of light obtained by exploiting the pyramidal morphology feature of the interface (Fig. 2.5). It is worth reporting that due to technological limitation, 3-D pyramids are not regular but their dimensions and positions are typically randomly distributed.

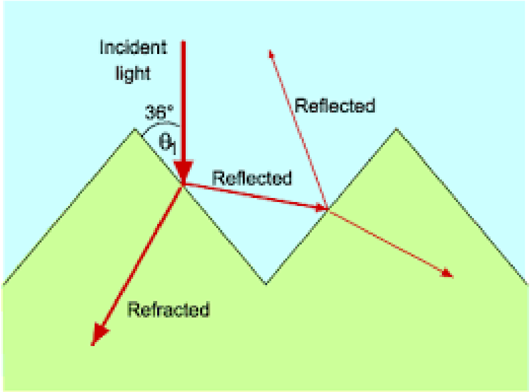

Figure 2.5: Reflection and transmission of light for a textured silicon solar cell [13].

The front metallization scheme is worth discussing. It should be noted that a trade-off exists between the series resistance introduced by the front metal contact and the optical shading that occurs due to the metal coverage. In this work, section 6.2 reports detailed simulation studies of an interesting front scheme option, composed of ribbon multi-wire instead of silver busbars

Photovoltaic research is based on reducing the energy losses of PV devices in order to achieve higher conversion efficiency. Solar cells are commonly distinguished and evaluated through such a value. However, there are other quantities that enable the identification of solar cell performance after a characterization: the so-called figures of merit (FOMs). It is worth noting that these quantities are strictly related to several mechanisms, as discussed in the following.

2.2.2 Electrical figures of merit (FOMs)

Solar cell FOMs are obtained from a current-voltage (IV) characterization (represented by an IV curve) typically performed under standard conditions: Temperature

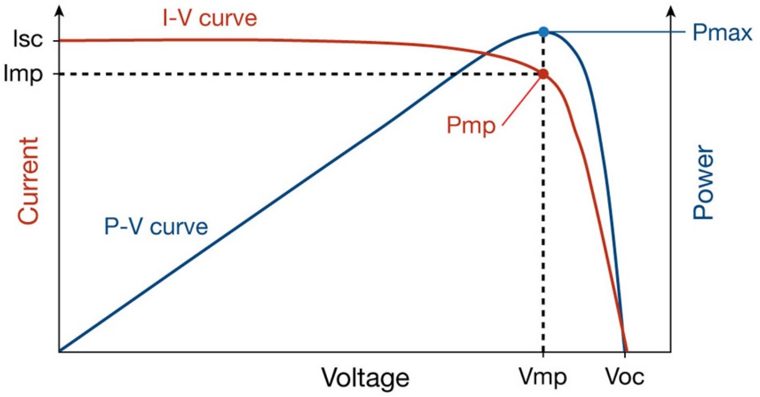

Figure 2.6: Current density-voltage curve of a solar cell under 1-sun illumination. The corresponding maximum power point (MPP) is reported as well.

T of 25 °C and assuming the AM1.5G global standard solar spectrum (described in section 2.1). An example of a IV curve is presented in Fig. 2.6. The figure including the current density curve (red), is completed by plotting the power density curve (blue), which highlights the maximum power point (MPP). The following FOMs may be identified by the IV curve:

- **Short circuit current** I_{SC}, ideally equal to the photogenerated current I_{PH}

- **Open circuit voltage** V_{OC}, described by the equation:

$$V_{OC} = \frac{kT}{q} \ln \left(\frac{I_{SC}}{I_0} + 1 \right) \tag{2.11}$$

  where k is the Boltzman's constant of $8.617 \cdot 10^{-5}$ eV·K^{-1}, T is the temperature and q is the unitary carrier, and I_0 is the saturation current. The V_{OC} value is ascribed to the properties of the semiconductor due to its dependence on I_0. The maximum generated power occurs at the MPP of the coordinates (V_{mp}, I_{mp}).

- **Fill Factor** FF, defined by:

$$FF = \frac{V_{mp} I_{mp}}{V_{OC} I_{SC}} \tag{2.12}$$

  indicates how "squared" is the IV curve, i.e. how it is similar to the maximum power condition. The FF of a high-efficiency solar cell is in the range of 81% - 85% and, theoretically, is a function of only V_{OC}. By defining a normalized voltage $v_{oc} = \frac{V_{OC}}{\frac{kT}{q}}$, the ideal FF (maximum) value is calculated as:

$$FF = \frac{v_{oc} - \ln v_{oc} + 0,72}{v_{oc} + 1} \tag{2.13}$$

It is worth reporting that FF value is strongly dependent on the series resistance, as will be discussed in section 2.3.3.

- **Conversion efficiency** η:

$$\eta = \frac{V_{mp} I_{mp}}{P_{in}} = \frac{V_{OC} I_{SC} FF}{P_{in}} \tag{2.14}$$

where P_{in} is the power under conditions of total illumination on the cell.

In [14] the Shockley-Queisser theoretical efficiency limit for a solar cell with a single pn-junction comprising by a semiconductor is expressed. The maximum value of 32% is reported in case of only radiative recombination (the most important recombination mechanisms are presented in section 2.3) for a silicon-solar cell under standard conditions.

Nowadays, the current record of efficiency for silicon solar cells is of 26.7%, reached by Kaneka [7], who developed an Interdigitated Back Contact (IBC) solar cells featuring a carrier-selective contacts, as discussed in section 2.4.

2.2.2.1 Series resistance

Several factors are responsible for the total parasitic resistance of a solar cell, considering the back-contact resistance (metal-semiconductor interfaces) and the front surface contribution ($\mathrm{R_{s,fr}}$). When metal is deposited on a highly-doped semiconductor, the contact is usually considered as ohmic contact. On the contrary, when semiconductor is lowly doped, the thermionic effect is the only cause of a charge carrier transfer toward the contact. For a front metal grid featuring fingers, L_T represents the transport length and R_{SH} the sheet resistance of the contacted semiconductor. The resistance of the front contact, extremely important because of the lateral conduction in the front region, can be obtained by:

$$R_{s,fr} = \frac{\sqrt{R_{SH}\rho_C}}{L} coth\left(W\sqrt{\frac{R_{SH}}{\rho_C}}\right) \tag{2.15}$$

where ρ_C is the contact resistivity, W is the finger width and L the finger length. Fig. 2.7 shows a representation of the several series resistance contributions (including that one ascribed to the front contact) and the current path inside the device. In

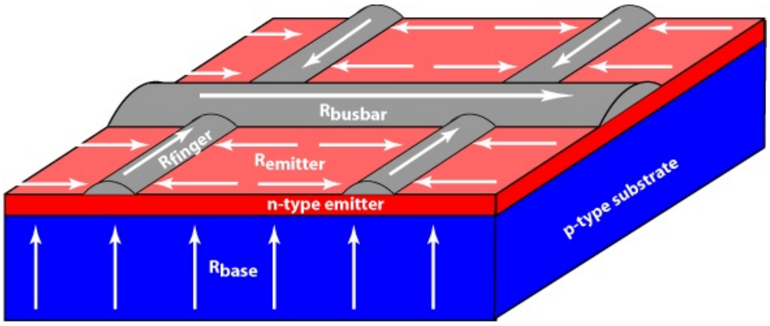

Figure 2.7: Schematic representation of series parasitic resistance contributions and of the current path.

the case of $L_T > 2W$, then:

$$R_{s,fr} = \frac{\rho_C}{L_T} = \frac{\sqrt{\rho_C R_{SH}}}{L} \tag{2.16}$$

If $L_T < 2W$, 2.16 can be approximated as:

$$R_{s,fr} = \frac{\rho_C}{LW} \tag{2.17}$$

The resistance $R_{s,fr}$ is not affected by the value of W when $L_T \leqslant 0.5W$. In addition to $R_{s,fr}$, the finger resistance R_{finger} has to be taken into account for [15]:

$$R_{finger} = \frac{1}{3}\rho_m \frac{L}{HW} \tag{2.18}$$

defining H as the finger height and ρ_M as the metal resistivity. The resistance introduced by the busbar R_{bus} can be furthermore expressed by [15]:

$$R_{bus} = \frac{1}{6}\frac{L_B}{H_B W_B}\rho_m \tag{2.19}$$

where L_B, H_B and W_B denotes the busbar length, height and width, respectively. The above-mentioned contributions, are those typically included as post-processing. As illustrated in Fig. 2.7, there are other series resistance contributions worthy of mentioning such as the base resistance (R_{base} or R_{bulk}), the emitter sheet resistance (R_{SH} or $R_{emitter}$) and the resistance of the bottom-side contact. In particular, R_{base} and R_{SH} are obtained by the following equations:

$$R_{base} = \rho_S T, \qquad R_{SH} = \frac{\rho_{e,S}}{t_e} \tag{2.20}$$

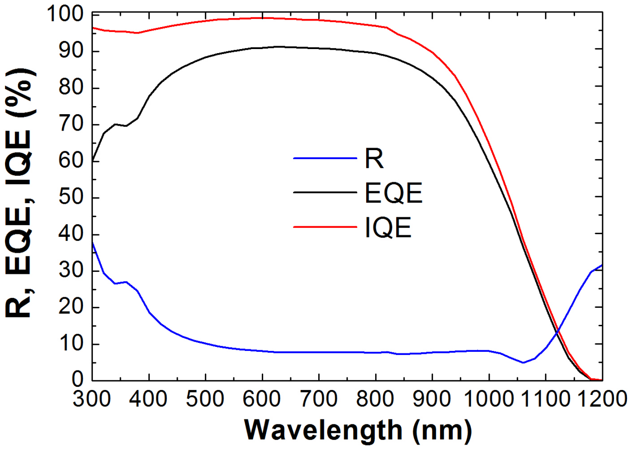

Figure 2.8: Example of Reflectance (R), External (EQE) and Internal (IQE) Quantum efficiency.

where ρ_S and T denote the substrate reistivity and the substrate thickness, respectively, whereas $\rho_{e,S}$ and $t_{e,S}$ refer to the resistivity and the thickness of the emitter region.

2.2.3 External and internal quantum efficiency

An important feature of solar cells is the capability of converting as many photons as possible into carriers. This property is identified by the external quantum efficiency *EQE(λ)*. Indeed, EQE is calculated as the ratio of the number of carriers contributing to the current in short-circuit conditions to the number of incident photons. Defining the input irradiance as I_0 and the incident power flux as $\phi(\lambda)$:

$$\phi(\lambda) = \frac{I_0(\lambda)}{E_{ph}(\lambda)} = \frac{I_0(\lambda)}{\frac{hc}{\lambda}} \tag{2.21}$$

assuming the energy of the photon $E_{ph}(\lambda)$, the Plank's constant h and the speed of light c. N_{INC} (number of incident photons) is obtained by the multiplication of ϕ with the area of the solar cell device A. Therefore,

$$EQE(\lambda) = \frac{J_{sc}(\lambda)}{qN_{INC}(\lambda)} = \frac{J_{sc}(\lambda)}{q\phi(\lambda)} = \frac{J_{sc}(\lambda)}{J_{IN}(\lambda)} \tag{2.22}$$

At the same time, the internal quantum efficiency IQE(λ) relates to the property of collecting the carriers photogenerated in the semiconductor into the I_{SC}. In detail, IQE(λ) is expressed as:

$$IQE(\lambda) = \frac{EQE(\lambda)}{1 - R(\lambda)} \tag{2.23}$$

Moreover, the collection efficiency η_C of the photo-generated carriers can be calculated as:

$$\eta_C(\lambda) = \frac{J_{sc}(\lambda)}{J_{ph}(\lambda)} \tag{2.24}$$

Fig. 2.8 depicts an example of the R, EQE and IQE curves.

Each carriers recombination meachanism leads to a reduction of η_C. In the next section, the main recombination mechanisms are presented and explained in order to better understand the basic concepts of such limiting mechanisms.

2.3 Main loss mechanisms in solar cells

As reported in the previous section, recombination mechanisms contribute significantly to the electrical losses. Recombination is conceived as a mechanism that competes with the generation where, basically, free electrons and holes recombine, reducing the amount of carriers able to reach the electrodes. Recombination mechanisms, however, are not the only loss mechanisms that take place in solar cells. In this section, the most significant loss factors are presented.

2.3.1 Recombination mechanisms

2.3.1.1 Auger recombination

The Auger recombination can be thought as the reverse of the impact ionization [11]. An electron, which recombines with a hole, gives its energy to another electron. This second electron releases its energy in the form of a phonon emission (energy loss) and returns to its starting energy level. The Auger recombination rate is strictly dependent on the doping concentration of the material of the semiconductor involved; in this thesis, silicon. Moreover, particular attention is therefore required for the design of the emitter or other heavily doped regions. Mathematically, the Auger recombination is described by the following equation:

$$R_{AUG} = (C_n n - C_p p)(np - n_i^2) \tag{2.25}$$

where C_n and C_p are specific parameters for the material involved and n_i is the intrinsic carrier density concentration.

2.3.1.2 Radiative recombination

The radiative mechanism may be defined as the opposite of the (photo)generation effect. To better understand, in such a case, an electron from the conduction band returns to the valence band losing its energy by emitting a photon that features an energy related to the energy gap of the electron transition. The radiative recombination rate is expressed as:

$$R_{rad} = Bnp \tag{2.26}$$

where B refers to a property of the semiconductor involved, n denotes the concentration of electrons and p that of holes. In the case of silicon-based solar cells, since the light absorber material is an indirect band-gap material, the radiative contribution can be considered negligible. Considering a thermal equilibrium case (np = $n_{\mathrm{i}}{}^2$), under dark conditions the radiative recombination is basically balanced by a generation process. The recombination rate due to radiative mechanisms can be expressed as:

$$U_{rad}^{NET} = B(np - n_i^2) \tag{2.27}$$

2.3.1.3 Trap-assisted recombination

The energy band-gap should be inaccessible by the electrons. Defects in the semiconductor materials, however, can create energy levels that allow hosting electrons. If a two-step recombination process takes place (electrons from the conduction band to the defect level and from the latter to the valence band), this mechanism is called trap-assisted recombination mechanism. Given a single energy level trap, the net resulting recombination can be defined by the following equation, in accordance with the model proposed by Shockley-Read-Hall (SRH) recombination:

$$U_{SRH}^{net} = \frac{np - n_i^2}{\tau_{hSLT,0}(n + n_1) + \tau_{eSLT,0}(p + p_1)} \tag{2.28}$$

where

$$n_1 = N_C exp\left(\frac{E_{TRAP} - E_C}{kT}\right), \qquad p_1 = N_V exp\left(\frac{E_V - E_{TRAP}}{kT}\right) \tag{2.29}$$

and E_{TRAP} represents the energy level at which the defect occurs, $\tau_{\mathrm{eSLT,0}}$ and $\tau_{\mathrm{hSLT,0}}$ denote the SRH carrier lifetimes for electrons and holes, respectively, and N_C (N_V) is the density of states in conduction (valence) band with edges of E_C (E_V). $\mathrm{E_{TRAP}}$ = $Eg/2$, with Eg as the energy gap, leads to the peak value of $U_{\mathrm{SRH}}{}^{\mathrm{net}}$ as it maximizes the probability of the two-step transition. Defects are also typically present at the interfaces, and a model for the recombination mechanism (surface SRH) can be obtained by:

$$U_{SRH,SURF}^{net} = \frac{S_{e,0}S_{h,0}(np - n_i^2)}{S_{e,0}(n + n_1) + S_{h,0}(p + p_1)} \tag{2.30}$$

adopting the surface recombination velocities for $S_{e,0}$ and $S_{h,0}$.

2.3.2 Optical losses

Concerning the optical properties, the Transmittance $T(\lambda)$ and Reflectance $R(\lambda)$ can be expressed as:

$$T(\lambda) = \frac{P_{Tran}}{P_{Inc}}, \qquad R(\lambda) = \frac{P_{Refl}}{P_{Inc}} \tag{2.31}$$

where P_{Inc} represents the incident power, P_{Refl} is the reflected part of P_{Inc}, and P_{Tran} is the transmitted portion P_{Inc}. By assuming the use of a back reflector (ideal) $T(\lambda)$ is equal to 0. The given optical conservation law therefore, results in:

$$R(\lambda) + T(\lambda) + A(\lambda) = 1 \tag{2.32}$$

where $A(\lambda)$ is the absorbance of the solar cell dependent on the wavelength λ.

The reflectance from the external front interface represents the main optical loss, even though the optical properties of this interface are typically improved by adopting a texturized pattern and an ARC, as reported in section 2.2.

The shadowing caused by the front contact is also a significant source of losses. In this regard, the optimization of the front grid pitch is currently under investigation in PV research. In this study, the metal shading considered due to fingers is, in the best case, of around 1.1% [16], assuming an advanced lithography mechanism for the contact formation. Otherwise, for the most common screen printed technique, a percentage in the range of 3% - 4% is typically considered.

2.3.3 V_{OC} and FF losses

In addition to the recombination losses addressed in the previous subsections, the V_{OC} is also affected by the recombination losses that take place in the depletion region. The electrical behavior of a solar cell can be easily reproduced by the equivalent electrical circuit depicted in Fig. 2.9. The current-source refers to the

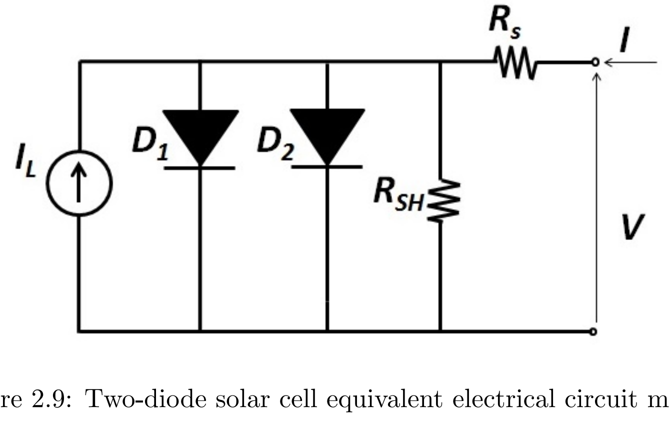

Figure 2.9: Two-diode solar cell equivalent electrical circuit model

photogenerated current (J_{PH} or J_{L}). The two-diode model is required in order to simulate the recombination mechanisms considered. If the recombination mechanism that occurs at the surface and inside the light absorber is modeled by D_1, in order to model the mechanism theat occurs due to the recombination within the space-charge region, a further diode has to be added (D_2). A deep understanding of the equivalent electrical circuit is proposed in [17], [18] and [19]. In this thesis, Chapter 4 proposes a comprehensive study aimed at reproducing and understanding the recombination losses ascribed to the depletion region of the pn-junction for the first-time proposed EWT-DGB solar cell.

Considering the solar cell and the two-diode circuit model depicted in Fig. 2.9, the expression of the I-V characteristic is expressed as:

$$J = J_{SC} - J_0\left(e^{\dfrac{qV_A}{n_{eff}KT}} - 1\right) \tag{2.33}$$

where J_0 is the saturation current density and n_{eff} is the ideality factor affecting the FF.

It is worth noting that the circuit of Fig. 2.9 is completed by two resistance contributions, the series resistance $\mathrm{R_S}$ and the shunt resistance $\mathrm{R_{SH}}$, both limiting the FF. The series resistance has been presented in the previous section, while $\mathrm{R_{SH}}$ refers to the quality of the pn-junction at the edge of the device (when defects or impurities are verified, the $\mathrm{R_{SH}}$ is reduced). Furthermore, in [11], the following models are reported for the FF:

$$FF = FF_0\left(1 - \frac{R_S}{R_{CH}}\right) \tag{2.34}$$

and

$$FF = FF_0\left[1 - \frac{(v_{OC} + 0.7)}{v_{OC}}\frac{FF_0}{r_{SH}}\right] \tag{2.35}$$

where FF_0 is the FF when $R_{SH} = 0$ and $R_S = 0$, respectively, R_{CH} is the characteristic resistance (V_{OC}/I_{SC}) and r_{SH} is defined as the normalized shunt resistance = R_{SH}/R_{CH}.

2.4 Advanced silicon solar cells: state-of-the-art overview

This section describes the advanced architectures that represent the state-of-the-art of silicon solar cells. The purpose of this part is to provide an overview of existing technologies in order to proper collocate the features of the solar cells addressed in this thesis. In fact, all the solar cell structures studied and presented in the following chapters have been conceived to exploit properties that are well highlighted in the state-of-the-art solar cell schemes.

2.4.1 Back-contact solar cells

The clear advantage of solar cells that feature both contacts at the rear side (back-contact BC solar cell) is an increase in the short-circuit current density J_{SC} thanks to the absence of front metal shading. This is the case of the emitter wrap through (EWT) and metal wrap through (MWT) solar cells, illustrated in Fig. 2.10 and Fig. 2.11, respectively. In the latter case, the optical shading is only reduced, not eliminated.

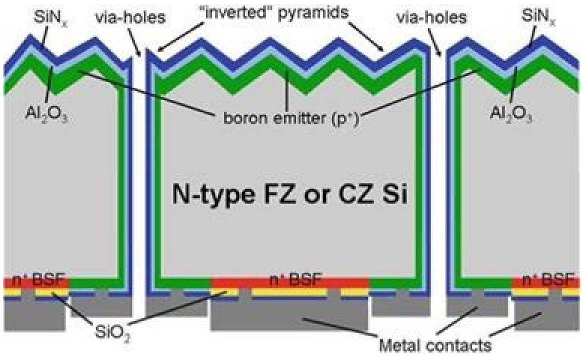

Figure 2.10: Cross-section of an EWT solar cell.

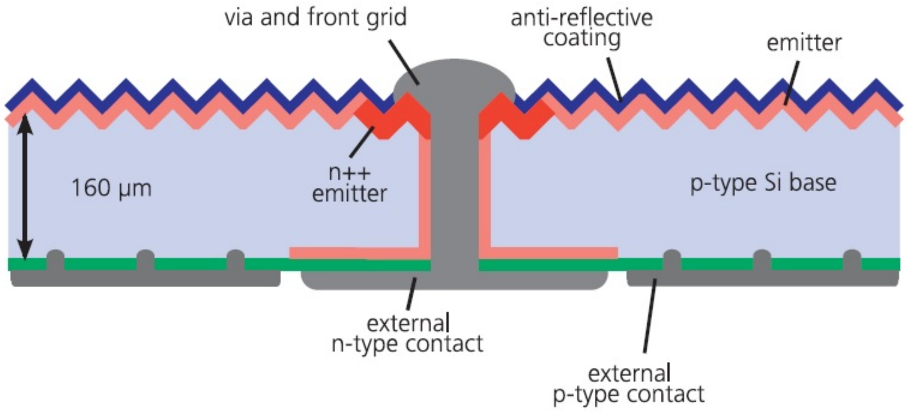

Figure 2.11: Schematic image of a typical MWT solar cell [20]

The EWT solar cell was proposed for the first time by Gee et al. [21]. After several analyses, over the last years some improvements of this scheme have been presented (a comprehensive discussion is reported in chapter 4), including an advanced numerical modeling that aims at understanding the main features of the design [22].

Concerning the MWT solar cell concept, it has been deeply analyzed by Thaidigsmann et al. [23], [20], Hendrics et al. [24] and Lamers et al. [25]. Moreover, Magnone et al. [26] have developed a numerical simulation of this structure based on experimental data.

In this thesis, the solar cell proposed in Chapter 4 (the so-called EWT-DGB solar cell) is based on the EWT concept while the simulation study discussed in Chapter 6.1 refers to the adoption of a point rear contact (section 2.4.2) on the well-known MWT solar cell.

In terms of performance, however, the most promising BC solar cell is the Interdigited Back Contact (IBC) solar cell (Fig. 2.12) [27], [28].

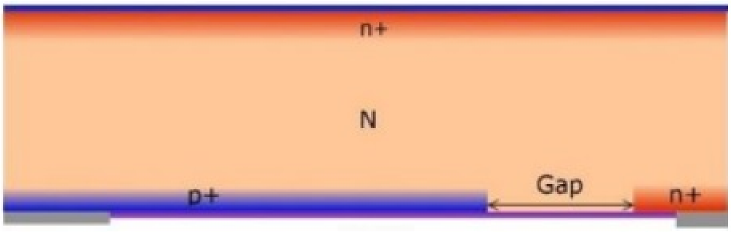

Figure 2.12: Sketch of a standard IBC solar cell (not in scale).

IBC solar cells allow for an excellent J_{SC} thanks to the absence of front metal shading and to the typical adoption of ARC layer. Furthermore, by adopting a high-quality light absorber material, and front- and back-surface field regions (FSF and BSF, respectively) it is possible to achieve a conversion efficiency at a cell level beyond 24% [27]. The main difference between the IBC and the EWT/MWT solar cell is that both *p*- and *n*-contacts are interdigitated and isolated (the emitter is placed only on the rear side).

An advanced modeling of the IBC solar cell was recently carried out by Procel et al. [29], providing a comprehensive analysis of susch a scheme. On the one hand, IBC solar cells achieve a promising conversion efficiency, while on the other hand the technological process is complex and onerous in terms of cost.

It is worth reporting that, recently, passivating structures on IBC solar cells were developed to enable higher conversion efficiency by quenching minority carriers recombination occuring at contact regions thanks to carrier-selective passivating contacts [30], [31], [32], [33], [34]. Chapter 5 includes analyses focused on solar cells with passivating carrier-selective contacts, which basic concepts are discussed in section 2.4.5.

2.4.2 PERC solar cells

Contact typically represents a relevant recombination source (the SRV on metal/Si is in the order of 10^6 cm/s). In order to reduce recombination at the contacts, several routes have been followed by the PV community. One example regards the adoption of a passivation layer at the back contact that reduces the metal/Si interface at the only puntcual contact region, this is the case of the passivated emitter and rear contact (PERC) solar cells (Fig. 2.13). In fact, PERC solar cells allow for a greater percentage of the back covered by a passivation layer/Si interface, featuring an SRV in the order of few tens of cm/s. In addition, the Al-BSF layer typically implemented on the rear surface for conventional solar cells, features a low reflectivity of the light, resulting in an increasing of heat losses. In PERC solar cells, the passivation layer is composed by an insulator which reflects long-wavelength light and therefore increases the photogenerated current. On the contrary, PERC solar cell may achieve conversion efficiency over 20% [35], [36]. However, the reduced minority carrier recombination loss at the rear interface takes place at the expense of the FF because, for the local rear contact, the current transport pattern is no longer 1-D but 3-D, thus introducing a current crowding effect (i.e. resistive losses).

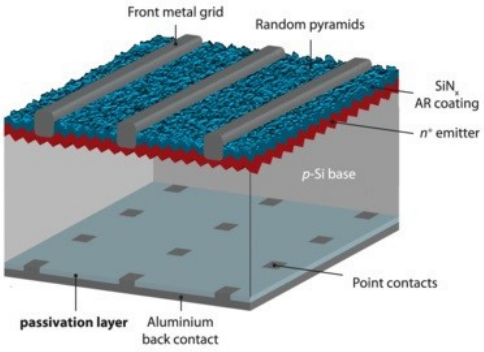

Figure 2.13: 3-D sketch of the PERC solar cell

Thanks to the fact that the fabrication of PERC solar cells is basically compatible with existing conventional cell production facilities, such technology is produced in a large scale at present, as discussed afterwards. As previously reported, Chapter 6.1 of this thesis concerns a study of the adoption of rear contact in MWT solar cell, including an advanced modeling of the spreading resistance and of the SRV resulting. Moreover, in sections 6.2 and 6.3, modeling studies focused on high-efficiency PERC solar cells are addressed.

2.4.3 Heterojunction solar cells

Another promising way to reduce recombination losses at the contacts (by also avoiding FF losses thanks to a resulting 1-D current pattern) is the adoption of carrier-selective contacts. The most attractive solar cell featuring carrier-selective contacts is the Silicon Heterojunction solar cell (SHJ) [30], [37], [38] (Fig. 2.14).

In this case, a stack composed of a metal/doped amorphous-silicon(a-Si)/intrinsic

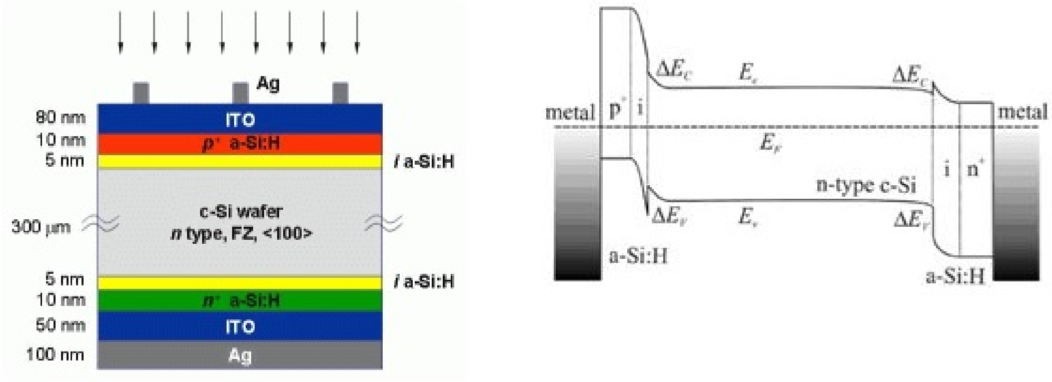

Figure 2.14: Cross-section scheme (a) and electronic band diagram (b) of the heterojunction solar cell (SHJ) (From [38]).

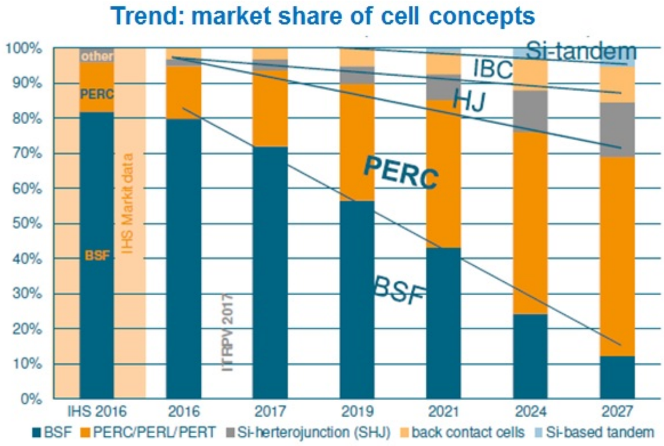

Figure 2.15: Market share trend reported in [35].

amorphous-silicon (i:a-Si)/c-Si substrate, guarantees the selectivity of the carriers, and permits only the majority carriers to reach the metal electrode (the minority carriers are rejected by the energy barrier). This leads to an absence of minority carriers at the contacts, therefore no recombinations can occur. The band-structure of this solar cell is shown in Fig. 2.14(b). Even though the SHJs achieve excellent V_{OC} values (around 750 mV), they present considerable drawbacks. Firstly, the presence of a transparent conductive oxide (TCO) is required for the contact formation to obtain satisfactory electrical properties. However, introducing a marked parasitic absorption effect. Secondly, a-Si cannot withstand temperatures above 200 ºC, while standard contact formation processes require temperatures of around 700 ºC.

In summary, the different schemes proposed in this section involve encouraging aspects in terms of performance improvements. However, the low cost-per-watt ratio requirement has to be always accounted for. This can be considered one of the reasons of the fact that the market share forecast of advanced c-Si-based solar cells reveals that PERC solar cells will play a significant role, covering a major part of the market demand, although their efficiencies are not the highest, as reported in Fig. 2.15 (from [35]). Moreover, it is expected a niche market share for the next years for both IBC and SHJs solar cells as well as for other concepts (e.g. Si-tandem), while conventional solar cells (BSF in Fig. 2.15) are expected to loss a considerable market share.

2.4.4 Record efficiency of c-Si based solar cell

The conversion efficiency record for c-Si solar cells is currently held by Kaneka [7]. It is worth noting that they reached the value of 26.7% by combining the concepts described in the previous subsection. The structure is depicted in Fig. 2.16, showing the adoption of a BC approach (IBC scheme) featuring carrier-selective contacts (recalling the SHJ concept). More in detail, the value of 26.7% has been obtained at laboratory cell level thanks to a J_{SC} ≈42 mA/cm^2, V_{OC} ≈745 mV and FF ≈85%.

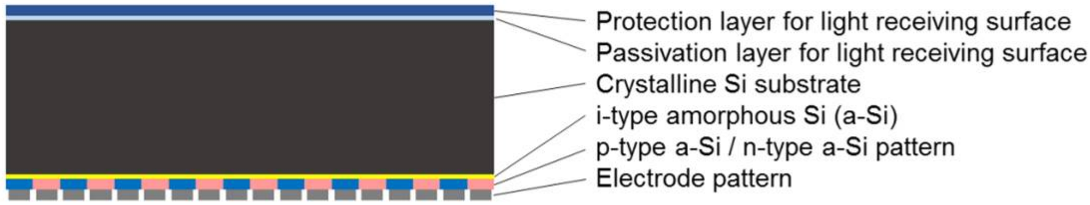

Figure 2.16: Cross-section schematic image of the SHJ-IBC cell that holds the conversion efficiency world record.

2.4.5 Innovative concepts: tunnel oxide passivated contact (TOPCon)

In order to overcome the problems mentioned in the previous sections for the presented high-efficiency solar cell concepts (such as the considerable fabrication costs), solar cells featuring passivated carrier-selective contacts have been proposed by the PV research community. One example is the case of solar cells featuring tunnel-oxide passivated contact (TOPCon).

Solar cells with TOPCon were originally proposed by Fraunhofer ISE [39] and recently studied by several research groups: Ingenito et al. [40], Tao et al. [41], Heng et al. [42] and Peibst et al. [43]. A scheme of solar cell with TOPCon and its band diagram is depicted in Fig. 2.17. The most interesting feature regards the

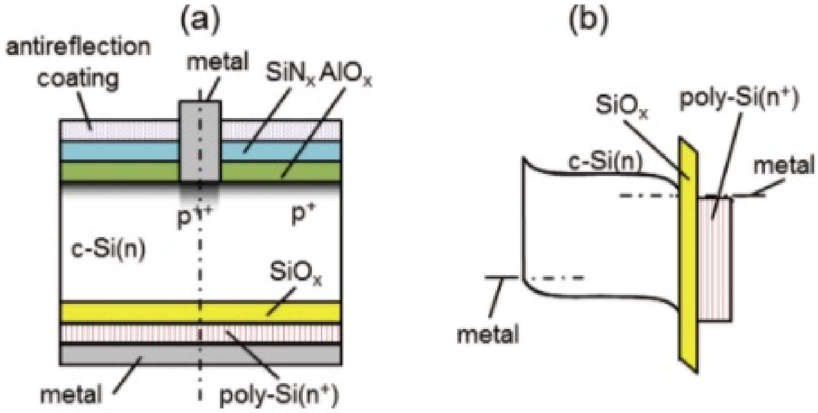

Figure 2.17: Sketch of solar cell with TOPCon (a) and relative band diagram (b). (From [44]).

rear surface, where a silicon oxide (SiO_2) layer of thickness ≈1.5 nm is placed between the c-Si substrate and doped poly-crystalline Si layer. Such concept prevents marked minority carrier recombination at the contact region, resulting in considerable higher V_{OC} due to the difference in terms of work function occuring between the layers considered. At the same time, thanks to an opportunely (heavily) doped thin Si-layer (e.g. poly-Si in Fig. 2.17), majority carriers are allowed to reach the metal contact by passing through the SiO_2 layer via tunneling mechanism. Solar cells with TOPCon demonstrated conversion efficiency even above 25% [45], [46].

In this thesis, detailed simulation studies of solar cells based featuring carrier-selective passivating contacts, by following TOPCon concept, are presented in Chapter 5. In particular, the structure presents a carrier-selective contact at both top/rear contact, re-calling the SHJ concept.

2.5 Concentrator photovoltaic (CPV)

Concentrator silicon solar cells are particularly worth of consideration because of their low-cost, fabrication easiness and affinity with conventional one-sun PV devices. In fact, thanks to the low material and processing costs, silicon solar cells can play an important role in low and medium CPV systems due to the good trade-off between conversion efficiency and overall cost [47].

Several design options of CPV Si solar cells, including vertical junction, multi-junction and hetero-junction solar cells, bifacial devices and back-contact back-junction (BC-BJ) solar cells, are proposed in the literature, and a quite comprehensive review of CPV Si solar cells is presented in [48].

In addition to the cell, a PV concentration system generally features a dedicated optical system that increases the luminous flux. More details may be found in [49]. One of the main difference between concentrator solar cells and conventional solar cells is the fact that the first ones are able to extract more current per unit of area, due to their exposure to the concentrated sunlight. Therefore, limiting the resistive losses is one of the main goals to achieve.

Solar cells for CPV have to fulfill several demands such as the minimization of optical losses due to shadowing at the front side, the reduction of front grid resistance as well as of resistance of the absorber material (base). Moreover, a high-efficient light trapping scheme is typically present in such solar cells. One of the main basic solar cell for CPV is the PESC cell (Fig. 2.18). In this case, a smaller resistance may result by implementing a dedicated front metal grid and by passivating the front surface by including a dielectric layer. As a metter of fact, to circumvent the limitation ascribed to the presence of a front metal grid, Slade et al. [51] proposed a back-junction point-contact silicon solar cell featuring a slightly doped base of high lifetime and p- and n-doped emitters arranged at the back of the cell. In this cell, no base component of the series resistance results, thanks to the fact that no current-flow from the front to the back occurs. Therefore, such a solar cell is able to work at higher concentration. The Slade's cell still holds the effciency record under concentrated light (27.6% at 100 suns). However, limitations in terms of cost due to the onerous process and to the requirement of high-quality material (elevated lifetime and FZ substrate typically 100-μm thick) are the main reasons why simpler solar cell architectures are still interesting.

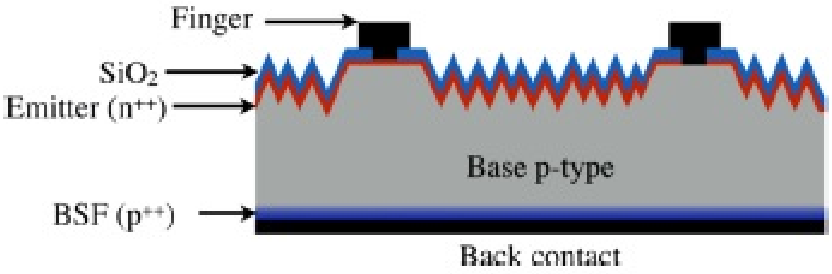

Figure 2.18: Example of vertical section (not in scale) of PESC silicon solar cell. (From [50]).

The studies presented in this thesis, in particular those of Chapter 4, are focused on a novel scheme conceived for CPV applications: the EWT-DGB solar cell. The carried out modeling activity described in such chapter also compares the proposed structure with a well-known PESC fabricated with the same CMOS-like process.

Chapter 3

Advanced numerical simulations of silicon solar cells

After a brief overview of the most common numerical device simulation tools, this chapter presents the main features of the tool used to obtain the results published in this work (Sentaurus tools provided by Synopsys [52], [53], [54], [55]). In particular, it illustrates the methods adopted to properly calculate the optical generation within the device. Moreover, the basic principles of the numerical methods used in the electrical simulations are reported, including the band-gap narrowing model, the modeling of the recombination mechanisms and the carrier mobility models. The last part of this chapter describes the advanced modeling of the different types of contact used in this thesis.

3.1 Numerical device simulation tools

Several simulation tools are commonly used by the scientific PV community for the electrical simulation of solar cells. Among others, PC1D [56], Quokka [57] and Afors-Het [58] are available for free use. While on the one hand PC1D guarantees a simple approach thanks to its interface and short simulation time, only 1-D and 2-D simulations of solar cells are workable, avoiding complex features. In addition, advanced physical concepts concerning carrier transport mechanisms (e.g. carrier-selective contacts governed by the tunneling effect) cannot be modeled. Fast simulations are also possible with the Quokka simulator [59], in which even the 3-D modeling of solar cells can be carried out by using a conductive boundary conditions approach. Nevertheless, physical concepts and mechanisms, such as those addressed in this thesis, are difficulty handled. Further, the simulation of only one cell design (the heterojunction solar cell) as well as the restriction of the 1-D domain are the main drawbacks of the Afors-Het [58] tool.

In view of the above, for the modeling of advanced concepts such as those addressed in this work, including comprehensive studies of several solar cell architectures and their main physical mechanisms, the use of a powerful simulation tool (non-free) was necessary.

All the results reported in the following chapters were obtained with the Sentaurus Device tool developed by Synopsys [52]-[55].

3.1.1 Sentaurus Device tool

Sentaurus refers to a wide field called Technology Computer-Aided Design (TCAD) and permits to carry out general-purpose simulations.

For the objective of this thesis, however, only electrical and optical simulations were performed, while the simulation of semiconductor processing and device fabrication are not covered in this work. A general numerical simulation of a solar cell follows two main steps. First, an optical simulation has to be performed in order to calculate the optical generation map (typically 1-D) inside the device. Thereafter, the optical map is loaded as input for the electrical simulations, where the basic equations of the current transport are solved at each point of the discretized domain. In fact, the simulator works on a standard domain (called symmetry element) of the solar cell of interest, opportunely chosen by exploiting the geometrical features of the device.

Using Sentaurus, advanced solar cell schemes have been analyzed by conducting 1-D, 2-D and 3-D simulations. The modeling of several features such as the back surface field (BSF), the rear point contact (RPC) and carrier-selective contacts were successfully obtained. The up-to-date physical models were taken into account for basing the activity on the state-of-the-art of the solar cell modeling. As a matter of fact, optical simulations of domains featuring front pyramidal pattern (texturing) were carried out by including the modeling of such advanced effects, such as the Free carrier absorption (FCA) and the roughness at the back interface.

The following sections describe the basis of the numerical simulation of solar cells and the main optical and electrical simulation methods of the Sentaurus environment used for performing the activities reported in this thesis.

3.2 The finite element method

As abovementioned, in order to electrically simulate solar cells in Sentaurus, the basic semiconductor equations reported in section 2.1 are solved by means of a finite element method (FEM) allowing the implementation of complex meshes and geometries. The application of the FEM includes the discretization of the simulation domain into elements (i.e. identifying the opportune mesh) and the following

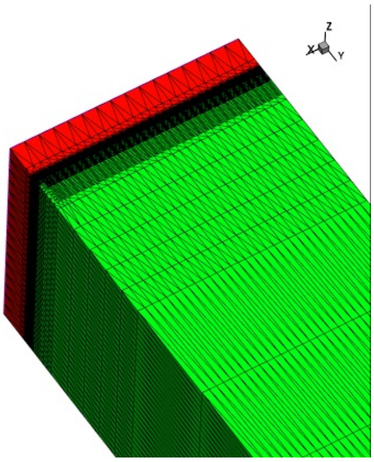

Figure 3.1: Example of 3-D standard domain featuring a local refined mesh.

derivation of the equations for such elements. Afterwards, a solution region composed by the elements in which the equations are numerically solved is created. The equations are iterativelly solved in each element, by starting from assigned initial values, as long as the desired level of convergence of the solution is achieved. The generation of the mesh is an aspect worth of discussion. Such process is typically related to the dimensions and the geometries of the standard domain used to reproduce the behavior of the overall device. The mesh elements identify the nodes (or the points) in which the equations have to be solved. It has to be considered that such elements are smaller and they cannot feature overlapping. The mesh refinement is sensitive to the region and to the expected gradient of the quantities to model such as the electric potential. However, the increasing of the number of elements leads to an unavoidable growth of the computational costs, intented as simulation time and cpu-memory occupied. In the case of 3-D simulations these aspects may lead to a compromise outcome of the analysis. Therefore, an opportune and reasonable mesh has to be implemented in order to optimize the trade-off between computational effort and the accuracy of the simulation.

In this thesis, clear examples of studies involving advanced mesh generation are reported in Chapter 4 and in Chapter 6.1, where 3-D structures are modeled performing proper local-mesh refinements aimed at achieving the desired accuracy by maintaning reasonable computational efforts. Figure 3.1 shows an example (3-D) of a discretized domain featured by a local-mesh refinement.

3.3 Optical simulation

The first part of the optical simulation involves a symmetric element that reproduces the overall behavior of the solar cell. Since solar cells typically feature a texturized

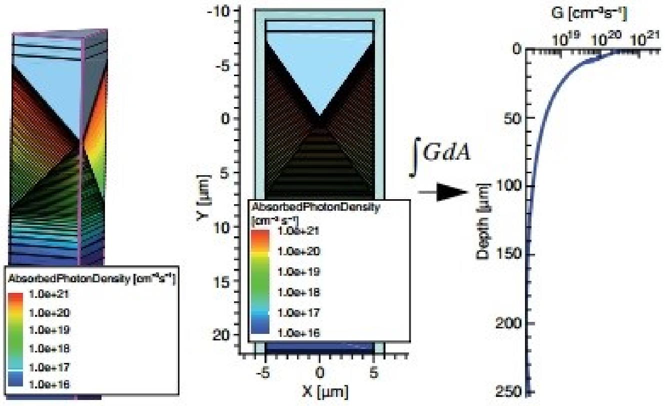

Figure 3.2: Example of 3-D symmetric element featuring a quarter of a pyramid and the extraction of a 1-D optical generation profile which has to be loaded into the electrical simulation (Figure from application note of [55]).

surface, a common domain is represented by a quarter of a pyramid, as depicted in the 3-D sketch of Fig. 3.2. It is worth reporting that the optical shading of the solar cell due to the front grid is not considered at this level. In this study, in all the simulation activities analyzed, the front metal shading has been accounted for in the electrical simulations by means of a geometric scaling factor.

Once the symmetry element has been identified, in order to properly perform the optical simulation it should be noted that the interaction of light and radiation silicon is governed by several mechanisms, depending on the properties of the materials involved. The relevant optical methods, typically included in the Sentaurus simulations in order to model such mechanisms, are presented in the following subsection.

3.3.1 Carrier generation and parasitic absorption

The absorption mechanisms used in the modeling can be classified into two main types, the so-called band-to-band absorption and other mechanisms, usually referred to as parasitic absorption because they do not lead to the generation of charge carriers.

Band-to-band absorption is responsible for the photovoltaic conversion, since it refers to the free carrier generation (i.e. photogenerated electron-hole pairs). A comprehensive physical explanation of carrier generation due to an interaction with a photon is reported in [11]. Fig. 3.3 illustrates the absorption coefficient of silicon. Since silicon is an indirect band-gap material ($\approx$ 1.1 eV), the absorption coefficient α_{Si} presents lower values for wavelengths of around 1.1 μm.

Parasitic absorptions include all the processes whereby photon absorption oc-

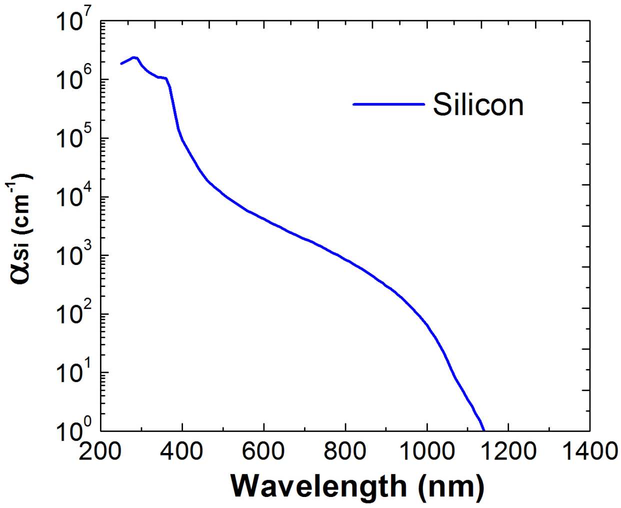

Figure 3.3: Silicon absorption coefficient α_{Si} at 300K as a function of the vacuum wavelength of light [11].

curs without leading to a free carrier generation [60]. Concerning the absorption mechanisms, both lattice absorption and free carrier absorption (FCA) should be considered. Since the low energy of the phonons leads to a significant lattice absorption at extremely high wavelengths, the absorption of the lattice is not considered in the numerical simulation of the solar cells. However, FCA effect plays a significant role for wavelengths above 0.9 μm. As a matter of fact, this effect on c-Si material can not be neglected in the simulations.

3.3.1.1 Modeling of the free carrier absorption effect

The FCA effect is the result of photons being absorbed by free electrons (holes). This leads to an excitation of a free carrier that is able to transit to the conduction (valence) band. Such excitation can take place both between states belonging to the same band and in different bands. By studying the dependence of the FCA effect on the free carrier concentration ($\mathrm{N_D}$ or $\mathrm{N_A}$) and on the wavelength, the absorption coeffient due to FCA (α_{FCA}) can be expressed as [61]:

$$\alpha_{FCA} = C_n n \lambda^2 + C_p p \lambda^2 \tag{3.1}$$

where C_n is related to the material refractive index, the effective masses and the mobility of the electrons while C_p refers to the holes. In this work, a the FCA effect is taken into account for in Chapter 5 where solar cells featuring poly-Si/$\mathrm{SiO_x}$ contacts are studied. It is worth reporting that the values of α_{FCA} used in this thesis have been measured by Fraunhofer ISE.

In order to perform a numerical simulation, the imaginary part of the refractive index (extinction coefficient k) of the semiconductor materials involved (c-Si or poly(crystalline)-Si) was evaluated according to the following relationship:

$$\alpha = \frac{4k\pi}{\lambda} \tag{3.2}$$

where λ is the wavelenght considered. A detailed characterization of the absorption coefficient α_{FCA} in c-Si is reported in [62], where, starting from experimental data, a confidence interval of such parameter and a comparison between different parameterizations is proposed.

3.3.2 The Phong illumination model

The optical model described in [63] is used when a precise and dedicated modeling of the rear interface in silicon solar cells is required. In detail, at a material interface, the incident light ray reflection is expressed by:

$$R = R_0 cos^{\omega}(\alpha) \tag{3.3}$$

with R_0 definded as the Phong parameter, which expresses the maximum reflection when the direction of specular reflection is considered, and ω is the diffuse scattering parameter, named the Phong exponent. The ideal diffuse reflection implies $\omega = 1$, while the specular reflection is obtained when ω approaches infinite.

In this thesis, the Phong parameters have been chosen by means of the tuning of R_0 and of ω in order to reproduce the experimental values of the solar cell reflection at wavlengths above 0.9 μm. In fact, in this portion of the spectrum the reflection on the rear side plays a significant role, as the absorption coefficient of the silicon decreases when the wavelength increases (Fig. 3.3).

In conclusion, at extremely high wavelengths an accurate modeling of the FCA effect and of the reflectivity at the rear interface is required in order to properly account for all the mechanisms involved.

3.3.3 Transfer matrix method

The most common solar cells architectures presents thin layers featuring thicknesses of the same order of magnitude of the incident radiation wavelengths (e.g., ARC layers with thickness of around 100 nm, as introduced in section 2.2). In these cases, an opportune optical method needs to be adopted to account for the wave optical effects. The Transfer matrix method (TMM) [64] guarantees the proper modeling of such interfaces/stacks by calculating the fractions of reflected, transmitted and absorbed light. The TMM method requires the knowledge of the refractive indexes as well as the thicknesses of the materials involved.

Most of the optical simulations performed and reported in this thesis involve the use of TMM. This is the case of the anlysis concerning the EWT-DGB solar cells of Chapter 4 and the solar cells featurng carrier-selective passivating contacts of Chapter 5.

3.4 Electrical simulation

3.4.1 Effective intrinsic carrier concentration and Band-Gap Narrowing

The intrinsic carrier density (n_i) is one of the most important parameters for properly modeling solar cells based on semiconductor materials. Its accurate determination is crucial for interpreting the recombination losses. The up-to-date n_i value reported in literature is $9.65 \cdot 10^9$ cm^{-3} for a given temperature of 300 K, considering silicon without doping [65]. This value is in agreement with the results of experiments carried out using capacitance measurements [66].
In addition, the temperature dependence of the energy of the band-gap has to be modeled:

$$E_G(T) = E_G(0) - \frac{\alpha}{T}^2 T + \beta \tag{3.4}$$

where $E_{G(0)}$ is the energy of the band-gap at $T = 0$ K and α and β are specific parameters of the materials involved. E_0 is defined as:

$$E_G(0) = E_{G,0} + \Delta E_{G,0} \tag{3.5}$$

where $E_{G,0}$ and $\Delta E_{G,0}$ depend on the band-gap narrowing (BGN) model adopted. Considering a temperature T, the effective energy band-gap ($E_{g,eff}$) results as:

$$E_{g,eff} = E_G(T) - E_{BGN} \tag{3.6}$$

with:

$$E_{BGN} = \Delta E_{G,0} - \Delta E_{G,f} \tag{3.7}$$

where $\Delta E_{G,f}$ is a factor related to the statistic model considered for the carriers. Del Alamo has proposed a largely adopted model for BGN in silicon [67], [68]. Other models are proposed in the literature, characterized by the fact that all of them present a BGN that is strictly dependent on the doping level concentration, whereas the effect of the free carrier concentration is not accounted for. As situations such as high carrier concentrations can occur, the Schenk BGN model has been adopted and opportunely tuned to properly reproduce n_i value of 9.65·10^9 cm^{-3} in case of lower doping concentrations.

It is worth reporting that the n_i measured data presented by Altermatt et al. [69] are in satisfactory agreement with those calculated using the Schenk-adapted BGN model. In the simulations performed in this work, the BGN is accounted for by using, as input, a table that enables calculating the BGN value for each doping concentration of donors and acceptors.

3.4.2 Recombination mechanisms

Chapter 2 reports the main physical aspects of the principal recombination processes involved in semiconductor-based solar cells. The following sections describe the relationships that enable the modeling of these effects by means of numerical simulations. A thorough documentation can be found in [55].

3.4.2.1 Shockley-Read-Hall recombination

Shockley-Read-Hall (SRH) recombination implies the presence of a defect level within the forbidden energy gap. In case of Maxwell-Boltzmann statistics:

$$R_{SRH} = \frac{np - n_{i,eff}^2}{\tau_p\left[n + n_{i,eff}e^{\dfrac{E_T}{kT}}\right] + \tau_n\left[p + n_{i,eff}e^{\dfrac{E_T}{kT}}\right]} \tag{3.8}$$

by indicating, with E_T, the difference between the energy of the defect level and the intrinsic energy (0 for c-Si). The Scharfetter relation enables the description of the SRH lifetimes depending on the doping concentration. Here, the electron lifetime is reported:

$$\tau_e(N) = \tau_{e,min} + \frac{\tau_{e,max} - \tau_{e,min}}{1 + \left(\dfrac{N_e}{N_{REF}}\right)^{\gamma}} \tag{3.9}$$

and the temperature dependence is:

$$\tau_e(T) = \tau_{e,0} + \left(\frac{T}{300K}\right)^{\alpha} \tag{3.10}$$

The SRH recombination also occurs on surfaces. In such cases, the so-called surface

SRH recombination can be modeled by:

$$R_{SRH,surf} = \frac{np - n_{i,eff}^2}{S_h^{-1}\left[n + n_{i,eff}e^{\frac{E_T}{kT}}\right] + S_e^{-1}\left[p + n_{i,eff}e^{\frac{E_T}{kT}}\right]} \tag{3.11}$$

where S_h and S_e are the surface recombination velocities (SRV) of holes and electrons, respectively. These parameters are related to the doping concentration on the surfaces and are strictly dependent on the quality of the interfaces. The doping dependence is accounted for by means of the following relation:

$$S = S_0\left[(1 + S_{REF}(\frac{N_S}{N_{REF}})^{\gamma}\right] \tag{3.12}$$

with N_S defined as the doping concentration value at the interface and with γ, N_{REF} and S_{REF} adjustable values.

3.4.2.2 Auger recombination

The Auger recombination rate (belonging to the band-to-band recombination mechanisms) is modeled in the Sentaurus environment by means of the following relationship:

$$R_{AUG} = (C_{T,n}n + C_{T,p}p)(np - n_i^2) \tag{3.13}$$

where $C_{T,n}$ and $C_{T,p}$ are the Auger coefficients dependent on the temperature T. Such equation recalls the equation (2.24) which mathematically describes the Auger recombination mechanism.

3.4.3 Carrier mobility models

The acceleration of electrons and holes is directly related to the electric field. However, the momentum of such carriers is typically reduced due to several scattering mechanisms. As a matter of fact, in addition to the electric field, carrier mobilities are dependent on the lattice temperature and the doping concentration. In particular, when the intensity of the electric field is relatively high, the carriers' mobility is limited by the increased scattering probability between them as the carriers gain energy, while for lower electric field intensities the mobility is only affected by scattering due to collision with impurities. The modeling of carrier mobility can be described according to the Philips' unified mobility model [70], [71], where, in addition to the scattering contribution μ_{scatt}, the phonon effect μ_{phon} is also taken into account:

$$\frac{1}{\mu_{eff}} = \frac{1}{\mu_{phon}} + \frac{1}{\mu_{scatt}} \tag{3.14}$$

it is worth noting that μ_{phon} is Temperature dependent:

$$\mu_{phon}(T) = \mu^{max} \left(\frac{T}{300K} \right)_{c}^{\theta} \tag{3.15}$$

3.5 Contact modeling in silicon solar cells

The numerical simulation of solar cells implies the modeling of the contact between the metal and the semiconductor. Two main types of contacts may be considered, the Schottky contacts (the Schottky barrier at the metal-Si interface) and the ohmic contacts. This section includes a short introduction to carrier-selective contact modeling that is helpful to better understand the results reported in Chapter 5.

3.5.1 Metal-semiconductor contacts

The Schottky barrier refers to cases when the metal and the semiconductor are in direct contact. Since the Fermi energies of the materials that comprise the interface are coincident, an energy barrier arises. In the case of n-type silicon, the barrier height is:

$$q\phi_B = q(\phi_M - \chi) \tag{3.16}$$

where $q\phi_{\mathrm{B}}$ and $q\phi_{\mathrm{M}}$ are the work function of the silicon and the metal, respectively, and $q\chi$ is the electron affinity of the silicon. The presence of a Schottky barrier leads to the formation of a depletion region that is entirely confined into the semiconductor material.

As a matter of fact, the metal-semiconductor contact in silicon solar cells is generally modeled as an ohmic contact. When the semiconductor features higher doping concentration values (the most common case for advanced Si-based silicon solar cells) the depletion region present in the semiconductor is enough narrow to allow for a high tunneling current through the barrier. The contact resistance is therefore lower.

For all the simulation results reported in this thesis, the standard approach is the assumption of an ohmic contact, except when opportunely changed, as in case of the MWT solar cells simulation (Chapter 6.1).

3.5.2 Carrier-selective contacts

When a carrier-selective contact is defined, it refers not only to the metal-silicon electrode but also to the region (or the stack of materials) that forms the contact region. For example, in this thesis, the poly-Si contact discussed in Chapter 5 includes the following stack: $\mathrm{SiO_x}$/poly-Si/metal. In this case, the dielectric tunnel layer is included within the “contact” region. The term carrier-selective refers to cases when the majority carriers flow toward the respective electrode, while the minority carriers are not allowed to reach the metal electrode. In other words, selectivity of the carriers occurs.

Classical carrier-selective contacts are the SHJ contact [37] or the TOPCon contact [72], as treated in Chapter 2. In these cases, due to the doping concentration and the higher band-gap (in the case of using a-Si), a significant band-offset (or band-bending) is verified at the material interfaces. In an ideal case, the band-offset exists only for the minority carrier, which are therefore prevented from passing through the interface. A deep understanding of the processing features of this contact (in particular, the TOPCon contact) is reported in [73], [74], [75], [76].

In this work, the current through the dielectric $\mathrm{SiO_x}$ has been assumed to be governed by only the tunneling mechanism. Several authors have presented different opinions about the main current mechanism through ultra-thin oxide layers. In [43] and [77], the role of pinholes in a n^+- p^+-polo junction on both the top and rear side in solar cells is addressed. The scope of this work, however, is not to compare several possible mechanisms (either exclusively or in combination), but rather to reproduce the behavior of the contact in order to analyze and investigate the features, advantages and drawbacks of the solar cells implementing such a type of contact. As mentioned, in this work the simulations are only based on carrier-selective contacts governed by tunneling mechanisms. To this aim, several parameters have been included in Sentaurus in order to define when a current via tunneling effect has to be modeled in electrical simulations.

3.5.3 Modeling of the tunneling mechanism in Sentaurus

Since the tunneling probability is dependent on the effective tunneling masses for both electrons ($m_{t,e}$) and holes ($m_{t,h}$) such values have to be opportunely chosen. In the literature, the reported range for $m_{t,e}$ is from to 0.3 to 0.42 m_0 (m_0 is the rest mass) while for $m_{t,h}$ from 0.2 to 0.3 m_0.

To allow the numerical simulation of such a mechanism, a non-local mesh has been implemented in Sentaurus [55]. Indeed, the basic concept of modeling tunneling currents implies the creation of locally distributed generation (and recombination) processes related to the Fermi level and the energy carrier. The relation of the local carrier generation rate G_L with the current ascribed to the tunneling mechanism J_T

can be expressed by:

$$G_L = \frac{1}{q}\nabla \cdot J_T = \frac{1}{q}\frac{dJ_t}{d\varphi} \cdot \nabla\varphi = \frac{dJ_t}{d\varepsilon} \cdot E \tag{3.17}$$

where the electrostatic potential is denoted by φ, ε represents the energy level, and E is the electrical field. Once J_T has been obtained, the generation rate G_L can be easily determined. As a first step, the tunneling probability T_p has to be calculated. In order to consider the simplest case possible, this study refers to a rectangular barrier:

$$T_p(E_x) = exp\left(-2\int_a^b k_{C/V}(x, E_x)\,dx\right) \tag{3.18}$$

where a and b are the turning points of the barrier and k_C (k_V) is defined as the complex local wave numbers of electrons (or holes) at a given position position x:

$$k_C(x, E_x) = \sqrt{2m_{t,e}(E_x - E_C)/h^2} \tag{3.19}$$

$$k_V(x, E_x) = \sqrt{2m_{t,h}(E_V - E_x)/h^2} \tag{3.20}$$

where $m_{t,e}$ and $m_{t,h}$ are the tunneling masses for electrons and holes, respectively.

The tunneling probability is therefore related to the tunneling masses values $m_{t,e}$ and $m_{t,h}$ which, as reported above, are changeable parameters in the Sentaurus environment.

In the simulation studies regarding solar cells with carrier-selective passivating contacts discussed in this thesis (Chapter 5), the values of $m_{t,e} = 0.4\ m_0$ and of $m_{t,h} = 0.3\ m_0$ have been chosen as results of a fine tuning. These values allowed for the reproduction of the electrical behaviour of the contact observed experimentally.

Chapter 4

Numerical simulations of Emitter Wrap Through with Deep Grooved Base (EWT-DGB) solar cells

In this chapter, simulation studies of Emitter Wrap Through solar cells with Deep Grooved Base (EWT-DGB) contacts are presented. In the first two sections (4.1 and 4.2), the fundamental motivations of the conceiving of EWT-DGB solar cell are discussed. In addition, cell design, fabrication process, and a complete experimental characterization under 1-sun illumination of the first produced prototypes are presented and discussed. Section 4.3 reports 3-D numerical device simulations performed to investigate some remarkable features of the cell design and to describe the cell electrical characteristics at 1-sun irradiation. Section 4.4 concerns the analysis of the EWT-DGB solar cell under concentrated light and a comparison with the simpler passivated emitter solar cell (PESC). The potentials of the two architectures are studied for concentrated light conditions considering possible realistic improvements with respect to the fabricated devices. Furthermore, simulations are exploited to provide additional analysis of the EWT-DGB solar cell performance under concentrated light.
Most of the results presented in this chapter have been published in three articles [78], [79], [80], by the author of this thesis. The presented activity was performed in close collaboration with Fondazione Bruno Kessler (FBK, Trento, Italy) which fabricated and characterized the EWT-DGB solar cells.

4.1 Introduction to the EWT-DGB solar cell scheme

Among methods to keep competitive the costs of electricity produced by means of photovoltaic (PV) systems, one of the most promising is the concentrator photovoltaics (CPV) [81], which target is the reduction of costs by replacing the cell surface (expansive material), with cheaper optical components [82].

To date, CPV systems are still approximately three times more expensive than silicon PV systems, due to the relatively high cost of the cell typically used (GaInP, Ge, or GaAs) [83]. For this reason, silicon is still an interesting material for developing CPV cells. Moreover, CPV Si solar cells are particularly worth of consideration because of their fabrication easiness and affinity with conventional one-sun PV devices. In addition, if relatively high-efficiency small-area solar cells are fabricated by a process compatible with complementary metal–oxide–semiconductor (CMOS) technology, the solar cells may act as an energy harvester in integrated circuits, which include sensors, digital and analogue circuits as well as communication interfaces. In case, the optical concentrator can be realized by using polymeric materials that can be easily integrated with the chip [84].

Different kinds of concentrated silicon solar cells have been proposed over the past years [48]. Some authors (Ruby et al. [85], Morvillo et al. [86] and Paternoster et al. [50]) used a relatively simple CMOS-like process with only two or three photolithographic steps, to produce passivated emitter solar cell (PESC). More in detail, in [50], a three-photolithographic-step process was used to develop a PESC cell optimized for medium concentrated light; the confirmed efficiency was 22.1% under 80 suns and higher than 18% under 300 suns. In such a front and back-contact cell, the designed metal grid is the result of a trade-off between low metal coverage to limit optical losses and high coverage to limit resistive losses.

However, one of the main factors limiting the efficiency of front-contacted CPV cells such as PESC is the parasitic resistances arising from the front metal grid, front contacts and substrate resistivity and the shadowing due to the front metal grid. The back-contact scheme allows to overcome the limitations associated to front grid and contacts, potentially leading to interesting conversion efficiency (the BC-BJ cell proposed by Slade [51] reached the highest efficiency of Si solar cell under concentration, up to 27.6% at 92 suns [87]). However, the efficiency of BC-BJ solar cells exhibits a strong dependence on the substrate lifetime and thickness. As a matter of fact, BC-BJs are commonly fabricated on very thin substrates or high-quality float-zone (FZ) Si [51], [88], the second option being in contrast with the requirement for decreasing costs.

In order to overcome these limitations in terms of substrate requirements, the emitter-wrap-through (EWT) cell concept was originally proposed by Gee et al. [21] as a technique to accomplish high efficiency, even for rather low-quality absorber material. In such a scheme, whereas the emitter is still located near the

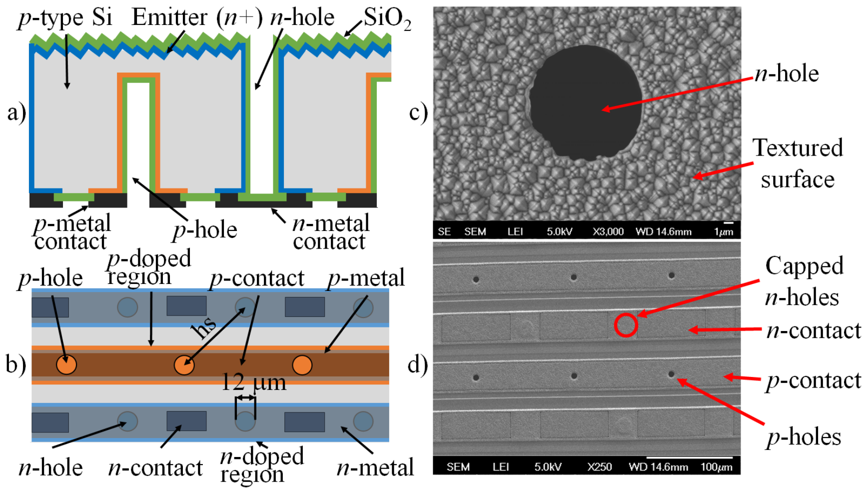

Figure 4.1: (a) Vertical cross section. (b) Back-surface scheme of the EWT-Deep Grooved Base (EWT-DGB) cell (not in scale). (c) SEM image of a hole rim on the texturized front surface. (d) SEM image of the back surface of the cell.

front surface, all contacts are fabricated on the rear. The connection between the front-surface active emitter and its contacts is provided by extending the emitter to the walls of holes etched through the substrate. The large coverage of electrically interconnected emitter areas allows collecting high current density without requiring high bulk lifetimes. EWT solar cells have been treated in detail by the PV community. Improvements adopted in order to achieve high efficiency values were discussed in [89], [90], [91], [92]. Moreover, Faika et al. [93] presented a fabrication approach adopting an Al-P-codiffusion, Harder et al. [94] proposed a laser-processed technique and Cho et al. [95] discussed high efficiency EWT solar cells featuring a non-uniform silicon-nitride passivation layer. In addition, the limiting aspects of the EWT concept have been deeply investigated in by Ulzhöfer et al. [22]. Regarding the numerical modeling of the EWT solar cells, Smith [96] proposed an equivalent electrical circuit. Moreover, 1-D and 2-D physics-based numerical simulations of EWT solar cells have been performed by several groups and implemented in different simulation tools [97], [98], [99], [100]. Furthermore, 3-D numerical simulations were successfully carried out in Sentaurus TCAD by Ulzhöfer [101]. Even though EWT cells have been largely used for 1-sun applications their use for CPV has not been extensively investigated.

In this chapter, a new solar cell design, based on the EWT concept and conceived for CPV applications is presented. In Fig. 4.1, a schematic of the vertical cross-section (a) and of the back surface (b) of the cell are illustrated. The cell, fabricated on a p-type c-Si substrate, features a front-side emitter and a passivated and texturized front surface (c). Both contacts and metallization grid are placed on the rear (d); therefore, the front surface is completely metal-free. The emitter on the front side is connected to the back contacts by means of n-doped pass-through holes following an EWT cell scheme. Furthermore, the cell features an additional matrix of p-doped holes, grooved through the substrate and placed alternately to the n-doped holes following a chessboard scheme. This design is defined as emitter-wrap-through solar cells with deep grooved base contact (EWT-DGB).

In this design, the distance between holes of the same type is of about 50–100 μm, much lower than the substrate thickness, providing an effective decoupling of the collection width, determined by the n-hole pitch, and the wafer thickness. Consequently, an increase in red-photon collection probability even in the case of low-lifetime substrates is expected. At the same time, due to the small distance, p-holes act as effective collecting electrodes, allowing a reduction of the resistive losses due to the substrate, a particularly important feature for CPV applications. This way, thick substrates with low lifetime ($\approx$60 μs in this study) have been used to produce cells approaching 19% efficiency and fill factor (FF) of 80% under 1-sun illumination. In other words, compared with a conventional EWT design, in the EWT-DGB cells, the n-type holes act as both collecting electrodes and conductive paths.

Moreover, the p-type and n-type hole distance is much lower than the substrate thickness, allowing to remove the dependence of collection width and series resistance on substrate thickness.

4.2 Fabrication of EWT-DGB solar cell

The first EWT-DGB cell prototypes have been produced in a CMOS-like pilot line at the Micro–Nano fabrication and characterization Facility of Fondazione Bruno Kessler (Trento, Italy). The aim of this first production was the evaluation of an innovative cell scheme never proposed before; therefore, the cell layout, the manufacturing process, and the production costs are not optimized yet. All the structures have been defined by means of photolithographic steps. The 4 mm x 4 mm cells were fabricated on 280-μm-thick c-Si 4-in wafers. Two different <1 0 0> Si substrates have been used: a low-resistivity 0.5 Ωcm p-type FZ silicon and a standard p-doped Czochralski (Cz) silicon wafers with resistivity of 10 Ωcm. Cz wafers need a lower boron concentration in order to prevent the formation of boron–oxygen compounds that lead to the well-known light-induced degradation (LID) drawback [102]. Otherwise, in the case of p-type wafers, recovery from LID would be necessary to reduce the efficiency degradation [103], [104], [105].

The main production steps are summarized in Fig. 4.2. First, a thermal growth of silicon oxide was accomplished to protect the front surface in the following steps (1). Then, on the back surface of the wafer, 260-μm-deep and 12-μm-wide holes were etched by means of a deep reactive ion etching (DRIE) technique and subsequently

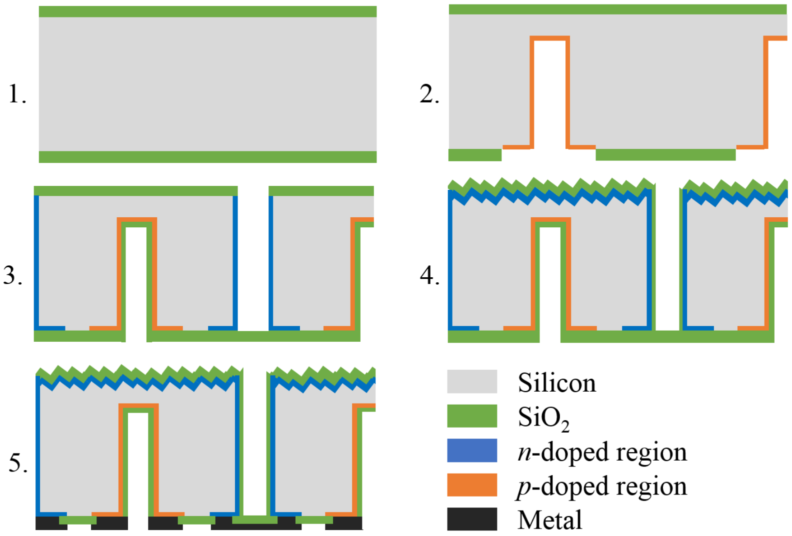

Figure 4.2: Principal steps of EWT-DGB production process. 1) Thermal growth of SiO_2. 2) Definition of the p-doped holes by means of photolithography, DRIE process, and boron doping by solid source diffusion. 3) Second thermal oxidation and subsequent formation of the pass through holes, successively ndoped with phosphorous. 4) Opening of the front surface from oxide, texturing of the surface, and phosphorous doping of the emitter, followed by thermal oxidation. 5) Lithographic definition of the back contacts and sputtering of the back metal.

heavily p-doped (140 Ω/sq) with boron solid source diffusion (2). A second thermal oxidation was performed to protect p-holes walls in the following steps, and then, a second matrix of pass-through holes (12-μm-wide) was carried out with a DRIE process from the front wafer side, and heavily n-doped (15 Ω/sq) by phosphorous solid source diffusion (3). To preserve the mechanical integrity of the wafer, n-holes were capped on the back of the cell by depositing a SiO_2 thick layer. The front surface has been texturized by random upright pyramids and then lightly n-doped (80 Ω/sq). A last oxidation step provided the front-surface passivation by a 105-nm-thick antireflecting SiO_2 front coating (4). The contacts on the cell backside were opened by means of a photolithographic step followed by a dry RIE etching. A uniform layer 2-μm-thick of Al-1%-Si was then deposited on the backside by means of sputtering. The last lithographic step defined the interdigitated metal grid and the busbars, which are finally separated by means of a dry etching of the aluminum layer (5). The main physical and geometrical cell parameters are summarized in Table 4.1, and scanning electron microscopic (SEM) images of the cell at the end of the fabrication process are shown in Fig. 4.1(c) and (d).

In this first part, three different cell prototypes, which differ in terms of hole spacing h_S (the distance between n- and p-doped holes), have been realized: h_s = 43 μm, 50 μm and 78 μm.

The EWT-DGB cells were separated by dicing and have been mounted on an adhoc printed circuit board and experimentally characterized under 1-sun illumination with a class AAB steady-state solar simulator (ABET Technologies SUN 2000 Solar Simulator), in accordance with the IEC 60904 international standard. The standard testing conditions (total irradiance: 1000 W/m^2; spectral irradiance: AM1.5G; cell temperature: T = 298 K) have been checked and calibrated with a certified standard reference cell from VLSI Standard Inc.

Table 4.1: EWT-DGB cells geometrical and physical parameters

Parameter	Unit	Value
Cell die area	mm^2	4 x 4
Wafer thickness	μm	280
Front emitter sheet resistance	Ω/sq	80
Hole sheet resistance (n-hole, p-hole)	Ω/sq	15, 140
Substrate doping concentration (FZ, Cz)	cm^{-3}	$3.5{\cdot}10^{16}$, $1.35{\cdot}10^{15}$
p-hole depth	μm	260
Hole diameter, hole pitch	μm	12, 80

4.3 EWT-DGB solar cell under 1-sun illumination

4.3.1 Numerical simulations of EWT-DGB solar cell

4.3.1.1 Simulation methods

Three-dimensional numerical simulations are performed by using a state-of-the-art finite-element TCAD device simulator [54] on a simulation domain chosen by exploiting the symmetry of the structure and depicted in Fig. 4.3. The simulation domain width is strictly related to the considered hole spacing (h_s) and includes a quarter of both p- and n-hole. The geometrical parameters of the simulated structure are the ones reported in Table 4.1.

Doping profiles of emitter and doped regions on the back are acquired by a dedicated campaign of secondary ion mass spectrometry (SIMS) analyses and then imported to reproduce the sheet resistance values of the fabricated devices, as successfully adopted in [50]. The doping profiles provided by SIMS measurements are considered as active because the peak of all the n-doped concentrations are lower than the well-known activation limit of $\approx 2{\cdot}10^{20}$ cm^{-3} [106]. Moreover, the sheet resistance of the holes has been measured by means of specific test structures, which, however, do not allow knowing the doping concentration profile along the hole depth. Since the doping profile measurement in the holes region is not straightforward, an analytical Gaussian profile is adopted in order to reproduce approximately the measured value of 15 Ω/sq in the n-holes and 140 Ω/sq in the p-holes.

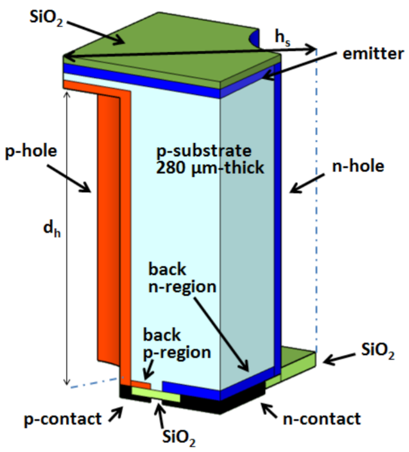

Figure 4.3: Fig. 3. Three-dimensional simulation domain of the considered EWT-DGB solar cell. $\mathrm{h_s}$ denotes the distance between n- and p-hole and $\mathrm{d_h}$ the p-hole depth.

In this study, the choice of a so low sheet resistance value for the n-type doped holes, aimed at reducing the resistive losses (particularly impactful for CPV applications), has not been optimized so far.

Two EWT-DGB solar cells are simulated with two different substrates: FZ and Cz. For the FZ, the adopted substrate resistivity value ρ_s is 0.5 Ωcm and the measured minority carrier lifetime τ_n is 62 μs, while for the Cz ρ_s is 10 Ωcm and τ_n is 190 μs.

4.3.1.2 Physical and Electrical models

Parameters of physical models already successfully adopted in [9], [10], [107], [108], [109], [110], [111], [112], are used. The temperature, doping, carrier density dependence of carrier's mobility, Auger and Shockley–Read–Hall (SRH) recombination are taken into account for. The doping concentration-dependent bandgap-narrowing model by Schenk is considered to account for the effective intrinsic carrier density [65] and Fermi–Dirac statistics is used in order to model more accurately highly doped regions. The unified mobility model proposed by Klaassen [70], [71] is considered, and concerning the Auger recombination, the Dziewior and Schmid parameterization [113] is assumed in order to consider the dependence on doping concentration and temperature. Moreover, the SRH model for trap-assisted recombination is adopted. In the substrate region, parameters for degraded boron-doped Cz-Si according to Glunz's parameterization [114] are adopted as well as for the highly doped BSF region. Radiative recombination is modeled as proposed by Trupke [115]. It is worth noting that considered values of parameters of the recombination model are chosen consistently to the revised value of intrinsic carrier concentration $n_i = 9.65{\cdot}10^9$ cm^{-3}

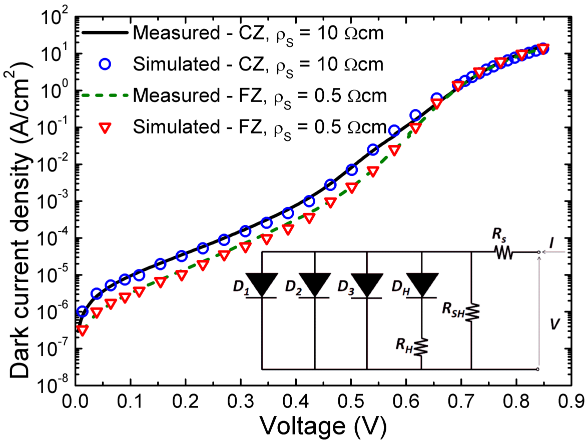

Figure 4.4: Measured and simulated dark J–V characteristic for both considered substrate (FZ, substrate resistivity ρ_S = 0.5 Ωcm and Cz, ρ_S = 10 Ωcm). In the inset, the equivalent electrical model for the dark analysis is reported.

at T = 300 K [116]. The assigned surface recombination velocity (SRV) values are [9], [114]: $5.8 \cdot 10^3$ cm/s at both front emitter and back passivated interfaces while at the back p-doped and n-doped region interfaces are $1 \cdot 10^3$ and $3 \cdot 10^4$ cm/s, respectively. Finally, the SRV for minority carriers at both contacts is set to $1 \cdot 10^6$ cm/s, which is a value close to the kinetic limit for nonpassivated surfaces [117].

The recombination losses in the n- and p-holes regions are specifically modeled in order to take into account for the high concentration of defects localized in these regions due to the deep holes etching process. In particular, it is considered a region around the n-type doped hole (n-hole region), where an effective carrier lifetime value was set as tuning parameter to reproduce the experimental value of saturation current densities, as explained in the following sections.

The spatially resolved optical generation rate profile is calculated by a ray tracer tool considering the internal bottom reflectivity at the different material stacks at the back interface: i) silicon/aluminum/air stack at contacted interface; ii) silicon/silicon-oxide/aluminum/air at passivated interface; and iii) silicon/silicon-oxide/air (see Fig. 4.1(a)). In order to model the typical roughness in such material stacks, a Phong diffusive boundary condition is adopted [63]. For the front interface, a texturing by regular upright pyramids is assumed.

4.3.1.3 Calibration methodology

The physical recombination parameters in the n-hole region and some other figures of merit (FOMs) such as the cell shunt resistance (R_{SH}) and series resistance due to contacts and metal (R_s) are calibrated by starting from the measured dark J–V characteristics. The equivalent electrical model reported in the inset of Fig. 4.4 is

Table 4.2: Saturation current densities of the equivalent electrical model of Fig. 4.4. The respective diode ideality factors are: $n_1 = 1$, $n_2 = 2$, $n_3 = 1.3$, and $n_H = 1$.

cell substrate	J_H *(A/cm²)*	R_H *(Ωcm²)*	J_{01} *(A/cm²)*	J_{02} *(A/cm²)*	J_{03} *(A/cm²)*
FZ	10^{-15}	1000	$1.7 \cdot 10^{-12}$	$2 \cdot 10^{-8}$	$5 \cdot 10^{-10}$
Cz	$8 \cdot 10^{-10}$	500	$1.8 \cdot 10^{-12}$	$2 \cdot 10^{-7}$	$2 \cdot 10^{-9}$

considered.

As matter of fact, the measured dark J-V characteristics are not acceptably fit by using a simple two-diode circuital model, in particular within the bias voltage range 0.3 to 0.6 V. In detail, the third equivalent diode (D_3, ideality factor $n_3 = 1.3$) takes into account for the recombination occurring in the highly defective region around the n-hole.

This region is few micrometer depth and also includes the depletion region of the n^+-p junction. It is worth noting that the recombination losses ascribed to the n-hole region markedly affect the performance in terms of V_{OC} (see following sections). The value of n_3 is consistent with the general theory of depletion region recombination proposed in [17]. The effect of the diode D_3 is appreciable for bias voltage from 0.45 to 0.6 V. Finally, the path composed of D_H and R_H accounts for edge recombination [18], which is observed to be considerable in the first run samples, affecting the dark J–V characteristic for bias voltage from 0.3 to 0.45 V. Such recombination effect is ascribed to the induced junction caused by the surface charge at the nondoped border regions, especially in the case of lowly doped substrates (for instance, the Cz solar cells; see Table 4.2). An equivalent circuit model similar to that of Fig. 4.4 has been proposed in [19]. Smith et al. [96] perfectly fit the dark I–V characteristic of their EWT solar cells by using a two-exponential model. However, they observed a soft-knee diode feature under illumination and proposed an equivalent circuit model that includes a voltage-dependent current source to describe the bipolar transistor effect.

From the fitting procedure, the SRVs at hole internal surface are set at $4 \cdot 10^4$ cm/s in the case of FZ substrate and $1 \cdot 10^3$ cm/s in the case of Cz. The adopted n-hole region effective lifetime values, chosen to model the effect of the the diode D_3, are 0.18 and 0.38 μs for the FZ and the Cz substrate, respectively. Numerical simulations of the EWT-DGB solar cells are performed by means of a TCAD mixed-mode device simulator where the solar cell is included in an electrical circuit, which directly takes into account R_{SH}, R_s as well as D_H and R_H. Fig. 4.4 shows the measured dark J–V characteristics and the simulated ones by using the calibrated physical models. Table 4.2 illustrates the calculated saturation current densities of the equivalent circuit. In the table, these values are compared for FZ and Cz EWT-DGB cells.

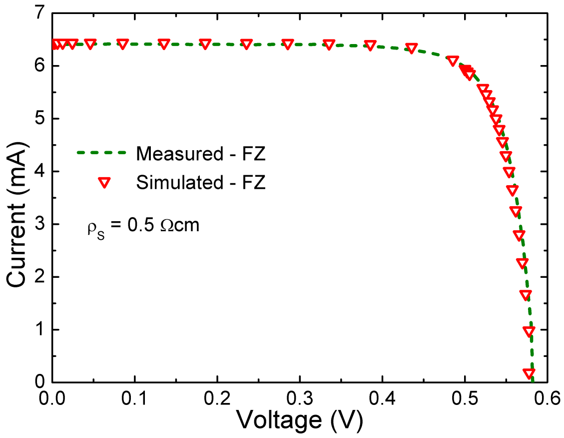

Figure 4.5: Measured and simulated I–V curve under 1-sun illumination for FZ substrate (substrate resistivity $\rho_S = 0.5\ \Omega$cm).

4.3.2 Results under 1-sun illumination

In this paragraph, the experimental characterization under 1-sun illumination of the EWT-DGB cells is reported and compared to simulations.

The experimental I–V curve at 1-sun is reported in Fig. 4.5 (green line) and compared with the simulated data (red triangles). The experimental and simulated FOMs are summarized in Table 4.3.

The experimental data are well reproduced by the numerical simulation within the assumed experimental uncertainty, by assuming an external resistance R_s of 0.15 Ωcm^2 for the metal grid in order to satisfactory match the measured FF and efficiency. In this study, the following relative experimental uncertainties, calculated and provided by FBK, are assumed: 1% for V_{OC}, 2% for J_{SC} and 5% for both FF and efficiency. A detailed description of the evaluation of such values is reported in [49]. The obtained J_{SC} value is higher than 40 mA/cm^2 for both the Cz and the FZ samples. The FF is around the 80% for the FZ cell, and the conversion efficiency reaches the 18.6% in the case of the FZ cell and the 16.8% for the cell

Table 4.3: Measured and simulated values of FOMs. The relative uncertainties of experimental values are indicated in the brackets.

Cell	Value	V_{OC} *(mV)*	J_{SC} *(mA/cm^2)*	FF *(%)*	Efficiency *(%)*
FZ	Measured	582 (1%)	40.1 (2%)	79.6 (5%)	18.6 (5%)
FZ	Simulated	578	40.2	79.7	18.6
Cz	Measured	551 (1%)	40.2 (2%)	76 (5%)	16.8 (5%)
Cz	Simulated	550	40.2	75.3	16.6

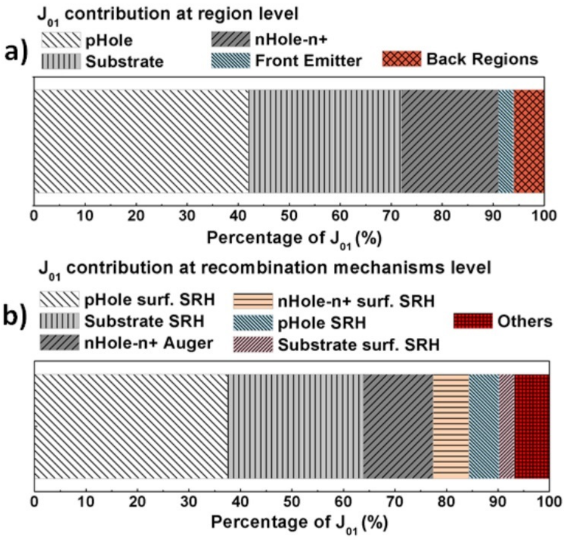

Figure 4.6: (a) Bar chart illustrating the dark saturation current density J_{01} contributions at region level for the FZ solar cell. In (b), the bar chart shows the contribution at recombination mechanisms level. n_{Hole}-n^+ is the n-hole diffusion region.

produced on the Cz substrate. Measured V_{OC} are 583 mV and 551 mV for the FZ and Cz cell, respectively. It is worth noting that these values are significantly lower than typical V_{OC} values of high-performance solar cells. This is ascribed to the high recombination losses present in these devices.

In order to understand the mechanisms underlying the V_{OC} limitation, a detailed recombination losses analysis in terms of J_{01} is carried out. In Fig. 4.6, the contribution of the regions which lead to relatively higher recombination losses is illustrated. More in detail, it can be observed that both p- and n-type holes and the substrate contributions regions are responsible for almost the 90% of the J_{01} (see Fig. 4.6(a)). Moreover, the most impactful mechanisms on J_{01} are the surface SRH recombination in the p-hole, the SRH recombination in the substrate, and Auger recombination inside the n-hole diffusion (see Fig. 4.6(b)). However, in the fabricated samples, J_{01} is not the only responsible for V_{OC} limitation. As a matter of facts, for both kinds of substrates, the observed V_{OC} degradation is mainly ascribed to the effect of the recombination losses within the n-hole region (diode D_3). In particular, in the case of Cz substrates, this contribution has a more marked impact compared to the FZ samples as confirmed by the current density J_{03} (see Table 4.2, contribute of diode D_3) which is appreciable for bias voltage from 0.45 to 0.6 V and, therefore, affects the V_{OC}. Moreover, in the case of high resistive substrates also losses due to edge recombination (D_H and R_H) lead to a further decrease in V_{OC}. Hence, despite edge recombination is mainly remarkable within the bias range 0.3–0.4 V, its effect is appreciable also at open-circuit bias.

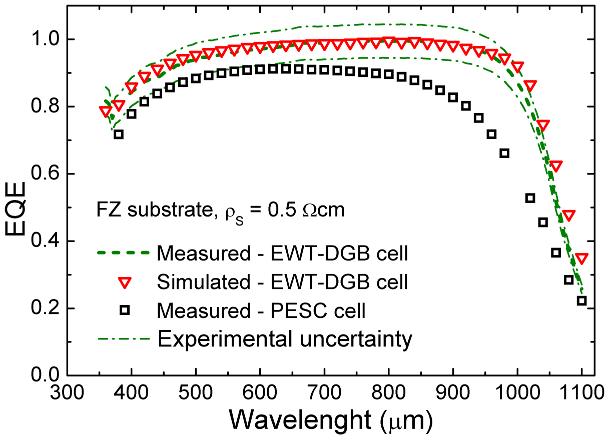

Figure 4.7: Simulated (red triangles) and measured (green-dashed line) EQE with the corresponding bounds of the experimental uncertainty (green dashed-dotted lines) of EWT-DGB FZ solar cell. Measured EQE of a PESC cell [50] used as reference baseline is also illustrated.

Finally, a better hole passivation is expected to significantly lower the recombination current densities J_{01}, J_{02}, and J_{03} and thus to increase the V_{OC}. Roughly, for the Cz substrate cell, it has been estimated the contributions to V_{OC} degradation due to edge recombination losses and due to those in the n-hole region as 5 mV (J_{0H} = 0 A/cm^2, diode D_H OFF) and 60 mV (by assuming for the n-hole region the same lifetime of the bulk region), respectively. Again, a better passivation for holes internal surfaces (e.g., Hole SRV = 100 cm/s) potentially leads to an increase in V_{OC} of approximately 10 mV. Overall, according to simulations, thanks to the enhancement in terms of V_{OC}, an efficiency above 19% at 1 sun is potentially reachable (Cz substrate). For the FZ substrate, this would mean a conversion efficiency above 20%.

4.3.2.1 External and internal quantum efficiency

The external quantum efficiency (EQE) characteristic is reported in Fig. 4.7, where the accordance between the experimental and calculated behavior values is observable. It is worth reporting that no further calibration process of the parameters assumed into simulations has been performed to satisfactory fit the measured data. As comparison, the EQE curve of a conventional PESC cell [50], with same physical dimensions, fabricated on the same FZ silicon substrate and by using a similar technological process, is reported in the figure and used as reference baseline. It is worth noting the higher EQE of the EWT-DGB structure (in particular, in the IR portion of the spectrum) with respect to the PESC cell. This enhancement can be explained by i) the higher optical absorption in the whole spectrum due to suppression of the front metal grid and ii) the higher collection efficiency of the EWT-DGB layout for the IR photogenerated carriers as confirmed by the analysis of the simulated internal quantum efficiency (IQE). In a standard PESC scheme, the electron–hole pairs generated in the deep region of the substrate by red and IR photons are not completely collected due to the limited bulk lifetime. On the other hand, in the EWT-DGB cell, the n-hole pitch is smaller than the substrate thickness; therefore, the red and IR generated pairs are effectively collected by the vertical emitter along the n-hole. It is worth noting that, as confirmed by the relatively enhanced EQE, the marked recombination losses observed in the fabricated samples and previously discussed affect mainly V_{OC} rather than J_{SC} (approximately 40 mA/cm^2 starting from a calculated photogenerated current density of 41.1 mA/cm^2). In addition, the adoption of a more effective antireflection coating layer (for instance, a double-layer SiO_2/SiN_x [118], [119], [120]) is expected to enhance J_{SC} up to 42 mA/cm^2. This option is required in order to obtain short circuit current density values comparable with state-of-the-art solar cells, even with front contact [45].

4.3.2.2 Impact of interfacial defects on FOMs

Numerical simulations are exploited to investigate the effect of interfacial defects on the cell FOMs. Such defects are accounted for by imposing a surface recombination velocity (surface SRH model) at each interface including front, back passivated and holes interfaces. In this study, only the case of $h_s = 50$ μm is considered. Fig. 4.8 shows the impact of the SRV of the cell front interface and of the back passivated interface on FOMs while Fig. 4.9 illustrates the impact of the SRV of the hole surfaces. A negligible impact in terms of J_{SC} and FF is observed except for the case of the front SRV where J_{SC} variations justify the efficiency trend. Moreover, holes SRV significantly affects V_{OC} and then the efficiency. It is worth noting that a simultaneous reduction of the studied (front, back and hole interfaces) SRVs down to $1 \cdot 10^3$ cm/s leads to an efficiency increase up to $19\%_{abs}$.

4.3.2.3 Hole spacing impact

The adopted values of physical parameters discussed in the section 4.3 allow to satisfactory reproduce, by means of numerical simulation, the measured dark J-V characteristic of the EWT-DGB cell featuring h_s of 50 μm. In addition, two further EWT-DGB solar cells featuring h_s of 43 μm and of 78 μm have been characterized at 1-sun. By starting from the same physical parameters successfully tuned for the $h_s =$ 50 μm cell, numerical simulations of the other two EWT-DGB cells featuring h_s of 43 μm and of 78 μm are carried out under both dark and 1-sun illumination conditions. Simulations do not show any difference in terms of recombination losses between the two smaller hole spacing 43 μm and 50 μm. On the contrary, simulations confirm that, by increasing the hole spacing up to 78 μm, the J_{01} contribution significantly

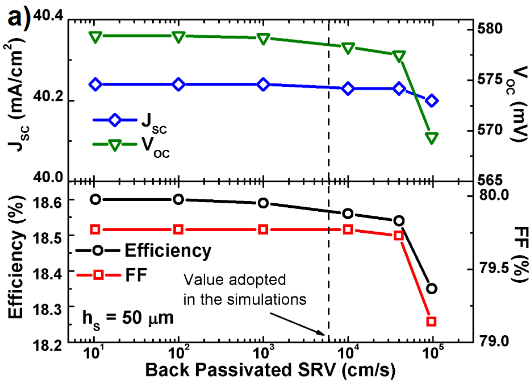

Figure 4.8: (a) Simulated values of Figure of Merit (FOMs) the considered EWT-DGB solar cell (hole spacing $h_s = 50\ \mu$m) versus Surface Recombination Velocity (SRV) at back passivated interface; (b) Simulated values of figures of merit (FOMs) the considered EWT-DGB solar cell (hole spacing $h_s = 50\ \mu$m) versus Surface Recombination Velocity (SRV) at front interface. The black dashed lines denotes the SRV values used for the simulation of the baseline cell ($h_s = 50\ \mu$m) which reproduce the experimental data.

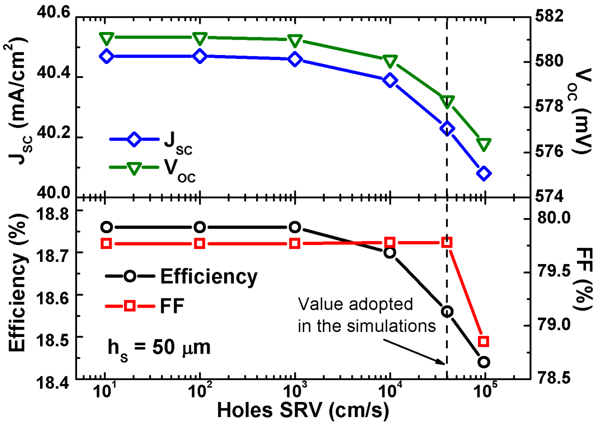

Figure 4.9: (a) Simulated values of figures of merit (FOMs) the considered EWT-DGB solar cell (hole spacing $h_s = 50\ \mu$m) versus Surface Recombination Velocity (SRV) at p- and n-hole interface. The black dashed lines denotes the SRV values used for the simulation of the baseline cell ($h_s = 50\ \mu$m) which reproduce the experimental data.

Table 4.4: Measured and simulated FOMs of the considered EWT-DGB solar cells for the three different hole spacing h_s considered in this study. The relative uncertainties of experimental values are indicated in the brackets.

h_s (*μm*)	FZ substrate	V_{OC} *(mV)*	J_{sc} *(mA/cm²)*	FF *(%)*	Efficiency *(%)*
43	Measured	575 (1%)	38.9 (2%)	81.1 (5%)	18.1 (5%)
43	Simulated	575	39.9	80.5	18.5
50	Measured	582 (1%)	40.1 (2%)	79.6 (5%)	18.6 (5%)
50	Simulated	578	40.2	79.7	18.6
78	Measured	597 (1%)	38.5 (2%)	80.4 (5%)	18.5 (5%)
78	Simulated	595	40.7	81.3	19.5

decreases. In detail, this reduction is ascribed to the lowering of recombination losses in the substrate and in both holes' regions.

It is worth reporting that, the total dark current density at low-voltage bias ($<$ 0.5 V) is not strictly related to the hole spacing. As a matter of fact, the dark J-V characteristic at relatively low bias is dominated by recombination in the n-hole region which are affected by etching process conditions. In order to reproduce the measured dark J-V characteristics, the n-hole region effective lifetime has been therefore finely tuned.

Table 4.4 reports the measured FOMs of the three fabricated EWT-DGB cells (h_s = 43 μm , 50 μm and 78 μm). In addition, the results of the simulation under 1-sun illumination are also shown for the corresponding different geometries, obtained by adopting the physical models used for the dark J-V characteristic fitting of the h_s = 50 μm case (section 4.3).

The V_{OC} is equal to 595 mV in case of h_s = 78 μm and it decreases down to 575 mV by reducing the hole spacing, as predicted by simulations. This reduction in V_{OC} can be explained in terms of J_{01} reduction and of lower recombination losses in the region around n-holes (n-hole region). The conversion efficiency is in the range of 18.1% - 18.6% for all the samples, even though simulations suggest an higher efficiency for the samples with larger h_s.

In terms of FF, the n-hole region limits the FF in case of h_s = 50 μm while for the h_s = 43 μm and h_s = 78 μm cases higher FF is observed. Simulations show that samples with higher hole spacing have better overall performance. On the other hand, cells with lower h_s could be preferred under concentrated light, where the parasitic resistance of the substrate limits the conversion efficiency. By analysing the simulated FOMs it can be noticed that in the case h_s = 50 μm simulations are in agreement with the experimental data within the considered uncertainties.

As discussed in section 4.2, in order to obtain a satisfactory FOMs fitting (especially in terms of FF) also for h_s = 43 μm and h_s = 78 μm cases, a further fine tuning of the n-hole region lifetime is required to take into account for the samples variability of the defects occurring in that region.

4.3.3 Considerations

In these first three sections (4.1-4.3), a novel cell scheme based on the EWT concept, where a hole matrix arranged in two alternating doping type (p and n) is fabricated by means of the DRIE technique has been presented. The fabricated solar cell allows to increase the charge carriers collection efficiency and reduce the front metal-grid shadowing thanks to the back contact option. Moreover, p-holes act as collecting electrodes, allowing a reduction of the resistive losses due to the substrate, feature particularly important for CPV applications. Thick substrates with low lifetime (about 60 μs) are used to produce cells approaching 19% efficiency and FF of 80% under 1-sun illumination and ensure an efficient photon absorption within the spectrum from UV to IR. The measured EQE confirms the advantages of this design in terms of carries collection in particular in the red and IR portion of the spectrum. Starting from experimental data of two EWT-DGB solar cells, fabricated with FZ and Cz substrates, a 3-D numerical simulation flow that allows reproducing the measured dark and illuminated J–V characteristics of the two considered solar cells has been develpoed. It has been observed that the open-circuit voltages of these cells are mostly influenced by the recombination losses due to defects in the region around the n-hole, by the edge recombination effects (especially for low-doped substrates), and by recombination at hole surfaces. Although the fabricated samples show conversion efficiency lower than those exhibited by state-of-the-art industrial screen-printed solar cells, it is important to note that this first production was mainly aimed to test an innovative layout, never proposed before.

First experimental data are encouraging and have driven optimization of the numerical models. According to new simulations, an optimized process is expected to provide a marked increase of the V_{OC} as well as 1-sun efficiency above 20% (FZ substrate).

Finally, a more effective antireflection coating layer will be helpful to attain an increase in short-circuit current density (up to 2 mA/cm^2).

In the following section, a detailed analysis of EWT-DGB solar cells under concentrated light on the basis of experimental data is presented. In addition, the EWT-DGB technology has been compared to the PESC concept by means of numerical simulation in order to highlight the expected advantages of the usage of EWT-DGB scheme under concentrated light.

4.4 EWT-DGB solar cell at low and medium concentration and comparison with a PESC architecture

In this section, after first numerical simulations aimed at demonstrating that the depth of the p-type holes plays a crucial role in terms of the reduction of resistive losses under concentration light, the experimental characterization and the numerical simulation flow under concentrated light of the EWT-DGB and PESC solar cells are reported and discussed. Furthermore, PESC and EWT-DGB silicon solar cells are compared by using a calibrated numerical simulations tool successfully validated by a comparison with experimental data under one-sun and under concentrated light.

The simulations are exploited to study the FOMs of both schemes by removing the limitations due to the process non-idealities, still under realistic assumptions for physical and electrical parameters. Advantages and disadvantages of both solar cell architectures are discussed by means of the calculation of the FOMs under concentrated irradiation, a comprehensive current and power loss analysis and a study of the underlying physical mechanisms. In addition, in the comparison the record Si BC-BJ cell, as a reference for silicon CPV is included.

Finally, an analysis of the impact of the distance between alternatively doped holes (hole spacing) for the EWT-DGB solar cells is carried out by means of numerical simulations. The relevance of substrate resistivity and of the defects located in the region close to the n-doped hole is investigated.

4.4.1 EWT-DGB solar cell: first simulations under concentrated light

Since EWT-DGB solar cells are conceived for CPV applications as stated in section 4.1, in this part, the calibration process adopted and described in 4.1 is initially exploited in order to study by means of numerical simulations the performance under concentrated light. Fig. 4.10 shows the simulated efficiency at T = 298 K as a function of the concentration factor (CF) for the cells fabricated on both Cz and FZ substrates. The cell fabricated on the FZ low resistivity wafer exhibits efficiency peaked at 44 suns, attaining considerably value (21.4%); the conversion efficiency is higher than 21% in the range 20–150 suns. The cell fabricated on Cz wafer shows efficiency equal to 19.4% at 25 suns. Interesting, the efficiency is higher than 18% up to 150 suns, despite the high resistivity of 10 Ωcm. A conventional PESC cell with such high resistivity would have a much lower efficiency due to the parasitic ohmic losses in the substrate. According to experimental data, at 25 suns, the Cz cell exhibits a series resistance ($R_{s,tot}$) equal to 59 mΩcm^2, which is markedly higher than that of the FZ cell (21 mΩcm^2). Measured $R_{s,tot}$ is in excellent agreement with the simulated data. The presence of the deep grooved p-doped holes in the EWT-DGB cell effectively reduces the substrate ohmic losses of the cell. This is confirmed by simulations; for instance, for the Cz cell at 25 suns (T = 298 K), reducing the

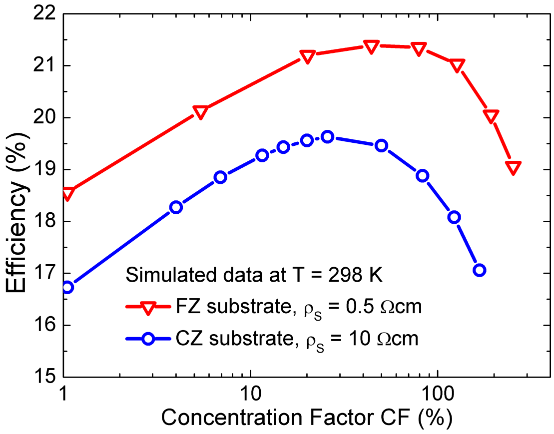

Figure 4.10: Simulated efficiency as a function of the CF for both FZ (substrate resistivity ρ_S = 0.5 Ωcm) and Cz (ρ_S = 10 Ωcm) substrates, by assuming constant temperature T = 298 K.

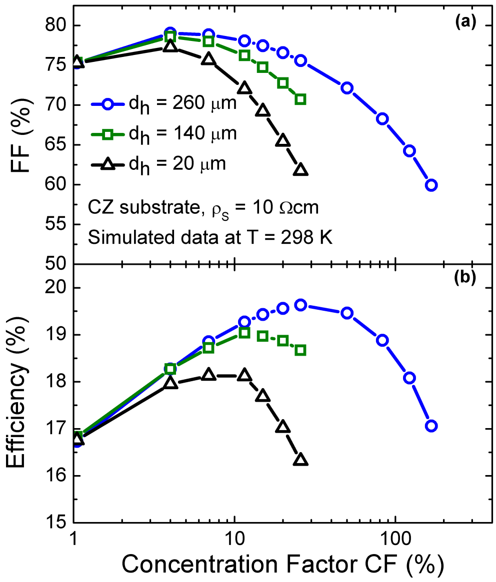

Figure 4.11: Simulated (a) FF and (b) efficiency as a function of the CF for Cz substrate (substrate resistivity ρ_S = 10 Ωcm) by assuming constant temperature T = 298 K. Three different values of p-hole depth d_h have been considered.

p-hole depth (d_h) from 260 to 140 μm results in an increase of the overall $R_{s,tot}$ by 53 mΩcm^2. By reducing the depth to 20 μm, a further increase in $R_{s,tot}$ by 83 mΩcm^2 is estimated. This effect is clearly shown in Fig. 4.11, where the impact of the p-hole depth (d_h) on the conversion efficiency is investigated.

Two extra structures characterized by different p-hole depth (d_h: 140 μm and 20 μm) are simulated and reported in the figure. Deeper p-holes result in higher efficiency and higher FF under concentrated light. Moreover, the efficiency peak moves to higher CF, confirming a reduced series resistance. The considered upper boundary of d_h (260 μm) represents the deeper feasible value whithout compromising the integrity of the device.

4.4.2 Comprehensive simulation metholodgy under concentrated light

As reported in section 4.3, where the cells have been characterized under one-sun illumination, the first run of fabricated EWT-DGB cells is affected by significant recombination effects. The recombination occurring in the highly defective region around the n-hole affecting V_{OC}, as well as the edge recombination ascribed to parasitic lateral effects related to the cell package, is accounted for in the simulation. In particular, it has been considered a region around the n-type-doped hole where an effective carrier lifetime ($\tau_{\text{n-H}}$) value is set as tuning parameter to reproduce the experimental value of dark saturation current density. This region is few nanometres deep and includes the depletion region of the n^+–p junction. Self-heating affecting the cell during experimental characterization is modelled according to [50], by considering the thermal resistance of cell package. The temperature increase (ΔT) of the cell is calculated as a function of CF according to $\Delta T = (d_{eg} / k_{eg}) \text{ x } I_P$, where d_{eg} and k_{eg} are the thickness and the thermal conductivity of the test fixture, respectively, and I_P is the incident power density at given CF. A nominal values of test fixture thermal conductivity and thickness of $1.6{\cdot}10^{-2}$ W/cm/K and 230 μm, respectively, have been assumed, as discussed in [50]. Regarding numerical simulation metodology, in this section an additional validation of the simulation approach is provided by comparing simulation results to measured data under concentration for the EWT-DGB cell, as reported in the next subsection, where a comparison with the experimental results for the PESC cell [50] is reported as well.

4.4.3 Experimental characterization under concentrated light

The experimental data for EWT-DGB solar cells under concentration have been obtained by the same measurement setup used for the PESC cell, described in [50]. In Fig. 4.12 a sketch of the EWT-DGB solar cell is reproposed together with a PESC scheme. Both PESC and EWT-DGB solar cells experimentally characterized feature 16 mm^2 area and have been fabricated in a CMOS-like pilot line on 280-μm-thick 4-inch c-Si wafers. The nominal geometrical parameters of the considered

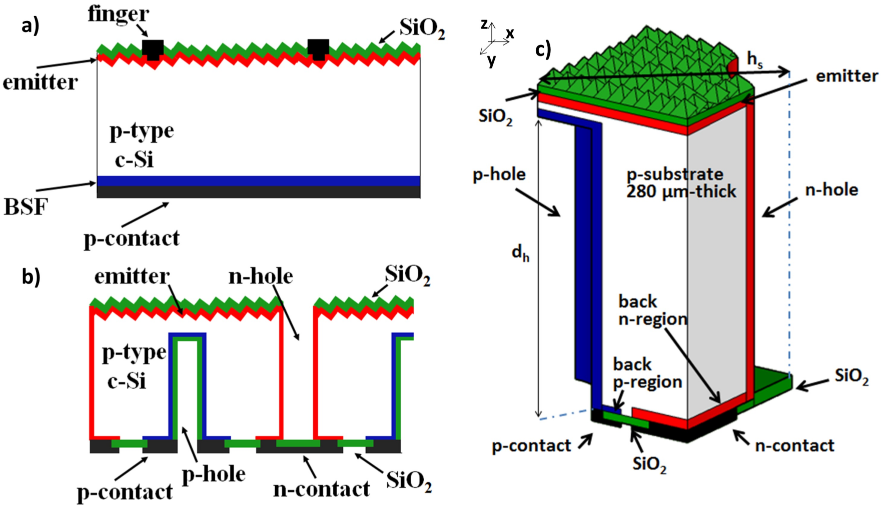

Figure 4.12: Vertical cross section of PESC cell (a) and of EWT-DGB cell (b). In (c), a 3-D sketch of EWT-DGB simulation domain is reported (not in scale).

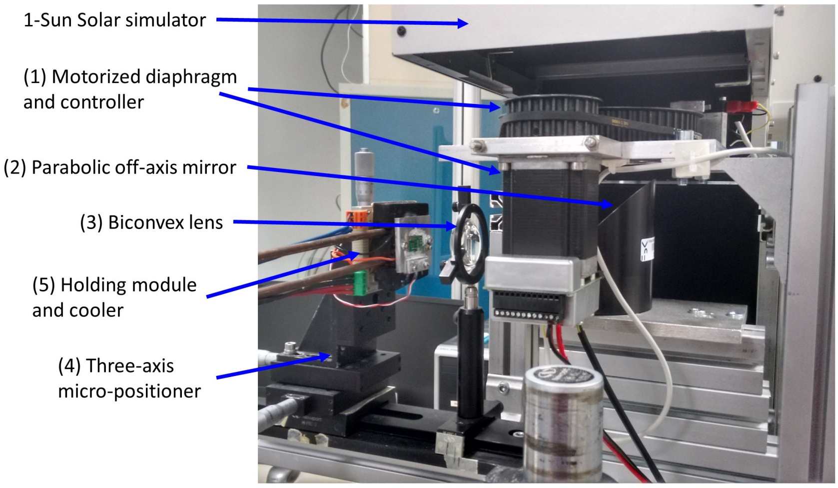

Figure 4.13: Picture of the concentrator system for cell characterization. The system is composed of a motorized diaphragm (1), a parabolic off-axis mirror (2), a biconvex lens (3), a micropositioner (4) and a thermal cell holder (5) that holds the packed cell.

EWT-DGB solar cell are listed in Table 4.1. The PESC solar cell (Fig. 4.12(a)) has been fabricated on FZ p-type wafers (resistivity of 0.5 Ωcm). The main parts of the fabrication process of EWT-DGB solar cell, including the three lithographic steps as well as the boron and phosphorous diffusions, surface texturing and the contact definition, are extensively described in section 4.2. Details of PESC solar cells are reported in [50].

With reference to Fig. 4.13, the concentrating system is composed of a motorized diaphragm (1), a parabolic off-axis mirror (2), a biconvex lens (3), a three-axis micropositioner (4) and a cooled holding module (5) which holds the packed cell (6). By tuning the diaphragm aperture, combined to the concentrating optics, the final irradiance can be directly controlled.

Such a system produces a spot on the 4 x 4-mm^2 test cell plane with a 10% spatial uniformity. The light source is supplied by a steady-state solar simulator (Abet Sun 2000 Solar simulator), while the AM1.5D direct spectrum with an irradiance of 1000 W/m^2 per sun as required by the ASTM standard G173-03 [121] is used during the measurements. The back side of the cell has been connected by means of silver-loaded adhesive to a dedicated printed board circuit, designed to allow four-wire electrical measurements, whereas the front metal is connected by wire bonding. Although the printed board circuit was kept at a constant temperature of 298 K, for concentration factor above 100 suns, the cell temperature increases due to self-heating and to the thermal resistance of the cell and of the adhesive. The effective cell temperature has been considered in numerical simulations as described in the previous subsection.

The measured FF and efficiency of the EWT-DGB cells are reported in Fig. 4.14 for both FZ and Cz substrates. Fig. 4.15 shows the open circuit voltage V_{OC} and the short circuit current density J_{SC}. The cell fabricated on the FZ low-resistivity wafer exhibits a significant 21.4% efficiency peak at 44 suns; the conversion efficiency is higher than 20% in the 20–100 sun range. The EWT-DGB cell fabricated on Cz wafer, despite of the relatively higher resistivity substrate, provides 19% efficiency at 25 suns. FF is $5\%_{abs}$ higher in the FZ substrate case, with respect to the Cz one, mainly due to lower resistive losses. The V_{OC} dependence on CF is illustrated in Fig. 4.15 (a) and (c). It can be observed that cells fabricated on FZ wafers feature larger V_{OC} thanks to lower recombination losses.

The FOMs under concentrated light of the PESC cells are reported in Fig. 4.16 and Fig. 4.17. It can be noted that 22.0% efficiency is attained at about 80 suns and a plateau of the efficiency–CF curve is observable in the 60–100 sun range. The FF is reduced by the enhanced resistive power loss as the irradiance increases, while the V_{OC} suffers from the increase of bulk and surface recombination due to significant self-heating effect occurring above 100 suns. The agreement between simulations and experimental data is excellent and always within the measurement confidence interval, confirming the accuracy of the numerical calculations.

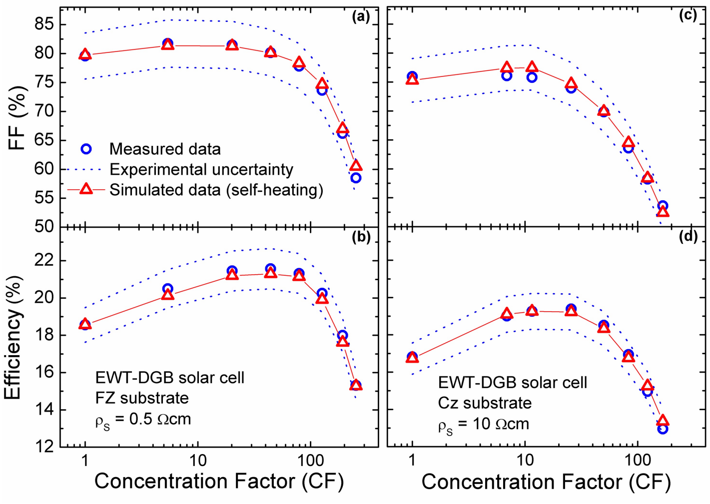

Figure 4.14: EWT-DGB: measured (blue circles) and simulated (red triangles) fill factor (FF) (a) and efficiency (b) versus concentration factor CF for FZ substrate ($\rho_S = 0.5\ \Omega$cm) and (c, d) for Cz substrate ($\rho_S = 10\ \Omega$cm); simulations include the self-heating effects.

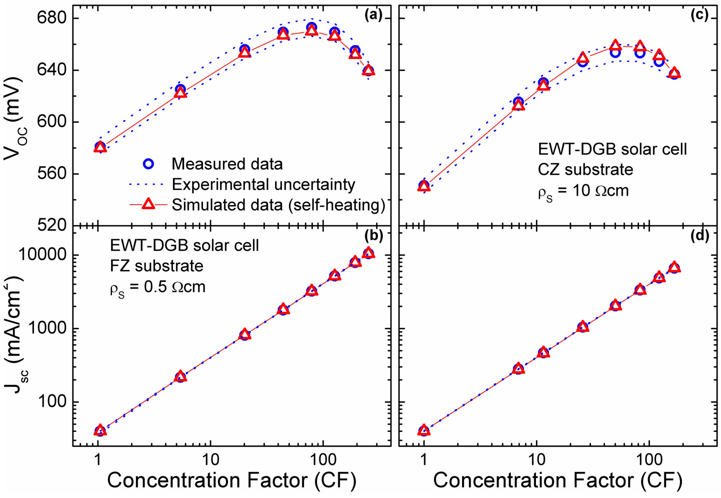

Figure 4.15: EWT-DGB: measured (blue circles) and simulated (red triangles) open circuit voltage (V_{OC}) (a) and short circuit current density (J_{SC}) (b) versus CF for FZ substrate ($\rho_S = 0.5\ \Omega$cm) and (c, d) for Cz substrate ($\rho_S = 10\ \Omega$cm); simulations include the self-heating effects.

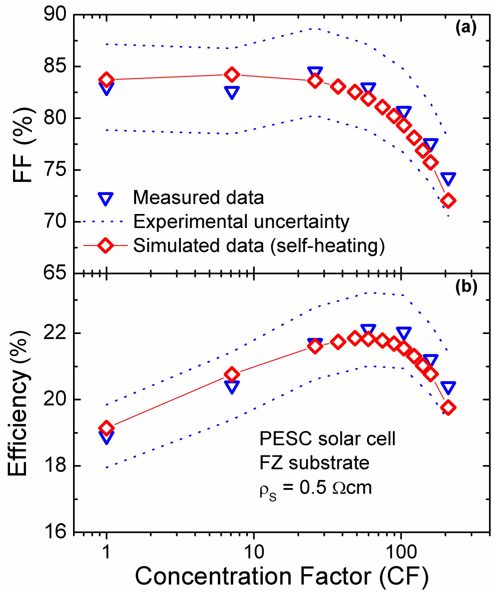

Figure 4.16: PESC: measured (blue triangles) and simulated (red diamonds) fill factor (FF) (a) and efficiency (b) versus concentration factor CF for FZ substrate (ρ_S = 0.5 Ωcm), reported in [50]; simulations include the self-heating effects.

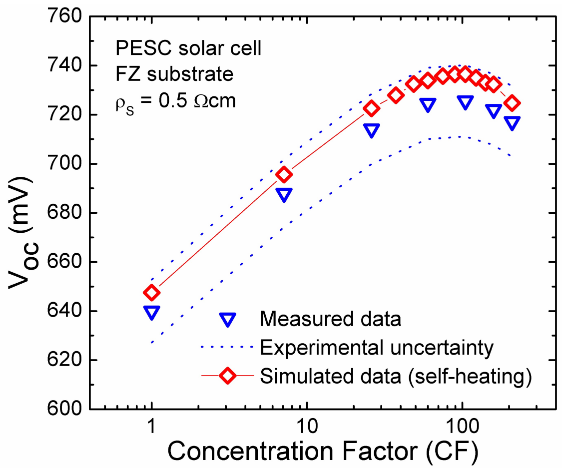

Figure 4.17: PESC: measured (blue triangles) and simulated (red diamonds) open circuit voltage V_{OC} versus concentration factor CF for FZ substrate (ρ_S = 0.5 Ωcm), reported in [50]; simulations include the self-heating effects.

4.4.4 Limitations of the fabricated devices and possible improvements

Although the samples from the first fabricated batch shows conversion efficiency lower than those exhibited by state-of-the-art Si solar cells, under both one-sun and concentration conditions, the experimental data of the fabricated PESC and EWT-DGB are encouraging. In particular, based on results obtained from these first fabricated devices, it is possible to identify and possibly correct their more relevant limitations.

First of all, it can be observed that the adopted microfabrication technology is based on some conventional CMOS techniques (thermal oxide-based ARC and passivation, boron diffused back surface field), not optimized for solar cell processing. In this regard, the adoption of a more effective ARC, such as a double-layer ARC (DARC) composed of a SiO_2/SiN_x stack, would certainly enhance the light absorption by significantly decreasing optical losses.

Secondly, as already discussed in the section 4.3 for the characterization of EWT-DGB solar cells at 1-sun, the relatively low V_{OC} values obtained by EWT-DGB are mainly ascribed to excess recombination in highly defective n^+-hole regions. This limitation could be alleviated by adopting an optimized fabrication process that reduces the damage introduced during the reactive ion etching process and, at the same time, by lowering the doping concentration of n^+-hole regions.

Finally, improving the substrate quality may also play a key role in terms of efficiency increase for both PESC and EWT-DGB.

In the following, in order to investigate the potentials of PESC and EWT-DGB architectures, four possible feasible improvements with respect to the first fabrication run are considered:

(i) Enhancement of photon absorption by adoption of a DARC.

(ii) Significant decrease of recombination losses in the n-hole region of EWT-DGB by assuming an improved fabrication process (reactive ion etching) in combination with a reduction of doping concentration of n^+-hole regions.

(iii) Reduction of recombination at the edge region of the EWT-DGB cells.

(iv) Better front and hole surface passivation.

From experiments it has been observed that the 1-sun short circuit current density (J_{SC}) values are closer to 35 and 40 mA/cm^2 for PESC and EWT-DGB cells, respectively. These values are significantly lower than those of the state-of-the-art solar cells reported in literature [87]. By assuming the presence of a DARC (87 nm of SiO_2 as top layer on 57 nm of SiN_x [118], [120]) featuring regular upright pyramids with a 10-μm-wide base and opening angle between two faces of the pyramid of 70.5°, the resulting simulated one-sun J_{SC} increases to 37.7 and to 41.9 mA/cm^2 for PESC and EWT-DGB, respectively.

In the case of EWT-DGB, the recombination losses at the device edges and in the region around the n-type-doped holes, where high concentration of defects is localized, are responsible for a degradation of V_{OC} by approximately 5 and 60 mV at one sun, respectively. Both these limiting effects can be reduced by finely tuning the cell design and some features of the fabrication technology. In particular, the edge recombination may be eliminated thanks to a more accurate cell packaging. The high concentration of defects in the region around the n-hole is associated both to the damage introduced by the etching process and to the high phosphorous concentration required for the n^+-hole region. In this regard, a lower defectiveness in the region around the n-hole may realistically considered by assuming the following:

(i) an improved fabrication process (in particular regarding the holes dry etching) by adopting an effective carrier lifetime ($\tau_{\text{n-H}}$) for the region around the n-hole equal to the substrate minority carrier lifetime (τ_{n});

(ii) a lower peak doping concentration in the n-hole region, which leads to a sheet resistance of 30 Ω/sq.

In addition, a better interface passivation would result in lower SRVs. SRVs = $1{\cdot}10^3$ cm/s has been assumed for the hole surfaces and for back passivated surfaces of the EWT-DGB. This value is reasonable, considering the peak doping concentration at interfaces and a good passivation quality.

Furthermore, in the following simulations, a p-type Cz substrate featuring resistivity (ρ_S) of 1 Ωcm with 200-μs minority carrier lifetime (τ_{n}) [114] is considered, a typical value for the most common commercial solar cells [122]. In addition, because EWT-DGB is expected to be less sensitive to substrate resistivity compared with standard PESC solar cells, the case of wafer resistivity ρ_S = 10 Ωcm it has been considered, corresponding to lower doping substrate, that is, higher carrier mobility and larger lifetime. In particular, a τ_{n} = 1 ms is assumed, a typical value for regenerated substrates [114].

Lastly, numerical simulations are performed at a constant temperature of 298 K, assuming the existence of an ideal heat sink, in order to remove the V_{OC} limitation due to self-heating.

In Table 4.5, the parameters used to simulate the process improvements assumed in this section are summarized and compared with their values used for the fitting of the experimental data reported in the previous section.

4.4.5 Comparison between EWT-DGB and PESC solar cells

The simulated FOMs versus CF are summarized in Fig. 4.18 and Fig. 4.19(a), where FF, efficiency and V_{OC} are shown. Moreover, in Fig. 4.19(b), the series resistance (R_s) versus CF, calculated by means of the method proposed by Wolf [123], is reported for both structures. The R_s value represents the total cell series resistance and includes the contribution of the front emitter, the base region and the hole regions (in the case of ETW-DGB), as well as that due to contacts and metal (≈1.8 mΩcm^2 [50]). The 1 Ωcm EWT-DGB solar cell exhibits conversion efficiency

Table 4.5: Comparison between the values of physical and doping parameters adopted in simulations to fit the experimental data (section 4.3) and those used accounting for the possible improvements (this section).

Parameter	Unit	Value: Set used to fit experimental data (Section 4.3)	Value: Set used to simulate the improved solar cells (Section 4.4)
ARC			
SiO_2	nm	105	87 [23]
SiN_x	nm	-	57 [23]
Cz substrate			
Substrate resistivity	Ωcm	10	1
Minority carrier lifetime (τ_n)	μs	190	200 [25]
Surface recombination velocity			
Front emitter	cm/s	$5.8 \cdot 10^3$	$1 \cdot 10^3$
Holes	cm/s	$1 \cdot 10^3$	$1 \cdot 10^3$
Back n-region	cm/s	$3 \cdot 10^4$	$1 \cdot 10^3$
Back p-region	cm/s	$1 \cdot 10^3$	$1 \cdot 10^3$
Defectiveness around the n-hole			
DRIE process		first run (hig defectiveness)	Improved process (low defectiveness)
n-Hole sheet resistance	Ω/sq	15	30
n-Hole effective lifetime ($\tau_{\text{n-H}}$)	μs	0.38	190
Temperature	K	Self-heating	298

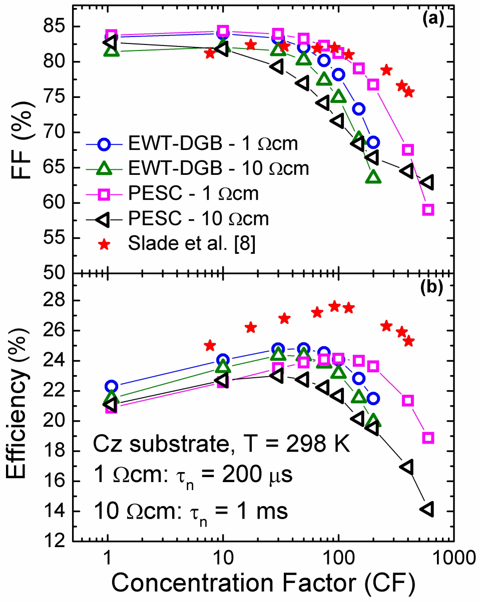

Figure 4.18: Simulated FF (a) and efficiency (b) versus concentration factor CF for ETW-DGB and PESC solar cells for two different Cz substrate resistivity: 1 Ωcm (minority carrier lifetime τ_n = 200 μs) and 10 Ωcm (τ_n = 1 ms). The red stars denote the experimental data reported by Slade [51]. All simulations are performed at temperature T = 298 K.

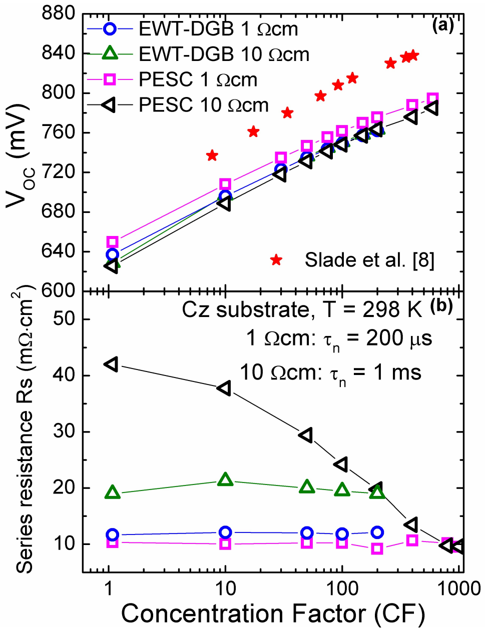

Figure 4.19: Simulated open circuit voltage V_{OC} (a) and calculated series resistance (b) versus concentration factor CF for ETWDGB and PESC solar cells for two different Cz substrate resistivity: 1 Ωcm (minority carrier lifetime τ_n = 200 μs) and 10 Ωcm (τ_n = 1 ms). The red stars denote the experimental data reported by Slade [51]. The series resistance values have been calculated according to [123]. All simulations are performed at T = 298 K.

higher than 24% in the range 10–100 suns, with 24.8% as maximum efficiency at 50 suns (Fig. 4.18(b)). Increasing the substrate resistivity to 10 Ωcm only slightly degrades the FF and the conversion efficiency (Fig. 4.18), thus demonstrating the effectiveness of the EWT-DGB scheme with high-resistivity substrates. The strong drop of efficiency and of FF occurring for CF > 60 is mainly due to both resistance losses and recombination losses, as discussed in the following. The PESC cell on 1 Ωcm substrate features conversion efficiency higher than 23% in the range 25–200 suns with maximum efficiency of 23.9% at 100 suns. However, in the 10 Ωcm case, the efficiency degrades significantly at increasing CF values. In this case, FF is markedly degraded due to the large resistive loss associated to charge transport in the high-resistivity base. Figu. 4.19 (b) shows that in the case of high-resistivity substrates, the series resistance significantly depends on CF. This effect can be explained by considering the dependence of the base resistance on photogenerated carrier concentration. As a matter of fact, by increasing the light intensity, the base resistivity is significantly modulated by the generated carrier densities; therefore, the effective base resistivity decreases with increasing concentration factor. This effect is not observable in the EWT-DGB scheme, which features a R_s constant with respect the CF, because the p-holes and n-holes affect the current path reducing the sensitivity to base resistivity.

Comparing the two designs for low-resistivity substrate, the EWT-DGB cell provides higher efficiency for CF up to 100 suns, while at higher CF values, the PESC scheme is preferable to the EWT-DGB. On the other hand, when high-resistivity wafers are considered, the PESC performance is markedly affected by the resistive losses in the substrate, whereas the EWT-DGB scheme provides better performance in the whole CF range, thanks to its peculiar lower sensitivity to the substrate resistivity.

Finally, a comparison with the record FOM values presented by Slade [51] is worthy of discussion. Although the record cell leads to 27.5% efficiency at 100 suns, substantially higher than both PESC and EWT-DGB solar cells, it should be considered that the latter cells are fabricated by using materials with lower minority carrier lifetime (200 μs for the 1 Ωcm substrate) and, at least in the case of the PESC, an extremely simple fabrication processes. On the contrary, the Slade's cell uses a highly resistive and high-quality 150-μm-thick substrate leading to large V_{OC} values (Fig. 4.19(a)).

4.4.5.1 Resistive, recombination and optical losses

As previously discussed with reference to Fig. 4.18, a significant drop of the EWT-DGB solar cells efficiency for CF > 60 is observed. This behaviour may be explained as the consequence of two factors: (i) losses due to the series parasitic resistance and (ii) increase of the recombination current at high concentration.

Regarding the parasitic resistance losses, as a matter of fact, in the case of 1

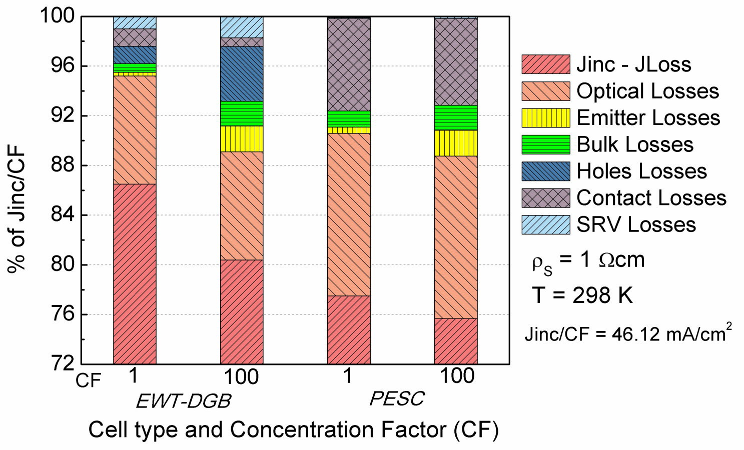

Figure 4.20: Calculated percentage contributions of recombination and optical losses to the total incident current density normalized to the CF (J_{inc}/CF) for EWT-DGB and PESC solar cells (1 Ωcm, at temperature T = 298 K) at both 1 sun and 100 suns. CF = 1: contribution calculated at MPP. CF = 100: contribution at a voltage $V = V_{OC}(CF = 100) \times (V_{MPP}(CF = 1)/V_{OC}(CF = 1)$.

Ωcm substrate, a slightly higher series resistance is found for the EWT-DGB cell with respect to the PESC cell (Fig. 4.19(b)). The thin n-doped regions located along the n-holes favour current crowding for the electrons photogenerated close to the surface, thus introducing a parasitic series resistance. In order to verify that a considerable contribution to the series resistance arises from the n-doped holes, numerical simulations have been performed by assuming the EWT-DGB structure of Fig. 4.12 with a metallic via instead of the n-type hole, obtaining a decrease of series resistance, a $2\%_{abs}$ increase in FF and a consequent shift of the optimum CF towards higher values.

In addition to the resistive losses, the optical and recombination losses of the 1 Ωcm EWT-DGB and PESC solar cells at CF = 1 and CF = 100 are analysed. Fig. 4.20 reports the optical and recombination losses expressed as percentage of the incident current density (J_{inc}) normalized to CF. For CF = 1, the optical and electrical losses occurring at the maximum power point (MPP) are calculated. In such a case, if J_{inc} denotes the incident current density, the difference J_{inc} - J_{losses} is equal to J_{MPP}. For CF = 100, losses have been calculated at a voltage given by $V = V_{OC}(CF = 100) \times V_{MPP}(CF = 1)/V_{OC}(CF = 1)$. This assumption was made in order to fairly compare the current loss mechanisms responsible for the FF degradation when the cell operates under concentration with respect to the one-sun condition. In the case of the EWT-DGB solar cell, light concentration increases the impact of carrier recombination (surface, Auger and SRH recombination) along both p-holes and n-holes and affects the cell efficiency at high concentration factors. The PESC cell exhibits marked optical losses, related to front-contact shadowing, and significant contact losses, but the recombination currents are only slightly dependent on the concentration factor.

Comparing the two structures, it can be noticed that, as expected, the EWT-DGB cell provides a higher available current density at contacts (J_{inc}-J_{losses}) with respect to the PESC one, mainly thanks to lower optical losses. For a thorough comparison between the two structures, Table 4.6 reports the values of the relative power losses at MPP for their respective optimum CF value (CF = 50 for the EWT-DGB and 100 for the PESC) evaluated in different cell regions. It appears that the power losses in the PESC cell are mainly due to optical shading and recombination at the contacts. On the other hand, the EWT-DGB scheme features low relative power losses in both bulk region and emitter region, whereas the hole regions are responsible for a 4.2% degradation. Finally, the PESC cell suffers higher series resistance power losses at MPP and optimum CF, compared with EWT-DGB (5.6% instead of 3.8%).

Table 4.6: Power loss analysis at MPP condition in the case of optimum concentration factor. Power loss is calculated as the product of loss current density by internal cell voltage $V = V_{MPP} + R_s J_{MPP}$. The relative power loss is calculated taking the power density at MPP ($V_{MPP} \cdot J_{MPP}$) as reference. The relative power-loss due to series resistance is calculated in terms of FF reduction by the equation $1.1 \cdot (R_s J_{SC}/V_{OC})$ according to [124]. For each region, the loss values refer to recombination losses.

	Power Loss (mW/cm^2)		Relative Power Loss ($\%$)	
cell	EWT-DGB	PESC	EWT-DGB	PESC
suns	50	100	50	100
Optical Losses	104.8	877.5	10.3	36.3
Emitter Losses	16.5	64.5	1.6	2.7
Bulk Losses	27.6	89.4	2.7	3.7
Hole Losses	42.9	-	4.2	-
Back/BSF losses	1.8	6.5	0.2	0.3
Contact losses	16.3	270.5	1.6	11.1
Tot. recomb. losses	105.2	430.9	10.3	17.8
Ohmic losses	26	206.4	3.8	5.6

4.4.5.2 Minority carrier lifetime sensitivity

In Fig. 4.21, the effect of the minority carrier lifetime τ_n, related to the substrate quality, on the FF and efficiency of the two considered cell architectures is investigated. As reported in Fig. 4.21(a), the FF is rather independent of τ_n. The conversion efficiency of the PESC cell is much more sensitive to lifetime compared with the EWT-DGB, due to the dependence of V_{OC} and J_{SC} on τ_n, as depicted in Fig. 4.22. In detail, the marked sensitivity of the J_{SC} on the substrate lifetime of

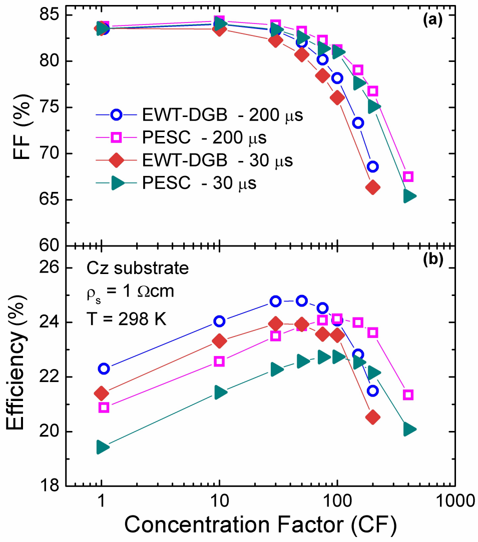

Figure 4.21: Simulated fill factor (FF) (a) and efficiency (b) versus concentration factor CF for 1 Ωcm ETW-DGB and PESC solar cells for two different minority carrier lifetimes τ_n: 200 and 30 μs. All simulations are performed by assuming constant temperature T = 298 K.

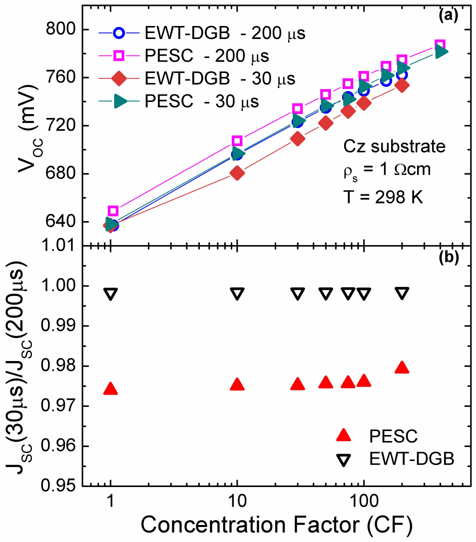

Figure 4.22: Simulated open circuit voltage V_{OC} (a) versus concentration factor CF for 1 Ωcm EWT-DGB and PESC solar cells for two different minority carrier lifetimes τ_n: 200 and 30 μs. In (b), the short circuit current density ratio J_{SC} (30 μs)/ J_{SC} (200 μs) versus concentration factor CF for 1 Ωcm EWT-DGB and PESC solar cells is illustrated. All simulations are performed by assuming constant temperature T = 298 K.

the PESC cell with respect to the EWT-DGB cell is noticeable in Fig. 4.22(b). The lower sensitivity to wafer quality exhibited by the EWT-DGB cell is mainly due to the reduced distance between holes of opposite type (hole spacing). In particular, this distance is much shorter than substrate thickness (280 μm), improving the collection efficiency of minority carriers photogenerated in the cell's base. Consequently, the proposed EWT-DGB can provide good performance even in the case of low-cost substrates featuring minority carrier lifetime (i.e. 30 μs, a typical lifetime value for degraded material [114]).

4.4.6 EWT-DGB solar cell: sensitivity to the hole spacing

In the introductive part of this chapter, it has been underlined that a key feature of EWT-DGB with respect to a standard EWT topology is represented by the presence of the p-holes. A simulation study aimed at investigating the dependence of EWT-DGB cell performance on the hole spacing h_s (Fig. 4.3) is discussed in the following. By exploiting numerical simulations, it is analysed how solar cell FOMs under concentrated light are affected by the hole spacing for different values of substrate resistivity and of recombination rates associated to defects localized in the region surrounding the n-hole. As pointed out in section 4.3, the level of defectiveness in such region is strongly related to the quality of the etching process used to fabricate holes. As a matter of fact, substrate resistivity and lifetime degradation introduced by etching process have a marked impact on the choice of the hole pattern density. In particular, h_s within the range 28–78 μm is considered. Longer spacing is not meaningful because the distance between p-type and n-type holes should be much lower than the substrate thickness.

In Fig. 4.23(a) and (b), the FF and the efficiency of the EWT-DGB solar cell for five different h_s values are shown for two different values of substrate resistivity (1 and 10 Ωcm) calculated for concentration factor CF = 75. A maximum for conversion efficiency is obtained for h_s close to 40 μm. By increasing further the spacing between holes, the substrate resistivity significantly degrades both FF and efficiency. In addition, higher h_s leads to a lowering of CF value at which the peak of efficiency occurs (Fig. 4.23 (c)). A short hole spacing mitigates the resistive losses due to the substrate, leading to (1) FF enhancement and (2) a shift of the peak of efficiency towards higher CF. On the other hand, for h_s values below 40 μm, a decrease of J_{SC} and V_{OC} becomes dominant, causing a reduction of the conversion efficiency. In fact, low h_s is counter productive for light absorption due to a reduction of the volume of absorbing material. The second analysis performed deals with the sensitivity of the EWT-DGB performance to the hole spacing depending on the defectiveness level in the region around the n-hole. Into the proposed simulations, the damage rate in such region of interest (including the depletion region of the n^+-p junction) is modelled by adopting a fine tuning of an effective charge carrier lifetime

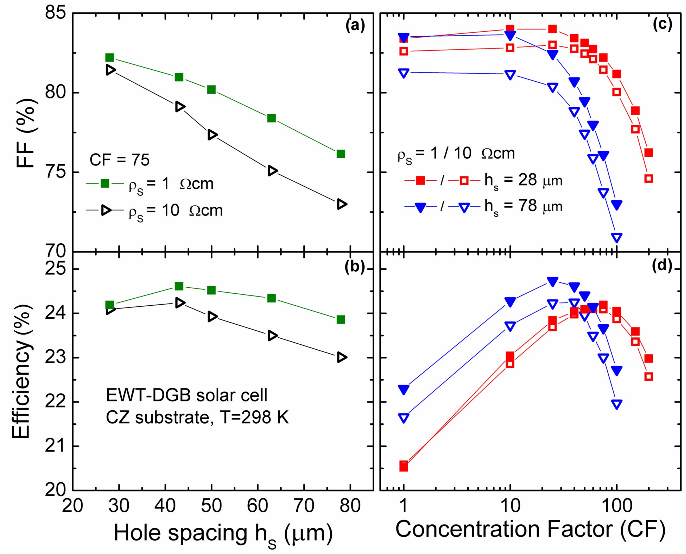

Figure 4.23: Simulated fill factor (FF) (a) and efficiency (b) versus hole spacing hs for 1 Ωcm (filled symbols) and 10 Ωcm (open symbols) EWT-DGB solar cell at concentration factor CF = 75. In (c) and (d), the simulated FF and efficiency are plotted against the concentration factor CF for two values of h_S: 28 μm (red squares) and 78 μm (blue triangles), for two different substrate resistivity: 1 Ωcm (filled symbols) and 10Ωcm (open symbols). All simulations are performed by assuming constant temperature T = 298 K.

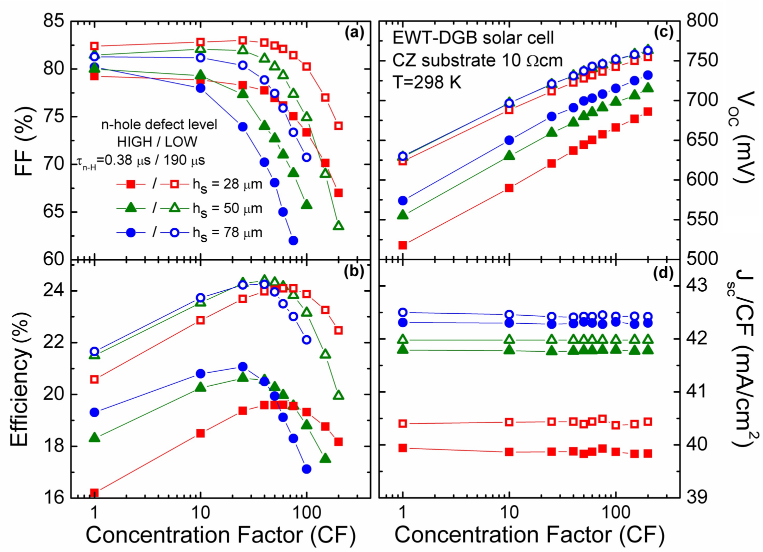

Figure 4.24: Simulated fill factor (FF) (a), efficiency (b), open circuit voltage V_{OC} (c) and short circuit current density normalized to the concentration factor J_{SC}/CF (d) versus concentration factor CF for 10 Ωcm EWT-DGB solar cell for three different hole spacing h_S values: 28 μm (red squares), 50 μm (green triangles) and 78 μm (blue circles). The filled symbols refer to a high defectiveness in the region around the n-hole (effective lifetime $\tau_{n\text{-}H} = 0.38$ μs), while the open symbols indicate a low presence of defects ($\tau_{n\text{-}H} = 190$ μs). All simulations are performed by assuming constant temperature T = 298 K.

($\tau_{\text{n-H}}$) value. The impact of the hole spacing for two defectiveness levels, indicated as high and low level, is investigated. It is worth noting that in this analysis, the high-level defectiveness condition is comparable to that used to reproduce the experimental data of section 4.2 ($\tau_{\text{n}} = 0.38$ μs), while the low-level condition refers to a defectiveness level equal to that used for the bulk region ($\tau_{\text{n-H}} = 190$ μs), as assumed in section 4.2. Fig. 4.24 depicts the FOMs under concentrated light for three values of h_s (where 50 μm is the one used in sections 4.2 and 4.3) for both low and high defectiveness level.

As shown in Fig. 4.24, the FOMs are strongly affected by the presence of defects ($\tau_{\text{n-H}} = 0.38$ μs) localized in the portion of device volume around the n-hole. In particular, for relatively low hole spacing, both FF (Fig. 4.24(a)) and V_{OC} (Fig. 4.24(c)) degrade significantly, and a slight decrease in terms of J_{SC} is observed as well (Fig. 4.24(d)).

Concluding, hole spacing has a relevant impact on efficiency under concentrated light, especially in the case of relatively high-resistive substrates and in the case of highly defective n-holes.

Finally, it may be noticed that, according to Fig. 4.23(b) and Fig. 4.24(b), the hole spacing chosen for the fabricated samples (50 μm) can be reasonably considered a satisfactory value close to the optimum one.

4.4.7 Conclusions

In this section, a preliminar simulation study of the performance of these cells under concentrated light was also carried out. It shown that a maximum efficiency of 21.4% is achieved in the case of FZ substrate for CF of 44, while for the Cz substrate, the maximum efficiency of 19.5% occurs at 25 suns (T = 298 K). Moreover, acceptable efficiency is obtainable up to 150 suns even in the case of highly resistive substrates. In addition, simulations have demonstrated that the depth of the p-type holes plays a crucial role in terms of the reduction of resistive losses under concentration.

Afterward, the physical models used for electro-optical simulations have been validated by means of comparison with experimental data on the first fabrication runs, realized by using Cz and FZ wafers of different resistivity.

Although the first fabricated samples clearly exhibit some limitations mainly due to a non-optimized fabrication technology, the measured efficiency is encouraging. By exploiting TCAD simulations, the FOMs of the PESC and of EWT-DGB cells have been studied by removing the limitations due to the process non-idealities, still maintaining realistic assumptions on physical and electrical parameters. By neglecting the self-heating effect that limits the V_{OC} under high concentration factors, simulations result in an efficiency close to 24% at 100 suns and to 25% at 50 suns for PESC and EWT-DGB, respectively. The main advantages of EWT-DGB with respect to PESC can be summarized in terms of better IR response, low sensitivity to wafer resistivity and quality. They are achieved thanks to the implementation of a matrix of n-holes alternated to p-holes that improves the collection of minority carriers photogenerated in the base. In this way, both the adoption of relatively thick wafers and the absence of front-contact grid optical shading are allowed. In addition, a comparison with the architecture holding the record efficiency for Si-based CPV solar cell [51] is proposed. The presented simulation study confirms that a particularly critical geometrical parameter such as the hole spacing has been chosen reasonably close to the optimum value. In fact, especially in the case of relatively high resistive substrates or highly defective n-holes, the design of the hole matrix pattern strongly influences FF, J_{SC} and the absorption of concentrated light.

According to the obtained results, the EWT-DGB can be adopted for low CF values, in the 10 to 60 sun range. Its conversion efficiency is rather insensitive to the defect density of adopted substrates. On the contrary, PESC solar cells are suitable for concentration factors up to 100. Slade's solar cell, based on a BC-BJ scheme, besides attaining higher peak efficiency, can straightforwardly operate at relatively high concentration factors. However, their superior performance is critically dependent on wafer quality and thickness.

Chapter 5

Modeling of Carrier-Selective contacts solar cells

This chapter presents simulation studies of silicon solar cells featuring carrier-selective passivating contacts based on ultra-thin tunnel oxides. In section 5.1, an introduction to Silicon Solar Cells featuring both top and rear poly-Si/SiO$_x$ carrier-selective contact is presented. Section 5.2 deals with a simulation study aimed at understanding the electrical properties of an experimentally characterized top/rear poly-Si/SiO$_x$ silicon solar cell. The anlyses are carried out by using physical models calibrated on the basis of experimental data. Furthermore, a rear junction (RJ) design which desensitizes the FF to top electrode resistivity is proposed. The results refer to the article published in IEEE Journal of Photovoltaics [125] by the auhor of this thesis. The presented models were developed in close collaboration with Frank Feldmann of Fraunhofer ISE who carried out the experimental characterization of the samples and of the solar cells considered.

5.1 Introduction to Silicon Solar Cells with poly-Si/SiO$_\mathrm{x}$ Carrier-Selective Base- and Emitter-Contacts

Silicon solar cell efficiency has been pushed markedly in the last decade. Heterojunction solar cells (SHJs) [37] and passivating contacts based on a thin oxide and a doped silicon layer (TOPCon) [74], [75], are among the more effective options to enhance the open-circuit voltage (V$_\mathrm{OC}$) well above 700 mV, by notably reducing surface recombination, outclassing point-contact schemes.

Best performing SHJs enable high V$_\mathrm{OC}$ (around 745 mV) thanks to an excellent surface passivation quality, allowing high conversion efficiency [30]. In [126] a SHJ is proposed that guarantees satisfactory electrical properties, by adopting a front transparent conductive oxide (TCO) electrode, ensuring a good contact formation to the amorphous-silicon (a-Si) front contact and providing sufficient lateral conductivity. However, SHJs exhibit considerable drawbacks: i) the limited thermal budget imposed by the a-Si:H passivation to the metallization process step and ii) TCO increases the overall production cost [8]. Solar cells featuring TOPCon or poly-Si/SiO$_x$ [74], [75], may be considered as a valid alternative to SHJs thanks to their improved thermal stability/compatibility with diffusion or firing processes.

Several papers [41], [45], [76], [127], [128], [129], [130], [131], deal with solar cells featuring passivating contacts where the doped silicon layer is composed of poly-Si or SiC$_x$. In terms of efficiency two cell concepts stand out: (i) the combination of a diffused front emitter and a passivating rear contact (TOPCon) (25.7%) [45], [46], (ii) IBC featuring poly-Si/SiO$_x$ junctions (25.0%) [131]. Bifacial textured solar cell with tunnel oxide junction and doped a-Si thin-film emitter layers has been proposed by Silevo group [42] demonstrating efficiency above 23%.

This work, however, deals with a solar cell featuring poly-Si contacts on both sides. Possible advantages are: (i) a lean processing sequence without structuring processing, (ii) high V_{OC} and FF due to passivating contacts (no selective emitter required to reach high V_{OC}s). Unfortunately, a limitation of poly-Si/SiO$_x$ approach is the parasitic light absorption of the poly-Si layer, making the application of the front poly-Si/SiO$_x$ potentially problematic [127]. Lastly, poly-Si is commonly highly resistive. Carrier mobility is limited to a few tens cm^2/V/s dramatically affecting fill-factor (FF). Alternatively, lateral conductivity of the top layer may be improved by using the above-mentioned transparent conductive oxide (TCO) layer which, however, increases the overall cost of the cell as well as the optical absorption especially in the blue. Theoretically, the adoption of higher optical band-gap materials such as Zinc Sulfide (ZnS) may overcome the parasitic absorption limitations. In [132], Liu et al. proposed a comprehensive theoretical analysis and design on heterojunction structures by replacing a-Si:H thin films with opportune semiconductor materials. In particular, the suitable compounds investigated are Aluminum arsenide (AlAs) for the p-doped layer, and Gallium phosphide (GaP), Zinc sulfide (ZnS) for the n-doped layer. However, in literature the fabrication of highly doped samples of ZnS while maintaining acceptable conductivity, optical transparency and good c-Si surface passivation, has still to be demonstrated.

Poly-Si front and rear passivating contacts complemented by a TCO to provide sufficient lateral conductivity have been recently proposed [127] (Fig. 5.1(a)). For the sake of simplicity, in this work we name such a solar cell poly-Si top/rear contacts. In [127], a p-type c-Si substrate was investigated. Since no front texturing was used, short circuit current density (J_{SC}) is limited to approximately 33 mA/cm^2 and efficiency to 19%. The authors conclude that, although the realization of a poly-Si/SiO$_x$ contact for both solar cell sides (Fig. 5.1(a)) enhances V_{OC}, the parasitic absorption and the resistivity of the poly-Si at the front are relevant factors,

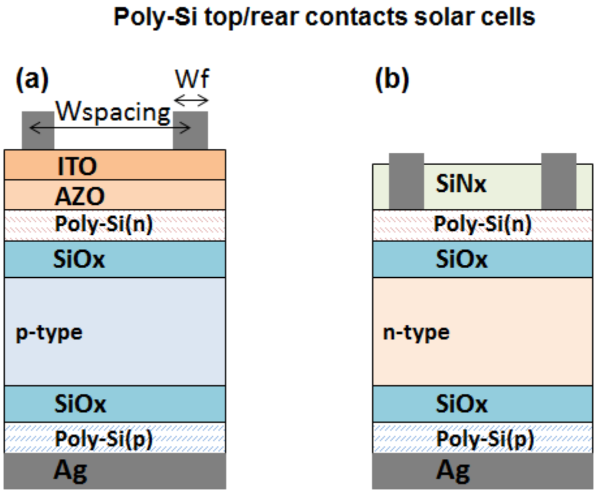

Figure 5.1: Sketches of the solar cell designs considered in this section. In (a), the scheme of the fabricated p-type poly-Si top/rear contacts solar cell [127] is shown. In (b) the n-type solar cell (rear junction design RJ) with a passivation SiN$_x$ layer instead of the ITO/AZO stack electrode is illustrated.

affecting J_{SC} and FF.

In this study, by means of a simulation flow, considering as starting point the architecture presented in [127] substantial modifications in order to overcome its limitations are proposed. Physical models calibrated by means of measurement performed on the poly-Si top/rear contacts solar cells fabricated at Fraunhofer ISE are adopted.

Firstly, following [43], a textured front surface is accounted for and the impact of front TCO presence and of front contact grid geometry on solar cell figures of merit (FOMs) is investigated.

Secondly, a rear junction (RJ) design of the poly-Si top/rear contacts solar cell featuring a Front Surface Field (FSF) implemented by adopting an n-type c-Si substrate is analyzed (Fig. 5.1(b)). Such a structure leads to improved efficiency compared to the p-type poly-Si top/rear contacts front junction (FJ) solar cell counterpart. As a matter of fact, in the n-type substrate solar cell the lateral carrier transport occurs mainly in the substrate and not in the top poly-Si layer, mitigating the impact of poly-Si resistivity on the FF.

In order to obtain better efficient tunneling effect thanks to a stronger band bending in c-Si and thus lower contact resistivity, a higher doping value concentration of the front poly-Si layer is required. In [127] it has been observed a lower passivation quality at the p-type poly-Si/SiO$_x$ interface respect to n-type interface as well as a lower measured peak doping concentration for Boron profiles. This is consistent with the lower Boron solubility with respect to the Phosphorus one, although several research groups achieved similar contact resistivity [130], [131], [133] with heavily doped Boron poly-Si layers comparable to that obtainable by using Phosphorus [128], [134], [135], [136]. The physical parameters in this simulation study are calibrated on the basis of experimental conditions of [127], in which only phosphorus-doped poly-Si as front layer material is considered.

According to simulations, efficiency above 23% is possible with poly-Si top/rear contacts solar cells implementing RJ design, even without TCO. In addition, the sensitivity of FOMs on front poly-Si thickness and doping concentration is studied. Finally, the impact of c-Si/SiO$_x$ interfaces defectiveness and of the effective tunneling masses is investigated for the RJ design of the poly-Si top/rear contacts solar cell, by means of numerical simulations.

5.2 Studied devices and simulation methodology

5.2.1 Studied devices

The p-type 2 cm x 2 cm planar poly-Si top/rear contacts solar cell fabricated and experimentally characterized at Fraunhofer ISE [127], features poly-Si contacts at both front and rear side (Fig. 5.1(a)). The absorber is a 250 μm-thick p-type 1 Ωcm FZ Si wafer, and poly-Si(n)/poly-Si(p) contacts are present at the front- and rear-side, respectively. The SiO$_x$ layer is $\approx$1.5 nm-thick. Such an experimental value has been chosen in according with previously cited studies [72], [74], [75]. The oxide layer has to allow for an efficient transport of the contact's majority carriers from the absorber into the doped Si layer. Therefore, its thickness has to be limited (<20 $\mathring{A}$) in order to guarantee an efficient tunneling mechanism (as assumed in this study) while the pinhole formation is supposed to play a minor role (not considered in this work).

Both poly-Si layers are 15-nm thick with constant doping concentrations, provided by ECV measurements [127], of $4{\cdot}10^{19}$ cm^{-3} for the poly-Si(n) and of $2{\cdot}10^{19}$ cm^{-3} for the poly-Si(p). Since the adopted thin poly-Si film exhibits a significant sheet resistance, in the order of 1000 Ω/sq, the deposition of a TCO on the front is required. More in detail, the front stack consists of a 20 nm-thick atomic layer-deposited Al-doped zinc oxide (AZO) interlayer and 55 nm sputtered indium tin oxide (ITO), reducing the sheet resistance down to 125 Ω/sq and avoiding sputter damage of the passivating contact.

The front grid includes 60 μm-wide and 2.5 μm-thick fingers with 800 μm spacing, realized by thermal evaporation of Ti/Pd/Ag and lift-off; the fully metalized rear side is coated by thermally evaporated Ag. Fig. 5.1(b) shows an additional structure that is analyzed in this study by means of numerical simulations, the n-type poly-Si top/rear contacts solar cell (RJ design). In such case, a FSF structure is obtained thanks to an n-doped poly-Si layer. In the sketch of Fig. 5.1(b), the emitter metal contacts directly the poly-Si and the front interface is coated by a $\mathrm{SiN_x}$ layer.

Realistic contact resistivity (ρ_C) values have been chosen for the mentioned structures. For the metal/ITO interface, it has been assumed a realistic ρ_C of 0.1 mΩcm^2 for evaporated contact, even higher than the value reported in [10]. Regarding the metal/poly-Si interface, a value of 1 mΩcm^2 is adopted, of the same order of magnitude of that reported in [10] for metal/semiconductor interface.

5.2.2 Simulation methodology and validation

The optical and electrical simulations reported in this section were performed by using Sentaurus Device [54], allowing the modeling of the carrier-selective contacts as already successfully performed in [72].

In the case of solar cells featuring planar front interface, the spatially resolved 1-D profile of the photo-generated electron–hole pairs within the silicon obtained from the optical simulation is mapped onto the 2-D electrical mesh grid.

The optical simulations have been performed by means of a standard raytracer in combination with the transfer matrix method (TMM) boundary conditions [54]. The optical properties of the ITO/AZO stack, as well as of the poly-Si layers, are experimentally measured. In order to model the typical roughness observed in the presence of the considered back interface stack (c-Si/$\mathrm{SiO_x}$/poly-Si/Ag), a Phong diffusive boundary condition [63] has been adopted, as already successfully performed in [78], [50], [137], The standard reference spectrum ASTM AM1.5G has been considered. Free carrier absorption (FCA) effect [62] within the poly-Si layers has been properly accounted for into numerical simulations as a function of the doping concentration following [16]. FCA can also affect the ITO layer. The optical properties of the ITO fabricated by Fraunhofer ISE are comparable to those reported by Holman in [138] for carrier density concentrations from 10^{19} to 10^{20} cm^{-3}. The absorption coefficients of such cases show a negligible FCA effect within ITO layer. In addition, as demonstrated by simulations, although a single layer of ITO (75 nm) represents the state-of-the-art as TCO [10], the adopted double stack ITO/AZO does not introduce significant optical performance variations.

Regarding the electrical part, an analytical 0.1-μm deep Gaussian profile (peak doping $1\cdot10^{19}$ cm^{-3}) adequately reproduces the doping tail of the poly-Si diffusions into the c-Si substrate, accordingly to the measured Phosphorus and Boron doping concentration profiles reported in [127]. The Surface Recombination Velocity (SRV) value at both c-Si/$\mathrm{SiO_x}$ interfaces has been calibrated in order to fit the experimental saturation current densities (J_0) value reported in [127]: $\approx$5 fA/cm^2 and $\approx$25 fA/cm^2 for the front and back interface, respectively. The adopted SRV are of 800 cm/s and $2.5\cdot10^3$ cm/s for the front and back interface, respectively. The doping-concentration dependent carrier mobility for the Phosphorus and Boron doped poly-Si films are modeled according to experimental values measured by Fraunhofer ISE. Fig. 5.2

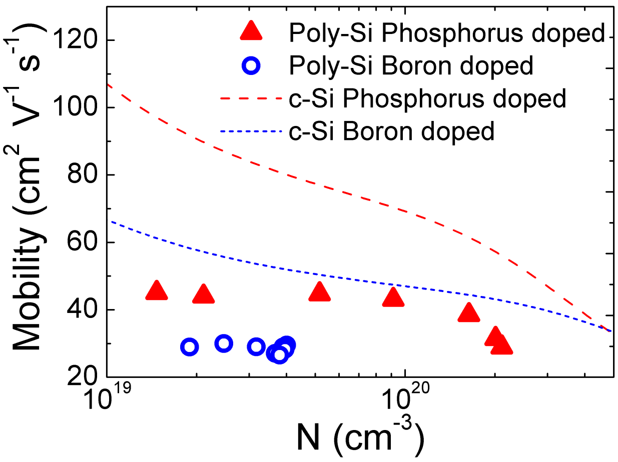

Figure 5.2: Measured majority-carrier mobility values of the poly-Si layer as a function of the doping concentration N. Red-filled triangles and blue-open circles refer to Phosphorus-doped and Boron-doped poly-Si, respectively. The carrier mobility values of c-Si (red dashed-line: Phosphorus-doped; blue short dashed line: Boron-doped) are reported as references.

reports such measured values and also carrier mobility values of c-Si for comparison. It is worth reporting that the poly-Si/SiO$_x$ contacts of interests were realized by LPCVD (low-pressure chemical vapor deposited) of a-Si layers, doping using ion implantation (Boron or Phosphorus) and subsequent annealing (900 °C, 10 min), as treated in [127]. The measured majority carrier mobility of Phosphorus-doped poly-Si deposited at Fraunhofer ISE plotted in Fig. 5.2 (grain size in the range from 100 to 400 nm for P-doped poly-Si) are comparable to those reported in literature [139], [140], for a grain size of 122 nm. Better poly-Si quality factor (i.e. larger grain size) may result in higher majority carrier mobility (50 – 80 cm^2/V/s) [141], [142].

The electro-optical device simulations adopt up-to-date physical and electrical models (including doping and carrier density dependence of mobility, band-gap narrowing) reported in [10] and successfully used in other simulation studies [72], [78], [50], [137]. Regarding the Auger recombination, the parameterization proposed by Richter et al. [143] is adopted. High-quality substrates are considered in order to highlight the effects of the investigated designs. In detail, in the proposed simulations, a Shockley Read Hall (SRH) minority carrier lifetime of 7 ms and of 4 ms has been adopted for n-type and p-type, respectively.

The current flow through the tunnel oxide layers is modelled by using the nonlocal tunneling model similar to [72], not considering the case of mechanism governed by pinholes formation discussed in [77]. For electrons (holes) an effective tunneling mass $m_{t,e}$ ($m_{t,h}$) of 0.4 m_0 (0.3 m_0) - m_0 electron rest mass - allows us to correctly fit the measured I-V characteristic and FOMs of the cell. The simulation models have been successfully validated by a comparison with experimental data as reported in

Fig. 5.3, showing an excellent agreement between simulated and measured optical properties of the FJ solar cell.

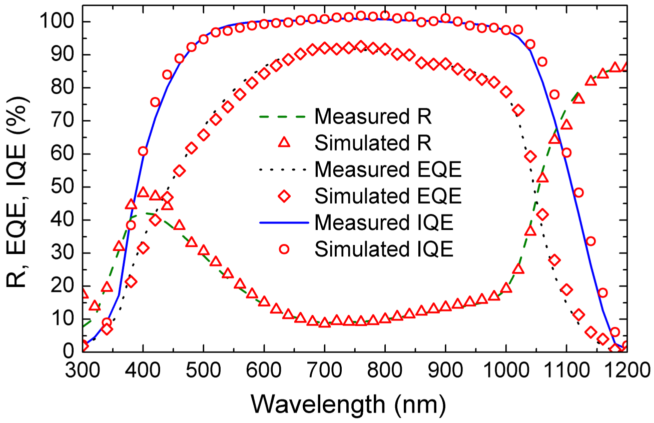

Figure 5.3: Simulation results (open-red symbols) of reflectance R (triangles), external quantum efficiency EQE (diamonds) and internal quantum efficiency IQE (circles) as a function of the wavelength of the solar cell fabricated at Fraunhofer ISE. Lines refer to measured results [127].

5.2.3 Modeling of the textured selective-contact solar cell

For all the studied structures of this section (Fig. 5.1) a textured front surface is assumed to remove the main limitation to low J_{SC}. To model the textured morphology, the spatially resolved optical generation rate was calculated starting from a 3-D symmetry element representing a regular upright pyramid featuring an opening angle of 70.5°. Tunnel SiO_x layer is assumed to be conformal to the textured interface with uniform thickness throughout the structure. Non uniformities of dielectric layer have been extensively studied in [77]. The textured solar cell is modelled in an effective way by simulating a 2-D planar solar cell instead of a more computationally demanding structure reproducing the pyramidal morphology. Specific tests showed that FOMs are hardly affected by such an approximation. In order to account in an effective way for the surface area enlargement due to texturing, an enhancement factor of 1.73 [10] is used for the SRV at the front c-Si/SiO_x interface.

In Table 5.1, the measured and simulated FOMs and poly-Si(n) saturation current density $J_{0,\text{Poly-Si(n)}}$ for the textured case compared to the planar one are reported. It can be noticed that texturing leads to higher J_{SC} respect to the planar case. This is ascribed to a lower reflectance obtained through overall the spectrum. However, due to the increased surface recombination, the $J_{0,\text{Poly-Si(n)}}$ increases of $\approx$5 fA/cm^2 for the textured solar cell. Therefore, the expected gain in terms of V_{OC} thanks to the elevated J_{SC} is almost entirely compensated due to higher $J_{0,\text{Poly-Si(n)}}$.

Table 5.1: p-type poly-Si top/rear contacts solar cell: measured [127] and simulated results

Front surface	J_{SC} (mA/cm^2)	V_{OC} (mV)	FF ($\%$)	Eff. ($\%$)	$J_{0,\text{poly-Si(n)}}$ (fA/cm^2)
with TCO*					
Measured [127]					
Planar	33.4	707.0	81.5	19.2	5
Simulated					
Planar**	33.4	706.0	81.5	19.2	6
Textured	37.4	706.8	81.4	21.5	11

** TCO electrode composed by 55nm of ITO and 20 nm of AZO*

*** Simulation of the structure experimentally characterized [127]*

5.2.4 Results and discussion

5.2.4.1 p-type substrate: Front Junction (FJ) design

Numerical simulations were used to investigate the impact on the FOMs of the presence of ITO/AZO stack (TCO). Moreover, in some cases the TCO is replaced for SiN_x layer and the metal fingers directly contact the poly-Si. In such cases, the adopted SiN_x layer thickness has been determined in order to maximize the photon current absorbed in substrate.

First, a study of the solar cells FOMs sensitivity on t_{poly} and on finger spacing ($W_{spacing}$) is carried out. In particular, t_{poly} has been assumed within the 15 nm - 60 nm range while $W_{spacing}$ from 800 μm to 1800 μm. Outside these ranges, a dramatic degradation of J_{SC} and of FF occurs. Two different realistic poly-Si(n) Phosphorus doping concentration (N_{poly}) values have been considered: $4{\cdot}10^{19}$ cm^{-3} and $2.7{\cdot}10^{20}$ cm^{-3} [127], [16]. In addition, for all the discussed structures, the poly-Si(p) at the back is 15 nm-thick and its Boron doping concentration is $2{\cdot}10^{19}$ cm^{-3}. The SRV values at c-Si/SiO_x interfaces allowing the fitting of the experimental results (t_{poly} = 15 nm) are assumed constant for the t_{poly}-range considered in this study (15 to 60 nm). In fact, from [127] it has been concluded that although a slight influence of t_{poly} on implied-V_{OC} (iV_{OC}) was observed (for t_{poly} from 6 nm to 34 nm), J_0 depends on t_{poly} only in the range of 5-10 nm. Moreover, recent data published in [16], show that the iV_{OC} (i.e. saturation current density J_0) is not affected by t_{poly} up to 145 nm. In this study, in absence of a clear understanding of relationship between c-Si/SiO_x interface quality and poly-Si thickness, constant SRV (section 5.2.2) is assumed.

In Fig. 5.4, the calculated J_{SC} and V_{OC} values are shown as a function of t_{poly}. The p-type FJ solar cell with TCO represents the baseline case. More in detail, Fig. 5.4(a) and Fig. 5.4(b) report the simulation results for N_{poly} set to $4{\cdot}10^{19}$ cm^{-3}, while Fig. 5.4(c) and Fig. 5.4(d) correspond to $N_{poly} = 2.7{\cdot}10^{20}$ cm^{-3}. From

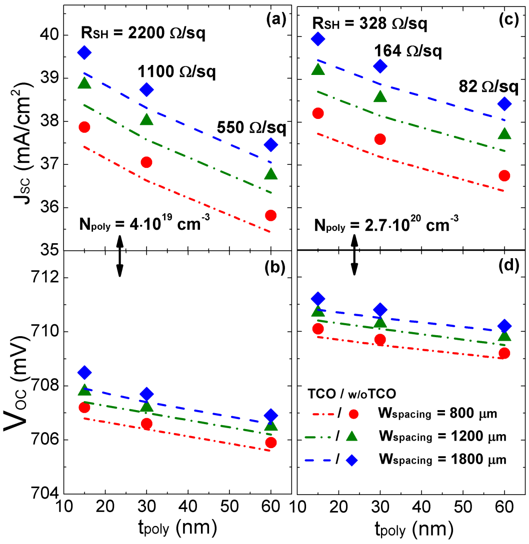

Figure 5.4: Simulated short circuit current density J_{SC}, (a) and (c), and open circuit voltage V_{OC}, (b) and (d), as a function of the front poly-Si thickness t_{poly}. (a) and (b) refer to a poly-Si doping concentration N_{poly} of $4{\cdot}10^{19}$ cm^{-3} while (c) and (d) to a N_{poly} of $2.7{\cdot}10^{20}$ cm^{-3}. Lines denote the cases implementing the TCO electrode whereas symbols refer to absence of TCO (w/oTCO). The colors blue, red and green refer to a finger spacing Wspacing of 800 μm, 1200 μm and 1800 μm, respectively. For each t_{poly}, in (a) and (c) the sheet resistance R_{SH} value expressed in Ω/sq is reported.

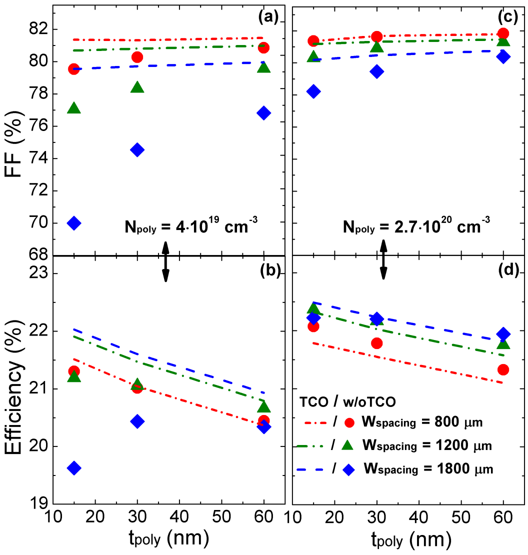

Figure 5.5: Simulated fill factor FF, (a) and (c), and efficiency, (b) and (d), as a function of the front poly-Si thickness t_{poly}. (a) and (b) refer to a poly-Si doping concentration N_{poly} of $4{\cdot}10^{19}$ cm^{-3} while (c) and (d) to a N_{poly} of $2.7{\cdot}10^{20}$ cm^{-3}. Lines denote the cases implementing the TCO electrode whereas symbols refer to absence of TCO (w/oTCO). The colors blue, red and green refer to a finger spacing Wspacing of 800 μm, 1200 μm and 1800 μm, respectively.

Fig. 5.4 it can be observed that the TCO stack leads to degradation of J_{SC} and V_{OC} due to significant parasitic absorption. In fact, our calculations show that the parasitic absorption loss of the front contact stack (TCO and poly-Si(n) layers) for the TCO case is close to 1.2 mA/cm^2 for t_{poly} = 15 nm, reducing to 0.9 mA/cm^2 as the TCO is omitted. Increasing N_{poly} leads to a better high-low junction [144], resulting in lower recombination at the front interface. Therefore, V_{OC} and J_{SC} slightly increase with the doping despite higher FCA effect. As expected, larger finger distance decreases the front contact metal shading leading to higher J_{SC} (Fig. 5.4). Fig. 5.5 shows the simulated FF and efficiency values. It is clearly noticeable that the adoption of a high doping level allows for acceptable FF values (> 77%) even without TCO; comparable FF-values can be obtained when TCO is present (Fig. 5.5(c)), for poly-Si thickness above 30 nm. In all other cases, in general avoiding TCO is dramatically detrimental to FF, especially for low poly-Si doping concentration (N_{poly} = 4·10^{19} cm^{-3}) as illustrated in Fig. 5.5(a). Furthermore, $W_{spacing}$ is a relevant parameter affecting FF. When N_{poly} = 4·10^{19} cm^{-3} removing the TCO electrode leads to degraded FOMs values for if $W_{spacing}$ > 800 μm, mainly due to significant FF losses.

The presented study demonstrates that for t_{poly} = 15 nm solar cells featuring TCO exhibit the highest conversion efficiency values. The simulated efficiencies without TCO are, in most cases, lower than the results with TCO, especially for thin poly layers. As soon as t_{poly} increases, the efficiency (Fig. 5.5(b) and (d)) declines due to parasitic absorption losses within the front stack. In summary, the solar cells with TCO show higher J_{SC} losses but small FF losses while a trade-off between the parasitic absorption losses and FF degradation exists for solar cells without TCO.

5.2.4.2 n-type substrate: Rear Junction (RJ) design

The lateral conductivity of the poly-Si(n) layer at the front side is one of the main reasons for the resistive losses observed in the studied FJ design of the poly-Si top/rear contacts solar cell especially when the poly-Si is highly resistive due to the limited carrier mobility (see Fig. 5.2). In this section, a scheme which avoids the previously discussed limitations is proposed, the RJ design which basically implements an n-type substrate instead of a p-type substrate, as depicted in Fig. 5.1(b). As demonstrated in [126] for SHJs, in a design in which the emitter is located at the rear side of the cell, the FSF allows for the reduction of the overall sheet resistance R_{SH} thanks to the coupling of the front poly-Si(n) and of the absorber (n-type). Thus, the current flow pattern towards the front electrode is differently distributed. Fig. 5.6, compares the current flow at the maximum power point of the p-type (FJ) and n-type (RJ) poly-Si top/rear contacts solar cells for $W_{spacing}$ = 800 μm. It can be clearly observed that in the RJ design a significant part of the transport occurs in the substrate, reducing the lateral transport contribution in the highly-resistive

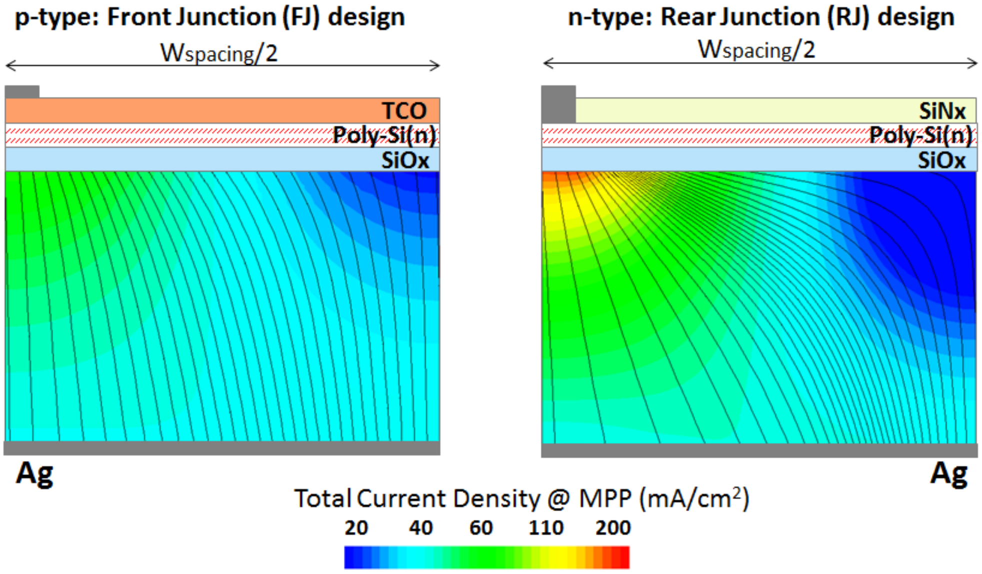

Figure 5.6: Simulated current paths (lines) and total current densities (color map) within the absorber at maximum power point condition (MPP). Left: p-type poly-Si top/rear contacts solar cell (front junction FJ design); right: n-type (rear juncion RJ design). The considered finger spacing $W_{spacing}$ is 800 μm and the plotted front stacks are not in scale.

front poly-Si. In the following, RJ solar cells are simulated by assuming the same set of physical models and a 15-nm thick poly-Si(n) as top electrode of the FJ solar cells (section 5.2.2). In Fig. 5.7(a) and Fig. 5.7(b) J_{SC} and $V_{OC}$are reported as a function of finger spacing. An N_{poly} impact for RJ solar cells comparable to the one of FJ (see Fig. 5.4) is noticeable. The most interesting findings are those observable from Fig. 5.7(c) and Fig. 5.7(d). In Fig. 5.7(c) the FF gain obtained thanks to the RE design concept is clearly noticeable. In particular, for $N_{poly} = 2.7{\cdot}10^{20}$ cm^{-3} the sensitivity to TCO presence is reduced. Promising efficiency values around 22.5% are obtained (see Fig. 5.7(d)). In contrast to the front emitter design, these values can be achieved with and without a TCO.

As stated in section 5.2.1, the adopted contact resistivity values have been realistically assumed following [10]. Since the quality of the contact formation is process-dependent, the impact of front-contact ρ_C on FOMs has been investigated. Simulation results (not shown) demonstrate that the impact of ρ_C on the solar cell FOMs is negligible for values < 10 mΩcm^2.

In this study, the considered range of majority carrier mobility as a function of the doping concentration in poly-Si is considerably small (Fig. 5.2). However, it is worth noting that a significant enlargement of the front poly-Si grain size could lead to higher majority carriers mobility value and thus resulting in a reduced efficiency enhancement of RJ scheme compared to FJ. Overall, higher poly-Si carrier mobility

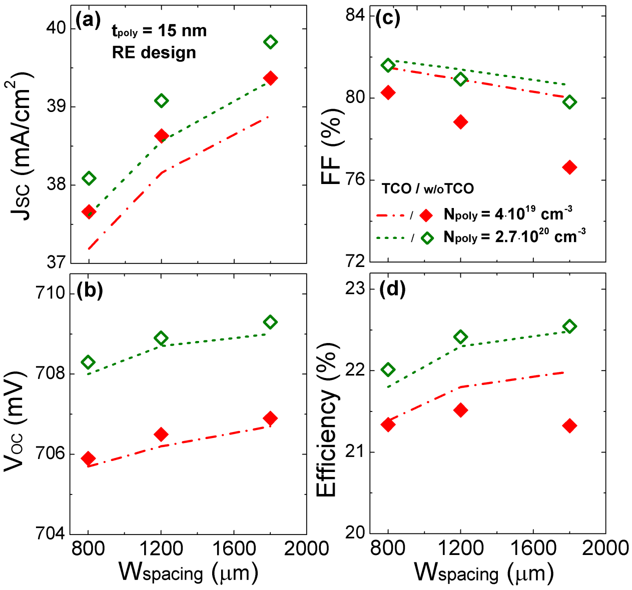

Figure 5.7: Simulated short circuit current density J_{SC} (a), open circuit voltage V_{OC} (b), fill factor FF (c) and efficiency (d) as a function of the finger spacing $W_{spacing}$ for n-type (RJ) design featuring front poly-Si thickness t_{poly} = 15 nm. Filled and open symbols refer to a poly-Si doping concentration N_{poly} of 4·10^{19} cm^{-3} (red) and 2.7·10^{20} cm^{-3} (green), respectively. Symbols and lines denote cases without TCO (w/o TCO) and with TCO, respectively.

leads to an increase in efficiency thanks to lower resistivity.

5.2.4.3 Rear junction design: sensitivity to interface passivation

Numerical simulations are performed in order to study the impact of defectiveness at the c-Si/SiO$_x$ interfaces on conversion efficiency. The discussion is limited to the RJ design, omitting TCO and assuming t_{poly} = 15 nm and N_{poly} = 2.7·10^{20} cm^{-3}.

For the previous analyses the SRV values at the c-Si/SiO$_x$ interfaces determined on the basis of experimental data have been considered. However, simulations show that efficiency can be potentially improved considering realistic values of SRVs. With respect to SRV at front interface, V_{OC} improvements are negligible (Fig. 5.8(a)). Hence, from measurements, front interface exhibits good passivation [127]. On the contrary, concerning the back SRV, a significant increase in V_{OC} can be potentially attained. Assuming a better quality passivation of poly-Si/c-Si interfaces, conversion efficiency of 23.5% may be achieved.

5.2.4.4 Influence of effective tunneling mass m_t

In previous sections, a value of electron (hole) tunneling effective mass $m_{t,e}$ ($m_{t,h}$) that successfully fits available experiments is adopted. The analysis proposed in

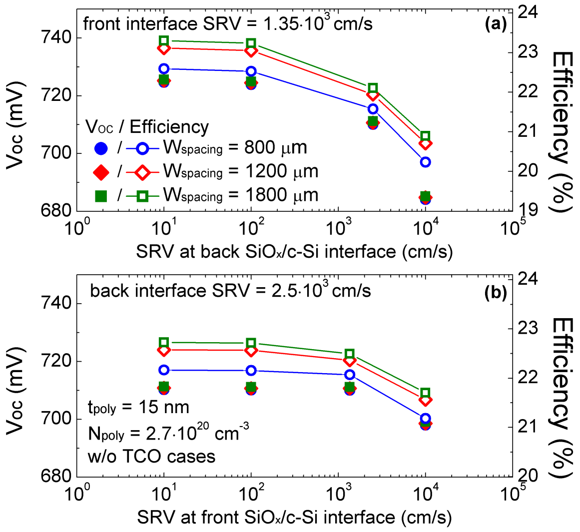

Figure 5.8: (Simulated open circuit voltage V_{OC} (filled symbols) and efficiency (open symbols) for the n-type poly-Si top/rear contacts solar cell (RJ design) featuring poly-Si thickness t_{poly} = 15 nm and doping concentration $N_{poly} = 2.7 \cdot 10^{20}$ cm^{-3}. In (a) and in (b) the values are plotted as a function of the back SRV and front SRV, respectively. The colors blue, red and green refer to a finger spacing $W_{spacing}$ of 800 μm, 1200 μm and 1800 μm, respectively.

this paragraph is aimed at exploring how the accuracy of such a fitting parameter influences the simulation results. In this regard, the sensitivity of the calculated solar cell figures of merit on $m_{t,e}$ and on $m_{t,h}$ is studied by means of numerical simulations.

Fig. 5.9(a) shows the impact of $m_{t,e}$ on the FF for both p-type (FJ) and n-type (RJ) poly-Si top/rear contacts solar cells (t_{poly} = 15 nm, $N_{poly} = 2.7 \cdot 10^{20}$ cm^{-3}, TCO omitted, $m_{t,h}$ fixed at 0.3 m_0). It can be observed that both the FJ and RJ scheme takes advantage of smaller $m_{t,e}$ thanks to a higher tunneling probability. In detail, resistive losses are reduced in RJ solar cell because, as previously discussed, a relevant part of the transport occurs in the substrate instead of within the highly resistive front poly-Si layer (Fig. 5.6). On the contrary, a less effective tunneling mechanism ($m_{t,e} > 0.4$ m_0) decreases the difference in terms of FF between the two designs and the benefit introduced by RJ design are reduced. RJ design results more sensitive to the tunneling mechanism, due to its current transport path. However, if we consider a realistic $m_{t,e}$ range (0.37 – 0.43 m_0) RJ exhibits higher FF with respect to FE scheme.

The observed influence of $m_{t,e}$ can be compared with that reported in [72] for a solar cell featuring TOPCon. By exploring the same $m_{t,e}$ range (from 0.3 m_0 to 0.45 m_0) it can be concluded that the sensitivity to such parameter is comparable (≈0.6%$_{abs}$ of FF for FJ design). Moreover, it is worth reporting that in [72] the passivated contact (electrons as majority carriers) concept has been applied to a

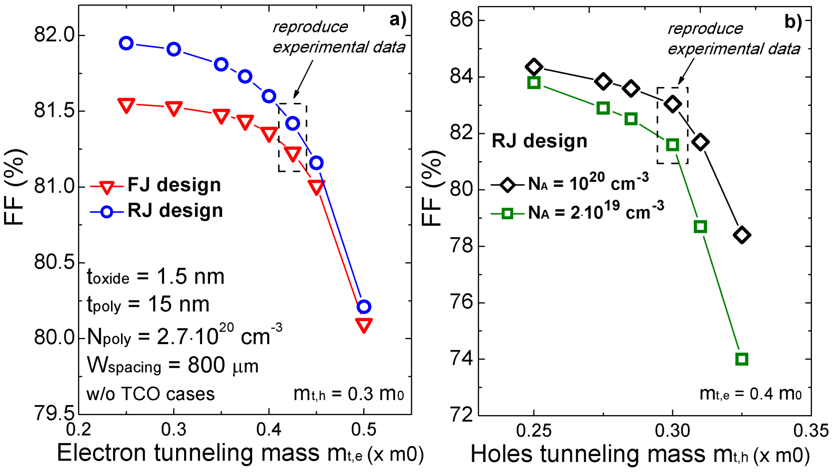

Figure 5.9: Simulated FF against the effective electron tunneling mass $m_{t,e}$ (a) and the effective holes tunneling mass $m_{t,h}$ (b). In (a), red triangles and blue circles refer to p-type (FJ) and n-type (RJ) poly-Si top/rear contacts solar cell, respectively. In (b), black diamonds and green squares indicate a Boron doping concentration N_A for the poly-Si layer at the back side of $1{\cdot}10^{20}$ cm^{-3} and of $2{\cdot}10^{19}$ cm^{-3}, respectively. In (a) $m_{t,h} = 0.3\ m_0$ while in (b) $m_{t,e} = 0.4\ m_0$.

full-metalized back contact whereas in this work to a front contact.

The influence of $m_{t,h}$ concerns the tunneling mechanism at the full back-contacted side of the studied cells. Simulation results of Fig. 5.9(b) ($m_{t,e}$ fixed at 0.4 m_0) demonstrate that the RJ design is more sensitive to $m_{t,h}$ than to $m_{t,e}$ (shown in Fig. 5.9(a)). In fact, for a relatively low Boron doping value concentration (N_A) of the poly-Si(p) back layer, the tunneling mechanism is mainly governed by the assumed $m_{t,h}$ value. On the contrary, a higher (N_A) leads to increased FF and to a less sensitivity to $m_{t,h}$. In addition, it can be observed a higher V_{OC} thanks to a better high-low junction effect. More in detail, for $m_{t,h}$ reproducing experimental data (0.3 m_0), an efficiency increasing of $\approx$0.55%$_{abs}$ results by considering N_A of $1{\cdot}10^{20}$ cm^{-3}.

5.3 Conclusions

In this chapter, a calibrated numerical simulation flow able to successfully model the solar cell fabricated by the Fraunhofer ISE featuring poly-Si/SiO$_x$ carrier-selective contact on both sides is presented. This study addressed the solar cell design to a scheme avoiding the TCO which leads to increase in manufacturing cost and process complexity. In the case of a front junction (FJ) design of the solar cell with poly-Si top/rear contacts, it has observed that, although J_{SC} and V_{OC} benefit from the absence of TCO, FF is critically influenced by front electrode conductivity. FF degradation can be mitigated by increasing either the poly-Si layers thickness or doping concentration, but TCO is suggested to attain acceptable efficiency. Increased doping concentration in poly-Si may result both in a better high-low junction and in a decrease in resistive losses. To overcome the typical limitations of a FJ design, a rear junction (RJ) scheme is proposed. The presence of a front surface field reduces the lateral transport in the front poly-Si layer, therefore, in case of sufficiently doped poly-Si, the RJ design is more insensitive to TCO properties with respect to the FJ design. This enables higher conversion efficiency combining the lower costs of an industrial type solar cell based on carrier-selective contacts. As shown by simulations, conversion efficiency above 23% is obtainable without considering further improvements deriving from using fine-line metallization technology as well as smart wire interconnection. Finally, it has been observed that the influence of the effective electron tunneling masses used for simulations is limited if a range of 0.37 – 0.43 m_0 is considered, while the holes tunneling mechanism is strictly dependent on the poly-Si(p) doping concentration.

Chapter 6

Simulation studies of advanced options for silicon Solar Cells

In this chapter, three comprehensive simulation studies investigating advanced options applicable in standard high efficiency c-Si solar cells are presented. Section 6.1 reports an analysis of the impact of a rear point contact (RPC) scheme in metal wrap through (MWT) solar cells with passivated base by means of numerical simulations. The discussed results have been published in Journal of Computational Electronics by the author of this thesis [145]. In the section 6.2, a numerical simulation is set up in order to reproduce the experimental measured values of figures of merit (FOMs) of four different PERC solar cells lots subjected to a degradation and two regeneration processes by modeling the recombination centres in bulk and the Boron-Oxygen complexes (B-O). This study refers to the work [146], published in Energy Procedia. In the last part of this chapter (section 6.3), which has been published in Energy Procedia [147], the results of electro-optical simulations of multi-wire solar cells aimed at calculating the effective optical shading factor, the enhancement of conversion efficiency and the saving of contact-paste, with respect to the busbar design are presented. The activities discussed in this chapter were developed in close collaboration with Applied Materials Italia s.r.l (AMAT) who provided the experimental characterization results of the considered solar cells.

6.1 Theoretical study of the impact of rear interface passivation on MWT silicon solar cells

As stated in the first chapter of this thesis, crystalline silicon (c-Si) solar cells are still extremely interesting and attractive for the photovoltaic (PV) industry. Research in PV is aimed at lowering the cost-per-watt ratio. This challenging goal can be achieved either by reducing the volume of the absorbing material and by improving solar cell efficiency. Among the promising solar cells architectures, metal wrap through (MWT) ([25], [148]) have been demonstrated to reach efficiency up to 20% [23], [20]. The main advantage of MWT solar cells is that the reduction of front metallization leads to an increase of photogenerated current density thanks to reduced shading [25], [24], [95]. In that case, the presence of a metallic via ensures the current transport from front fingers to bottom busbars. Moreover, another advantage of MWT solar cells is that their fabrication process can be exploited with few modifications with respect to conventional front contact (FC) solar cells [23]. However, also in case of MWT solar cells, one of the most relevant limiting mechanism for conversion efficiency is represented by recombination losses [26]. In particular, as discussed in this chapter, the most significant contribution to the total saturation current density is that from the base (mainly due to losses in back surface field region and at base metal contact). This contribution potentially represents up to 55% of the total recombination losses. In addition, by reducing the material volume (i.e. lowering substrate thickness) the relative impact of the base on the total recombination current may even increase. Therefore, in order to enhance the efficiency, an effective way is the adoption of a rear point contact (RPC) option in base [111], [149], [150], [151], [152], [153], [154], [155]. This opens the way to base passivation while the contact is ensured by openings in the c-Si/dielectric stack [156], [157], [158]. In addition, RPC is advantageous in terms of light absorption thanks to a relative higher internal reflectivity of the c-Si/dielectric/Aluminum stack at the back side of the cell, in comparison with the Aluminum back surface field interface [149]. However, a significant drawback of RPC schemes is the increase of the series resistance such as the lateral base resistance caused by the current flow pattern [159] of the majority carriers and the base contact contribution due to the reduced contact area [149]. Therefore, a theoretical study aimed at calculating the optimum contact fraction (C_{fr}) by accounting for all competing physical mechanisms occurring in a RPC structure may be helpful to provide guidelines for the fabrication of MWT cells. MWT cells have been investigated by means of numerical simulations and analytical models in [20], [160], [161]. Conversion efficiency values of 20.6% for float-zone and 20.1% for Czochralski-grown silicon have been achieved on large-area cells in [162], [163] and in [164]. A systematical optimization of the metallization layout of MWT-RPC solar cells has been carried out by using analytical models by Hendrichs [24] to demonstrate efficiency above 20%. Moreover, in [20] a potential efficiency $> 21\%$ has been estimated for fully deactivated boron-oxygen related recombination. This work is about the simulation of MWT cells featuring a rear point contact scheme in base (MWT-RPC). Starting from the considerations of Thaidigsmann [20], on the efficiency potential of the MWT-PERC scheme and a detailed loss analysis, a specific study about the impact of geometrical and doping parameters on main FOMs and on recombination losses is performed. For this study a state-

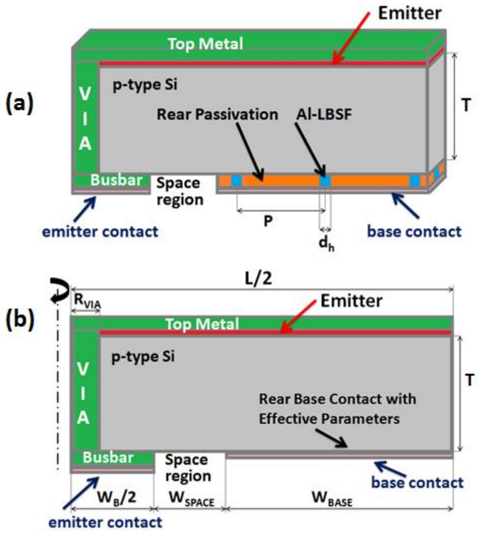

Figure 6.1: (a) Schematic of 3-D MWT-RPC solar cell with aluminum local back surface field (Al-LBSF) and and (b) cross-section of simulated MWT with effective parameters featuring rotational symmetry with respect to the via axis. The light-blue spots represent the opening in base with the respective Al-LBSF. L denotes the via spacing, T is the wafer thickness, W_B indicates the rear busbar width, W_{SPACE} is the space region width, W_{BASE} is the base contact width, P is the hole pitch and d_h represents the hole diameter. The schematics are not in scale as well as the point contact scheme in base (Color figure online)

of-the-art finite-element TCAD simulator [53] is adopted. The presented numerical simulation methodology significantly reduces the computational effort required for the simulation of the whole true three-dimensional spatial simulation domain.

This section is organized as follows: in subsection 6.1.1 the numerical simulation methodology, describing the studied solar cells and the adopted physical models are outlined. In subsection 6.1.2 the results of the analyses of the impact of the main geometrical and doping parameters of the MWT-RPC solar cell are discussed. Lastly, in subsection 6.1.3, the main results of the study are summarized.

6.1.1 Simulated device and simulation methodology

The studied device (Fig. 6.1.1(a)) is a MWT solar cell with passivated base (MWT-RPC). The contact in base is ensured by circular openings arranged in square lattice through which the Aluminum is screen printed to form the aluminum-local BSF (Al-LBSF). Emitter and base contacts are in the bottom side of the cell (separated by a region called “space region”). A metallic via ensures the contact between front emitter grid and bottom busbars. Disregarding the passivated base, the device is similar to that studied in [26] and [109] (Fig. 6.1.1(b)). The simulation of the full 3-D MWT-RPC cell (Fig. 6.2(a)) requires significant computational resources.

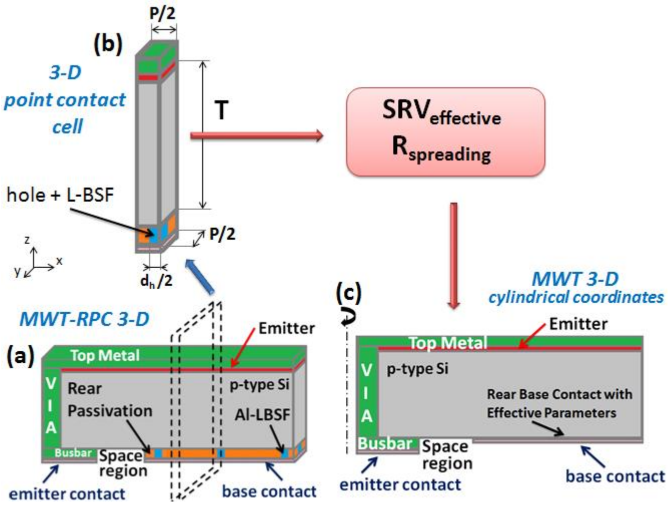

Figure 6.2: Schematic of the simulation flow adopted in this work. From the 3-D MWT-RPC structure (a), we extract a 3-D domain that represents the solar cell with point contacted base (b), which is used to calibrate the analytical models (Eqs. 6.2, 6.3) adopted for the calculation of the spreading resistance contribution ($R_{spreading}$) as well as the effective surface recombination velocity in base (SRV_{eff}). The extracted parameters are then used to perform the simulation of MWT-RPC solar cell by exploiting rotational symmetry with respect to the via axis (c). T, P and d_h denote the wafer thickness, the hole pitch and the hole diameter, respectively.

For this reason, it has been adopted the following simulation methodology, which is based on two different steps. First, in order to study the effects of the RPC in terms of recombination losses and of resistive contributions, a simplified (not MWT) structure (including the emitter, the substrate and the RPC base) is simulated bymeans of a true 3-D TCAD simulation. The simulated structure features the same geometry and periodicity of the rear contact pattern as well as the same doping profile of the local BSF of the MWT-RPC solar cell. This structure does not include the via, therefore the simulation domain allows to perform numerical simulations requiring limited computational resources (Fig. 6.2). Thanks to this simulation, as discussed in detail in the following subsection, the proposed analytical models used to calculate the effective values of surface recombination velocity (SRV) and spreading resistance (SRV_{eff} and the $R_{spreading}$, (Fig. 6.2(b)) are calibrated. Then, a MWT-RPC solar cell is simulated accounting for rear point contacts and Al-LBSF by adopting the effective parameters SRV_{eff} and the $R_{spreading}$ previously calculated (Fig. 6.2(c)). Moreover, this simulation is performed by exploiting the axial symmetry (using the via centre as axis of rotation) of the structure by solving the semiconductor equations recast in cylindrical coordinates, over a 2-D section of the device [26]. This allows to extend the simulation to a 3-D domain with acceptable computational effort. The front surface of the simulated cell is entirely covered by a transparent electrode which is used to account for the FC grid. In detail, as boundary

Table 6.1: Default parameters of the simulated structures

Parameter	Value
Wafer width	15.6 cm x 15.6 cm
Number of vias	16
Via radius (R_{VIA})	100 μm
Space region width (W_{SPACE})	1 mm
Rear busbar width (W_B)	2 mm
Base contact width (W_{BASE})	2 cm
Number of fingers	80
Number of busbars	4
Metal resistivity	$2.36 \cdot 10^6$ Ωcm
Finger height	8 μm
Finger width	65 μm
Front busbar height	10.1 μm
Front busbar width	Min: 334 μm Max: 787 μm
SRV at metalized regions (SRV_{met})	$1 \cdot 10^6$ cm/s
SRV passivated emitter (SRV_{em})	$1.81 \cdot 10^5$ cm/s
SRV passivated base (SRV_{pass})	70 cm/s
Front grid resistance (R_{grid})	0.5483 Ωcm^2
Specific contact resistivity (ρ_c)	1 mΩcm

condition at the front interface we adopt an effective Surface Recombination Velocity (SRV_{em}) calculated as an area weighted average between the surface recombination velocity at the passivated interface and that at contacted regions. Furthermore, a series resistance representative of H-pattern grids with tapered busbars (R_{grid}) is considered [109]. In the remainder of this section, the adopted doping and the geometrical parameters into simulations and the numerical simulation flow used to calculate the effective parameters representing the RPC scheme are discussed. Lastly, the adopted electrical and physical models are illustrated and the optical simulation is outlined.

6.1.2 Simulated device: doping and geometrical parameters

The default electrical and geometrical parameters of the simulated device are summarized in Table 6.1. The emitter features a sheet resistance of 75 Ω/sq and a doping profile with kink-and-tail shape [165] and chemical surface concentration of $4 \cdot 10^{20}$ cm^{-3}. By adopting these assumptions simulations result an emitter saturation current density of approximately 200 fA/cm^2. The contributions at region and mechanism wise level to the total dark saturation current density are calculated as illustrated in [110], [137]. The 10 μm-deep Aluminum BSF doping profile is similar to that presented in [166]. The trap-assisted recombination accounting for Al-O complexes in the Al-LBSF region is modeled by using the Altermatt's parameterization [166] and comparable values of saturation current density have been calculated. In the case of FC solar cell, the same emitter sheet resistance and BSF profile, a finger metallization of 3.54% (85 fingers, 65 μm-wide) and three, 1.5 mm-wide, front busbars are assumed.

6.1.2.1 Calculation of the effective parameters of the RPC base

3-D numerical simulations are performed on a simplified structure representative of the solar cell exhibiting the RPC scheme only (Fig. 6.2(b)), aiming at calculating an effective surface recombination in base ($\mathrm{SRV_{eff}}$) and a series resistance ($\mathrm{R_{spreading}}$) accounting for the lateral current flow due to the RPC structure. The via and the space region of the MWT structure are not included in such simulation domain. The 3-D spatial domain includes both the front emitter and the Al-LBSF. Such simulation domain which includes a quarter of opening in base is half rear contact pitch wide and features the same cell thickness of the MWT-RPC structure (Fig. 6.2(b)). The effective parameters allow to accounting for the RPC scheme in combination with the local Al-LBSF by simply simulating a 1-D structure without BSF diffusion and featuring a uniformly contacted base. $\mathrm{SRV_{eff}}$ is calculated as the Surface Recombination Velocity value set as boundary condition at the back of the 1-D cell which allows to equate the total dark saturation current density of the 3-D simplified cell ($\mathrm{J_{0,back,3D}}$) and of the 1-D structure ($\mathrm{J_{0,back,1D}}$):

$$J_{0,back,3D} = J_{0,BSF,3D} + J_{0,met,3D} + J_{0,pass,3D} = J_{0,back,1D} \tag{6.1}$$

where $J_{0,BSF,3D}$, $J_{0,met,3D}$ and $J_{0,pass,3D}$ are the saturation current density of the BSF (including Auger, trap-assisted and radiative contributions), of the metalized base and of the passivated base for the 3-D simplified cell, respectively. In addition, the spreading resistance $R_{spreading}$ is calculated from the I–V characteristic. The values of SRV_{eff} and $R_{spreading}$ are then used to calibrate the semi-empirical models from literature [150], [153], [167], as a function of $\mathrm{C_{fr}}$ value and of other input parameters:

$$\begin{aligned} R_{spreading} = R_{s,back,dark} - R_{bulk} = a \cdot p^2 \cdot \frac{\rho_S}{2 \cdot \pi \cdot r} \cdot atan(\frac{2T}{r}) \\ +b \cdot \rho_S \cdot T\{1 - exp(\frac{-T}{p})\} - \rho_S \cdot T \end{aligned} \tag{6.2}$$

$$\begin{aligned} SRV_{eff} = exp(-c \cdot X) \cdot \frac{D_n}{T} \cdot (\frac{R_{s,back,dark}}{\rho_S \cdot T} + \frac{D_n}{d \cdot X \cdot T \cdot SRV_{met,*}} - h)^{-1} \\ + \frac{exp(-X) \cdot e \cdot SRV_{pass}}{1 - X} \end{aligned} \tag{6.3}$$

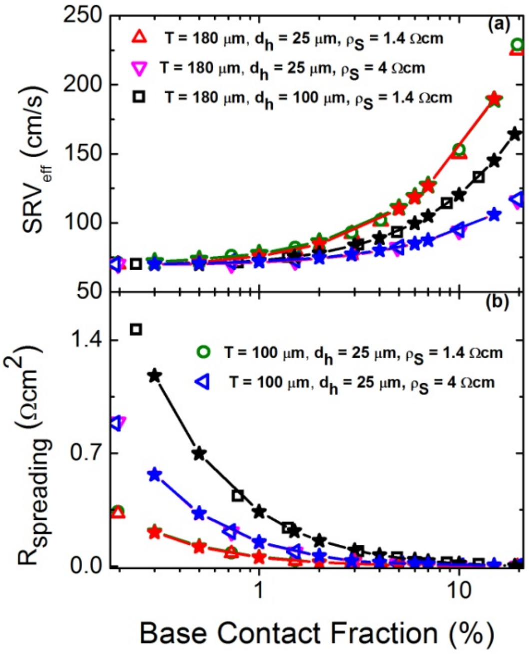

Figure 6.3: Effective surface recombination velocity SRV_{eff} (a) and spreading resistance R_h (b) calculated by 3-D TCAD simulations versus base contact fraction for MWT solar cells with RPC option, with substrate thickness T, hole diameter d_h and substrate resistivity ρ_S as parameters. Line-scattered star-points denote the values obtained by using analytical models (Eqs. 6.2, 6.3)

where ρ_S is the substrate resistivity, T is the substrate thickness, r is the hole radius, p is the hole pitch, $R_{s,back,dark}$ is the total dark series resistance of base, D_n is the electron diffusivity, $R_{bulk} = \rho_S \cdot T$ is the p-Si substrate resistance and $X = C_{fr}/100$. The fitting parameters a, b, c, d, e, h and $SRV_{met,*}$ are chosen on the basis of the geometrical and doping parameters and a comparison between numerical simulations and calibrated analytical models is reported in Fig. 6.3. Typically the calibration is carried out by using five values of SRV_{eff}, $R_{spreading}$ calculated by means of numerical simulation. Equations 6.2 and 6.3 have been modified with respect to those proposed in [167] in order to account for the presence of a LBSF in a RPC scheme. The presence of the LBSF leads to significant deviations in terms of SRV_{eff} and $R_{spreading}$ with respect to the original models especially at relatively higher base contact fraction and at lower C_{fr}, respectively. It is worth noting that for $C_{fr} = 100\%$, $R_{s,back,dark}$ is equal to the bulk resistance and SRV_{eff} is equal to SRV_{pass}; whereas for particularly low C_{fr}, SRV_{eff} is close to $SRV_{met,*}$. According to [167] it has been assumed with a reasonable approximation for the adopted cell thickness that the total series resistance of rear contact under illumination is equal to that under dark conditions. The calculated values of effective parameters are then used to account for the passivated base and the Al-LBSF in the complete MWT-RPC cell. The outlined methodology assumes that the presence of the space region, the bottom emitter and the via do not affect the calculation of the effective electrical parameters ($\mathrm{SRV_{eff}}$ and $\mathrm{R_{spreading}}$. All contributions to the total series resistance (including spreading resistance and contact resistance as well as the grid contribution) with the exception of the via resistance and the series resistance due to lateral conduction (since they are accounted for in the device simulation), are considered in a post-processing computation. The results obtained by simulations have been compared with [20] and [168], where a validation of the model by experimental results has been discussed, and we have observed the same trends considering the physical and geometrical substrate properties. The proposed methodology has been validated by comparing the results discussed in subsection 6.1.3 with those obtained by simulating a true 3-D MWT-RPC solar cell for two different substrate thicknesses (180 and 100 μm) and for significantly different values of coverage fraction in base (0.37 and 100%). In terms of agreement of the calculated FOMs (in particular $\mathrm{V_{OC}}$ and $\mathrm{J_{SC}}$) the comparison has resulted in a maximum relative error of 3% while in the case of FF and efficiency the absolute error has been observed to be less than 1%. Since the true 3-D MWT-RPC solar cell simulation accounts for the real geometry of the device, it is expected to provide a more accurate result compared to the simulation carried out by means the proposed methodology. As a matter of fact, it is observed that the true 3-D simulation is affected by lower numerical accuracy. This loss in numerical accuracy is ascribed to the poor mesh refinement especially in critical regions of the device such as the emitter and the base. In fact, the mesh has been designed in order to not exceed the computational resources capability of the used workstation (64 GB of RAM, 32 Intel Xeon cores).

6.1.2.2 Electrical and physical models

Numerical simulations are performed by using a TCAD device simulator [53] with parameters of physical models tuned for typical silicon PV technologies, as already successfully adopted in [26], [50], [107], [108], [149], [137], [169], [170], [171], [172], [173], [174]. They include the band-gap narrowing model by Schenk to account for the effective intrinsic carrier density [65], the Altermatt's parameterization for Auger recombination model [9], the mobility model proposed by Klaassen [70], [71] and the bulk Shockley–Read–Hall parameters for non-degraded boron doped Cz-Si according to Glunz's parameterization [114]. Fermi–Dirac statistics is accounted for in order to properly model highly doped regions. The parameterization proposed by Kimmerle [175] is adopted for the SRV at $\mathrm{SiN_x}$-passivated front surface.

6.1.2.3 Optical simulations base

Optical generation rate profiles are calculated by means of a ray tracing simulator in combination with a transfer matrix method [164]. A standard AM1.5G spectrum (1000 W/cm^2) [121] is assumed. Simulations account for front surfaces coated by SiN$_x$ textured by regular upright pyramids. The spatially resolved optical generation rate is calculated by considering two different kinds of stacks at the back interface (silicon/silicon-oxide/aluminum/air stack at passivated interface and silicon/aluminum/air at contacted interface). A Phong diffusive boundary conditions [63] is adopted to better model the roughness which is typically observed in such materials stacks [176]. The resulting optical generation rate profiles are averagely weighted depending upon the metallization fraction C$_{fr}$. For instance, for wafer thickness of 180 μm, the passivated interface leads to photo generated current density of 42.19 mA/cm^2 while the Al-LBSF interface leads to 41.46 mA/cm^2.Moreover, it is worth noting that the optical generation rate is properly scaled according to the front contact fraction (in this section 4.73%, representative of H-pattern grids with tapered busbar [26]).

6.1.3 Results and discussion

In this subsection, the analysis of the impact of substrate thickness, of resistivity and of hole size on the MWT-RPC cell saturation current density and on main FOMs are discussed. The contact fraction is changed by varying the value of the hole pitch. The above-mentioned parameters are potentially critical in RPC schemes. As a reference, we adopt the MWT cell without passivated base (full base contact, MWT non-RPC) and the conventional H-pattern, FC solar cell. In the following, the analysis is limited to the contact fraction range 0.3–20% within which the optimum value is typically found.

6.1.3.1 Impact of substrate thickness

The MWT-RPC solar cell has been simulated for two different substrate thickness values T: 180 μm (close to the current industrial standard for c-Si technology) and 100 μm (Thereiden and coauthors have demonstrated that 100 μm-thick silicon solar cells with efficiencies up to 20% are industrially feasible in a pilot production line [177]). The analysis has been carried out by adopting substrate resistivity of 1.4 Ωcm (base doping 10^{16} cm^{-3}). For the baseline MWT non-RPC it can be observed a more relevant contribution of the BSF region to the dark saturation current in the case of thinner substrate. In fact, in the case of the 180 μm-thick solar cell with ρ_S = 1.4 Ωcm, the relative contribution of the BSF region (399 fA/cm^2) to the total saturation current density (720 fA/cm^2) is 55% and for the 100 μm-thick is 60% (BSF region 447 fA/cm^2 and total saturation current density 738 fA/cm^2). This is mainly ascribed to the ratio carrier diffusion length to substrate thickness, which, in the case of thinner cell, explains the higher carrier recombination at the bottom interface. This effect partially compensates the decrease in saturation current in bulk due to the reduction of semiconductor volume. By reducing the contact fraction

C_{fr}, the J_{SC} increases (Fig. 6.4) due to (i) lower SRV_{eff} in base (Fig. 6.3) and to (ii) higher internal bottom reflectivity. The thicker substrate ensures enhanced photon absorption, which results overall in higher J_{sc}. Lower SRV_{eff} results in a decreased saturation current density (Fig. 6.5) and in a higher open-circuit voltage V_{OC} (Fig. 6.4). As discussed previously, by reducing C_{fr}, the impact of the spreading contribution ($R_{spreading}$) to the total series resistance becomes more relevant (Fig. 6.3 leading to a marked fill factor (FF) degradation (Fig. 6.6). No significant difference is observed in FF curves for the two considered different values of substrate thickness, meaning that such geometrical parameter within the considered range of values has a comparable impact on the lateral conduction of holes [26], [160]. For the spreading resistance contribution due to the RPC base scheme this can be also observed from Fig. 6.3. Both spreading series resistance and SRV_{eff} have similar values within the considered C_{fr}-range, independently of the base thickness. This results in a comparable optimum C_{fr} value (approximately 3%) for both thickness values. The substrate thickness has no significant effect on SRV_{eff} due to the relatively high value of electron diffusivity D_n. Moreover, for relatively thick substrates, T has no relevant impact on the lateral current flow of majority carriers. However, compared to the thicker cell, the 100 μm-thick MWT-RPC cell exhibits a more marked increase in efficiency with respect to the corresponding MWT without RPC option (not shown in Fig. 6.6). In fact, the simulation of the 100 μm-thick MWT solar cell without RPC option results in an efficiency of 18.86% exhibiting an increase of $1.31\%_{abs}$ in the case of MWT-RPC cell at the optimum C_{fr} (3%). For the 180 μm-thick the enhancement is equal to $1.07\%_{abs}$. Moreover, with respect to the FC solar cell [149] in the case of MWT-RPC (at the optimum C_{fr}) simulations show an increase in terms of efficiency of $1.33\%_{abs}$ for the thicker cell.

6.1.3.2 Impact of substrate resistivity

The analysis has been carried out by adopting substrate thickness 180 μm and two different resistivity values: $\rho_S = 1.4\ \Omega$cm and $\rho_S = 4\ \Omega$cm (bulk doping $3.5 \cdot 10^{15}$ cm^{-3}). ρ_S affects both the diffusion length of carriers (a doping concentration dependent carrier lifetimes is assumed) and the spreading resistance. From the simulations it is observed that, by increasing ρ_S the bulk saturation current density approximately halves in the case of the MWT non-RPC solar cell (from 90 to 47.5 fA/cm^2). However, similarly to the case of the substrate thickness discussed in the previous Subsection, this reduction is compensated by the increase in $J_{0,back}$. This motivates the study on the adoption of RPC schemes in MWT solar cells featuring highly resistive substrates in order to analyze the impact of such option on the base region. A lower J_{sc} in the case of the 1.4 Ωcm substrate is observed (Fig. 6.7); this is ascribed to the higher carrier recombination in the substrate that degrades the collection efficiency (not shown). Concerning the influence of C_{fr} on J_{SC} and V_{OC}, similar trends are observed in comparison with the analysis of the impact of

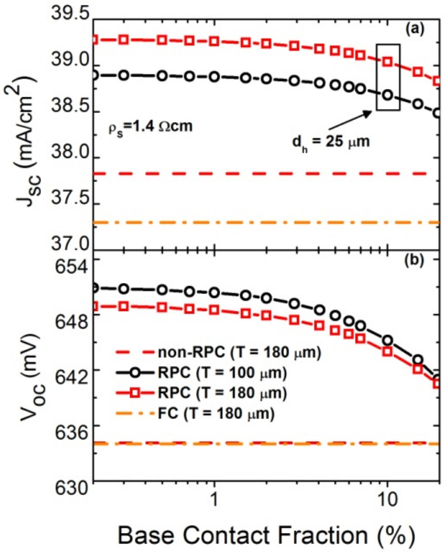

Figure 6.4: Short-circuit current J_{SC} (a) and open circuit voltage V_{OC} (b) of MWT-RPC solar cell (substrate resistivity ρ_S = 1.4 Ωcm, hole diameter d_h = µm) for two different values of substrate thickness T: 100 and 180 µm. The figure shows the comparison with the baselines (MWT non-RPC and front contact FC solar cells).

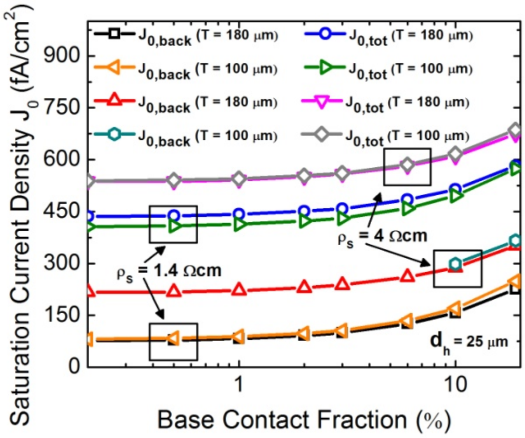

Figure 6.5: Total saturation current density $J_{0,tot}$ and saturation current density $J_{0,back}$ (defined in section 6.1.2) for MWT solar cells with RPC (substrate thickness T = 180 µm and T = 100 µm and hole diameter d_h = 25 µm) versus base contact fraction. Two different values of substrate resistivity ρ_S values are considered: 1.4 and 4 Ωcm.

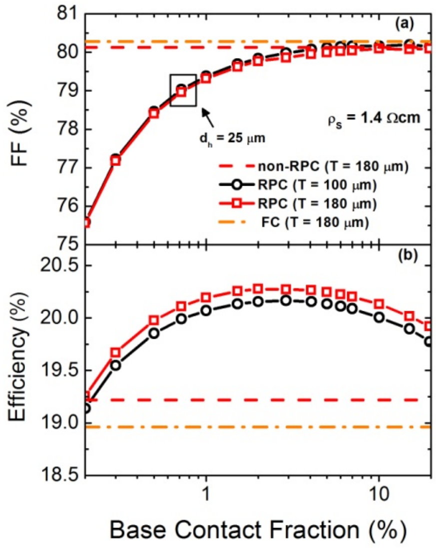

Figure 6.6: Fill Factor FF (a) and efficiency (b) of a MWT-RPC solar cell (substrate resistivity ρ_S = 1.4 Ωcm, d_h = 25 μm) for two different values of substrate thickness T: 100 and 180 μm. The figure shows the comparison with the baselines (MWT non-RPC and front contact FC solar cells).

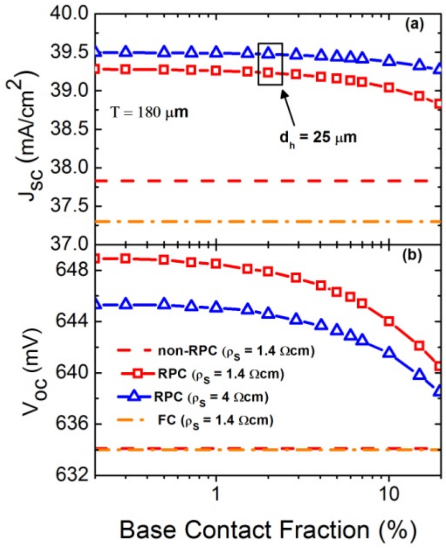

Figure 6.7: Short-circuit current J_{SC} (a) and open circuit voltage V_{OC} (b) of MWT-RPC solar cell (substrate thickness T = 180 μm, hole diameter d_h = μm) for two different values of substrate resistivity ρ_S: 1.4 and 4 Ωcm. The figure shows the comparison with the baselines (MWT non-RPC and front contact FC solar cells).

substrate thickness (Fig. 6.7). Higher minority carrier lifetimes ($\rho_S = 4\ \Omega$cm) lead to an increase in photogenerated current density and in recombination current density at the back-contact. Although we observe a decrease in terms of SRV_{eff} in case of high resistivity wafers (Fig. 6.3) the carrier recombination at the back contact is considerably increased. More in detail, at fixed C_{fr} (3%) $J_{0,base}$ = 100 fA/cm^2 in the case of ρ_S = 1.4 Ωcm and $J_{0,base}$ = 238 fA/cm^2 for ρ_S = 4 Ωcm are obtained leading to a higher V_{OC} if lower substrate resistivity is assumed as reported in Fig. 6.5. This effect is mainly ascribed to an increase of the carrier concentration close to the back interface of the cell due to the higher carrier lifetime. However, the substrate resistivity exhibits a relevant influence on FF, which strongly degrades (by reducing the optimum C_{fr}) in the case of lower doped substrate. This leads to a markedly different optimum C_{fr} for the two ρ_S values (Fig. 6.8); higher optimum C_{fr} is calculated for ρ_S = 4 Ωcm (approximately 4%). It is observed that the RPC option is less effective in MWT solar cells in terms of efficiency enhancement with respect to the baselines in the case of higher resistive substrates, mainly due to the enhanced spreading resistance.

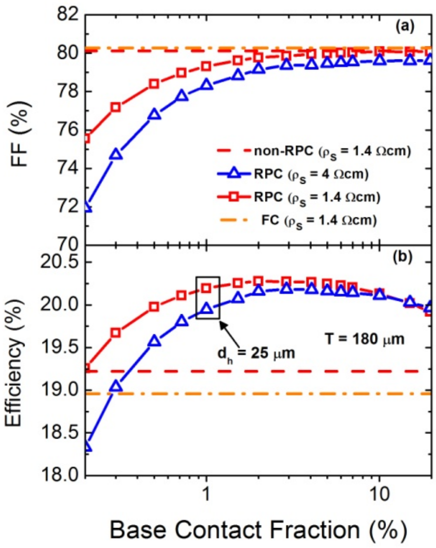

Figure 6.8: Fill Factor FF (a) and efficiency (b) of a MWT-RPC solar cell (substrate thickness T = 180 μm, d_h = 25 μm) for two different values of substrate ubstrate resistivity ρ_S: 1.4 and 4 Ωcm. The figure shows the comparison with the baselines (MWT non-RPC and front contact FC solar cells).

6.1.3.3 Impact of hole diameter

Two different hole diameters d_h, 25 μm and 100 μm (which represent practical values [166]) are considered, for substrate thickness T = 180 μm and resistivity ρ_S = 1.4

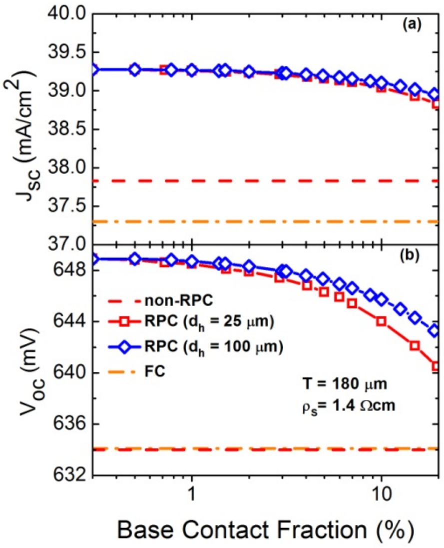

Figure 6.9: Short-circuit current J_{sc} (a) and open circuit voltage V_{OC} (b) of MWT-RPC solar cell (substrate thickness T = 180 μm, ρ_S = 1.4 Ωcm) for two different values of hole diameter d_h: 25 and 100 μm. The figures shows the comparison with the baselines (MWT non-RPC and front contact FC solar cells).

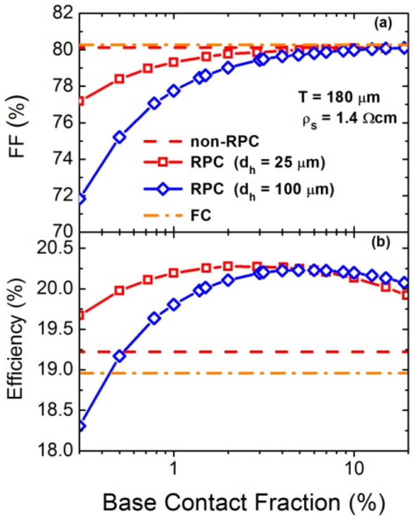

Figure 6.10: Fill Factor FF (a) and efficiency (b) of MWT-RPC solar cell (substrate thickness T = 180 μm, ρ_S = 1.4 Ωcm) for two different values of hole diameter d_h: 25 and 100 μm. The figure shows the comparison with the baselines (MWT non-RPC and front contact FC solar cells)

Ωcm. In case of relatively high C_{fr}, it is observed that, for a given C_{fr}, larger holes lead to lower SRV_{eff} as shown in Fig. 6.3. This allows to an increase in V_{OC}(Fig. 6.9). This may be ascribed to a better carrier diffusion towards the highly recombination active contact for a larger holes. In fact, at low C_{fr}, regardless the value of substrate resistivity, bulk thickness or hole size, SRV_{eff} flattens to SRV_{pass}. From Fig. 6.3 it is observed that the spreading resistance is significantly higher at low C_{fr} in the case of hole diameter 100 μm with respect to the smaller holes. Consequently, the FF degradation is more noticeable when C_{fr} is reduced (Fig. 6.10). The optimum C_{fr} is higher when large holes are used (approximately 6%). However, the calculated efficiency at the optimum C_{fr} is comparable. Furthermore, at low C_{fr} the spreading resistance contribution has marked impact on the FOMs in case of larger holes leading to lower efficiency.

6.1.4 Conclusions

In this section the impact of a passivated base in MWT solar cells exploiting a RPC scheme is discussed. A numerical simulation methodology which allows to study three-dimensional geometries without requiring cpuand memory intensive simulations is described. The approach is based on 3-D simulations of simplified structures, which are used to calibrate semi-empirical models to calculate the effective surface recombination velocity as well as the base spreading resistance. These parameters have been used to account for the local back surface field and the point contact scheme in an effective way. The 3-D simulations of the MWT solar cells have been carried out by exploiting the rotational symmetry of the spatial domain. The proposed simulation flow allows to straightforwardly carrying out analyses of the impact of different geometrical and process parameters, such as the substrate thickness, the hole size and the doping concentration in bulk on saturation current density and on main FOMs. From simulations it is observed that the passivated base may substantially enhance the conversion efficiency (above 20%). In particular, a maximum increase from 1.07 to 1.33$\%_{abs}$ with respect to baseline counterparts (MWT without RPC and front contact solar cell) is calculated in the case of 180 μm-thick cell depending upon the substrate resistivity and the substrate thickness. Simulations show a comparable optimum contact fraction (approximately 3%) for both substrate thickness values (100 and 180 μm). More marked increase in efficiency with respect to the corresponding baselines is observed in the case of the 100 μm-thick cell. Concerning the substrate resistivity impact the analyses highlighted that the RPC option in the case of higher resistive substrates MWT solar cells is less effective in terms of efficiency enhancement with respect to the baselines because of the relatively higher spreading resistance due to the lateral current flow of majority carriers. In addition, a comparison between two different holes diameter (with practical values of 25 and 100 μm) has been considered. Simulations show that optimum contact fraction is higher (approximately 6%) in case of larger holes, and that the calculated efficiency at the optimum contact fraction is comparable for both diameters. However, at lowcontact fraction the spreading resistance contribution has amore significant impact in the case of larger holes leading to lower efficiency. This allows us to conclude that for relatively low values of contact fraction smaller hole diameters are preferred with respect to larger ones.

6.2 Simulation study of LID-CID and recovery on PERC solar cells

It is well known that boron doped p-type crystalline silicon solar cells exhibit Current-Induced Degradation (CID) and Light-Induced Degradation (LID) of cell performance [178]. This effect is generally ascribed to the activation of boron-oxygen (B-O) defects and is accompanied by a reduction in bulk minority-carrier lifetime. Such degradation is almost completely recoverable if a dedicated process, which causes B-O complex dissociation, is applied. Since PERC solar cells represent one of the most promising architecture [149], the study of CID/LID effects and the regeneration techniques in PERC solar cell has been theoretically and experimentally investigated by several groups [104], [179]. In this section, starting from experimental figures of merit (FOMs) values and from the dark I-V characteristics of different samples post-recovery [180], a numerical simulation flow which allows to calibrate the model to determine the degradation and the recovery conditions is set up. In particular, as discussed in [181], B-O defects are taken into account by means of a properly tuned trap distribution. The analyses are performed on Cz-Si PERC solar cells from five different lots. The first four lots (Lot1 to Lot4) refer to a Al_2O_3 passivation film while the last considered lot (Lot5) features a SiO_x passivation. The cells are subjected to a CID and a subsequent regeneration process in different conditions and during these processes the FOMs of the cells are monitored. The remainder of the section is organized as follows. Subsection 6.2.1 describes the experimental characterization by referring to the work of Martier et al. [180]. Subsection 6.2.2 illustrates the simulation methodology and the adopted physical models. In subsection 6.2.3, the experimental values of the five considered lots are discussed in terms of FOMs and saturation current densities J_{01} and J_{02} measured during the degradation process and after different regeneration processes. Finally, the parameters adopted in the simulations which allow to physically reproduce the performance trends are reported and analyzed.

6.2.1 Experimental methodology

The experimental characterization is performed on p-type Cz-Si PERC solar cells from 4 lots (Lot1 to Lot4), fabricated by using the same technology by different manufacturers. Process, geometrical and doping parameters have been not provided by suppliers. The degradation process, as discussed in detail in [180] consists in a CID (that is comparable to LID, by applying a current of 6 A at temperature below than 45°C) during which the dark I-V parameters as well as the solar cell FOMs are monitored at intermediate time intervals up to 16h. Before degradation process the I-V characteristic of all cells is measured. Moreover, for each lot two different regeneration processes (high temperature treatment together with high

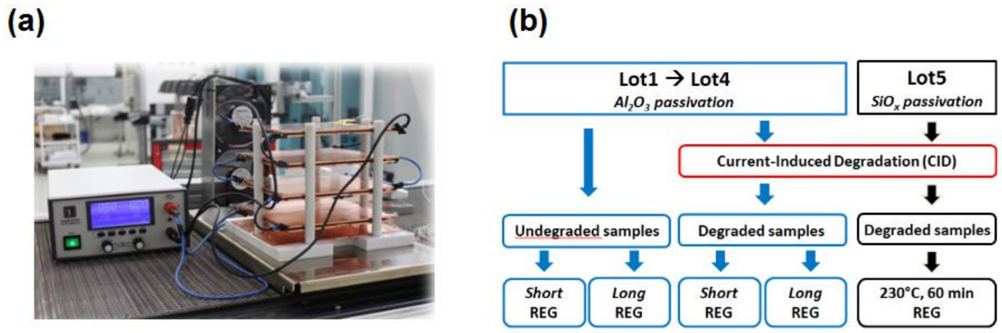

Figure 6.11: Experimental methodology step diagram.

carrier injection and fast sample cooling [180]) are applied. These two processes are different in terms of duration (in the following paragraphs they are denoted by “short” regeneration and “long” regeneration) and are performed on the degraded cells and on the undegraded cells of the considered lots. The steps of regeneration are followed by a process of degradation in order to evaluate the recovery stability. Further details of the stability check of the recovery process are reported in [180]. It is worth noting that at the starting point the Lot1 has been already regenerated. As it will be discussed in subsection 6.2.3, this explain why this lot is less sensitive to LID. A further lot (Lot5), which differs from the others in terms of passivation film (SiO_x instead of Al_2O_3), has been subjected to same degradation process and monitored after 16 hours of degrade. The following regeneration process is applied at temperature of 230°C for 60 minutes. Fig. 6.11 reports a summary diagram of the discussed processes.

6.2.2 Simulation methodology

Numerical simulations have been performed by using a TCAD device simulator [54]. A simplified 1-D structure representing a p-type Cz-Si PERC solar cell is considered. The cell is 180 μm-thick with substrate resistivity 1.5 Ωcm and exhibits a 75 Ω/sq homogeneous emitter. The PERC cell has an effective value of back surface recombination velocity of 60 cm/s. Simulations are carried out by considering the physical models parameters already successfully adopted in [9], [10], [50], [108], [109], [110], [112], [137], [182], [183], [184], [185], [186]. To account for the effective intrinsic carrier density, they include the band-gap narrowing model by Schenk [65]. For Auger recombination model the Altermatt’s parameterization [9] is adopted as well as the Klaassen’s mobility models [70], [71]. Moreover, Fermi-Dirac statistics are included. The optical generation rate profile refers to the standard AM1.5G

Table 6.2: Fitting parameters to mathematically describe the relationship between the FOM and the degradation time (t_{DEG})

	Lot1		Lot2		Lot3		Lot4	
FOM	*a*	*b*	*a*	*b*	*a*	*b*	*a*	*b*
Efficiency	0.07	20.02	0.27	19.66	0.24	20.15	0.25	19.83
FF	0.25	78.29	0.33	78.54	0.40	78.45	0.37	78.99
V_{OC}	-	-	3.17	645.44	1.89	650.72	2.47	651.74
J_{SC}	0.02	38.91	0.18	38.76	0.14	39.44	0.15	38.49

spectrum (1000 W/cm^2) [121]. In order to reproduce the measured dark saturation current density J_{02} a tuning of an effective carrier lifetime (single level trapping, Shockley Reed Hall model) within a 1 μm-deep region which includes the emitter space charge region is carried out. In the remainder of the cell (bulk region) a two-level acceptor trap distribution to model the recombination losses is assumed. The first energy level position is centered in the midgap and allows to fit the initial (non-degraded) solar cell FOMs. The second trap level is representative of the B-O complexes and its concentration value is tuned on the basis of each single process condition that has been applied to the cell. The second trap level is positioned at -0.2 eV from the midgap and the carrier capture cross sections are of $5\cdot 10^{-17}$ cm^2. These parameters are comparable to those adopted in [181]. Starting from experimental data, the numerical simulation flow aimed at reproducing the measured values for each step of the degradation-regeneration process, can be summarized in three main steps. First, the measured dark I-V characteristic data is analyzed [110] and in order to fit the J_{01} and J_{02}, the carrier lifetime within the space charge region and the traps level concentration are properly set up. Then a fine tuning of FSRV values is performed in order to reproduce the experimental values of short circuit current density (J_{SC}). Lastly, a series resistance in post processing is considered in order to reproduce the measured values of fill factor and efficiency.

6.2.3 Results and discussion

6.2.3.1 Measured data

As it can be observed in Fig. 6.12, the first four lots show different initial conditions in terms of FOMs. Moreover, the curve describing the FOM degradation levels off after 16h, which means that the B-O defects are almost activated. The relationship between the measured FOMs and the degradation time (t_{DEG}) can be mathematically described by the equation:

$$FOM = -a \cdot ln(t_{DEG}) + b \tag{6.4}$$

The values of the fitting parameters a and b assumed for each FOM are listed in Table 6.2. In case of degraded cells, the duration of the regeneration process ("short", "long") has no marked impact (Fig. 6.12 and Fig. 6.13) while in case of undegraded cells the "long" regeneration process leads to better FOMs recovery with respect to the "short" one. In detail, the effects of the process of stability check, aimed at evaluating the recovery stability [180], have a significant impact on the undegraded solar cells in case of "short" regeneration process. Due to stability check, FOMs recovery is not fully reached with respect to starting point. In terms of J_{01} (Fig. 6.14(a)) it is observed that Lot1 exhibits the lowest values due to the fact that it has been previously regenerated and the effects of the performed regeneration processes are negligible. Moreover, Lot3 and Lot4 show comparable values of J_{01} and no difference in terms of regeneration processes effectiveness is observable. However, Fig. 6.14(b) shows that, in case of undegraded cells, the "long" regeneration process leads to more marked J_{02} reduction. The measured data of Lot5, which differently from the first four lots, features a SiO_x passivation film instead of Al_2O_3, are reported in Table 6.3. By comparing the initial conditions of Lot5 with the previous four lots we observe that efficiency and V_{OC} are subjected to a better recovery than others lots while J_{SC} and FF are substantially comparable with those of Lot3. Moreover, the J_{01} value confirms the advantages in terms of recombination losses observed for this lot. Regarding the regeneration process, a satisfactory recovery in terms of performance is observed. In particular, respect to the first four lots, the grade of the recovery in terms of efficiency is slightly higher.

Table 6.3: Measured data of the Lot5 which differs from the others in terms of passivation film (SiO_x instead of Al_2O_3) for the considered conditions (start condition, degraded state and regenerated state)

Lot5	Starting point	Deg. (16 hours)	Reg. (230°C, 60 min)
J_{SC} *(mA/cm²)*	39.45	39.14	39.32
V_{OC} *(mV)*	661	652	659
FF *(%)*	79.16	78.05	79.16
Efficiency *(%)*	20.66	19.92	20.5
J_{01} *(fA/cm²)*	400	550	430
J_{02} *(pA/cm²)*	6.7	17	7.3

6.2.3.2 Simulation results

The considerations resulting from the analysis of the measured data are confirmed by simulation results (Fig. 6.15), which allow to reproduce the experimental trends. In particular, the first level trap concentration values (reported in the caption of Fig. 6.15(a)) are consistent with the J_{01} values at the starting point and with the

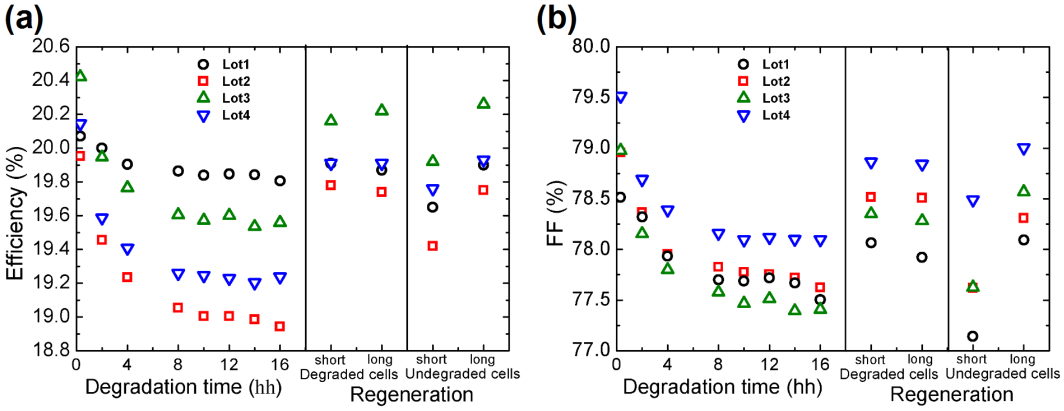

Figure 6.12: Measured values of efficiency (a) and Fill Factor (FF) (b) for the first four lots in different conditions (degradation, "short" and "long" regeneration in case of degraded and undegraded cells).

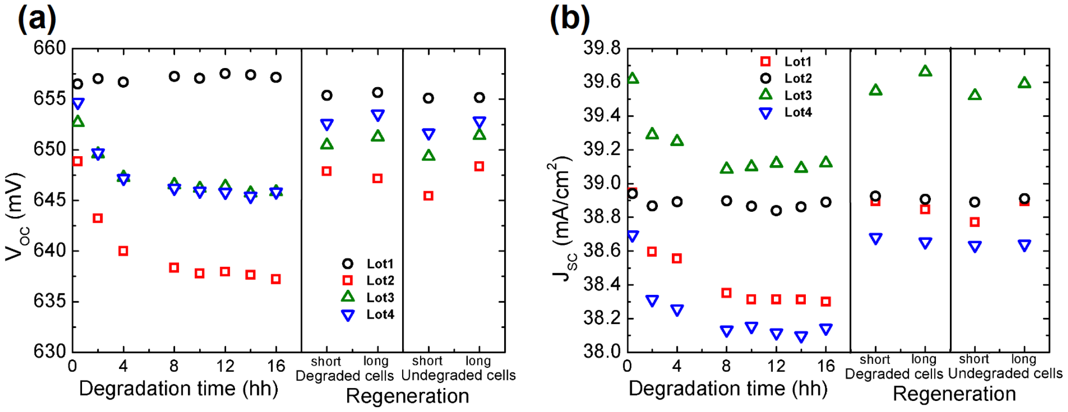

Figure 6.13: Measured values of open circuit voltage (V_{OC}) (a) and short circuit current J_{SC} (b) for the first four lots in different conditions (degradation, "short" and "long" regeneration in case of degraded and undegraded cells).

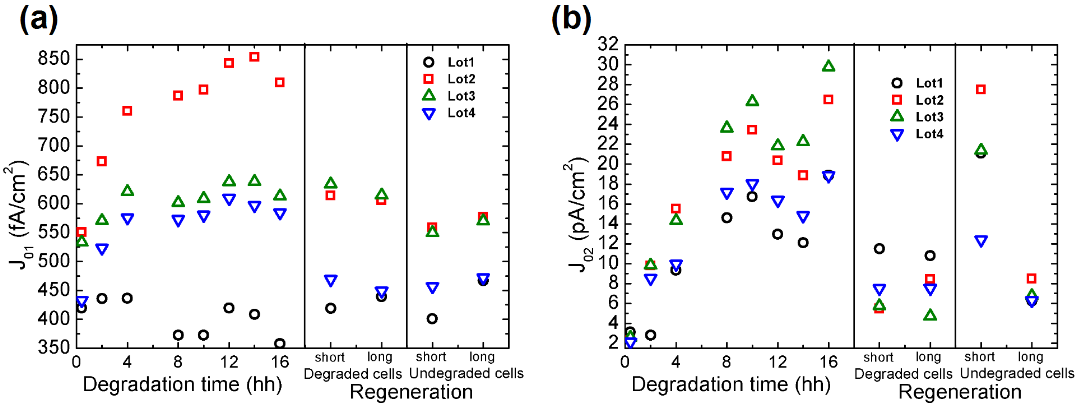

Figure 6.14: Measured values of saturation current density J_{01} (a) and J_{02} (b) for the first four lots in different conditions (degradation, “short” and “long” regeneration in case of degraded and undegraded cells).

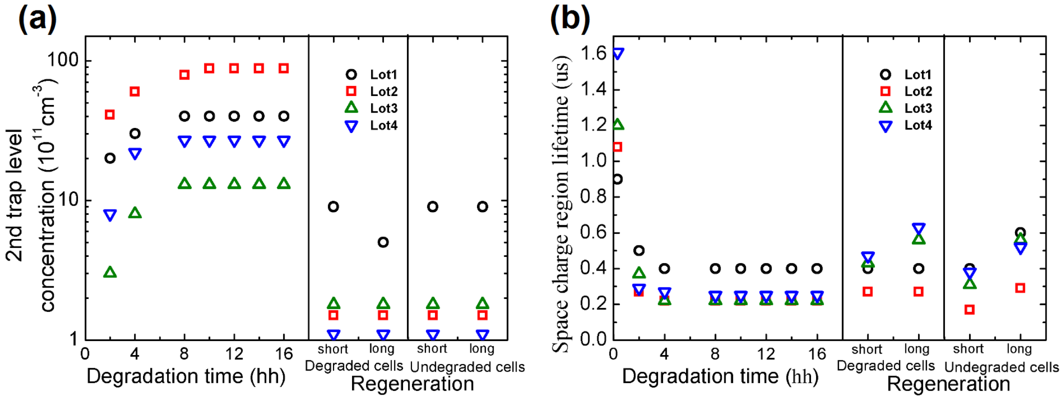

Figure 6.15: (a) Values of 2nd trap level concentration for the first four lots in different conditions (degradation, “short” and “long” regeneration in case of degraded and undegraded cells) adopted in the simulations. The first level trap concentration values adopted in the simulations are $1.07{\cdot}10^{13}$ cm^{-3}, $1.65{\cdot}\ 10^{13}$ cm^{-3}, $1.39{\cdot}10^{13}$ cm^{-3} and $1.22{\cdot}10^{13}$ cm^{-3} for the Lot1, Lot2, Lot3 and Lot4, respectively. (b) Values of the space charge region lifetime for the first four lots in different conditions (degradation, “short” and “long” regeneration in case of degraded and undegraded cells) adopted in the simulations.

Table 6.4: Values of the 1st and 2nd trap level concentration and of the space charge region (SCR) lifetime adopted in the simulations of the Lot5 for the considered conditions (start condition, degraded state and regenerated state.))

Lot5	Starting point	Deg. (16 hours)	Reg. (230˚C, 60 min)
1st trap level conc. *(10^{13} cm^{-3})*	0.7	0.7	0.7
2nd trap level conc. *(10^{11} cm^{-3})*	-	15	1
SVR lifetime *(μs)*	0.4	0.1	0.3

measured V_{OC} (Fig. 6.12(a)). From Fig. 6.15(a), which illustrates the second level trap concentration versus process conditions, the saturation of the FOMs degradation curve and the B-O defects deactivation is not easily noticeable thanks to the regeneration process. The assumed concentration values of the two trap levels allowed for a perfect match between experimental and calculated J_{01} and J_{02} (not shown).

Regarding the value of carrier lifetime within space charge region, simulations reveal that a regeneration process characterized by longer time is preferred in terms of performance recovery (Fig. 6.15(b)). Moreover, also the Lot5 is analyzed by means of the same simulation approach. The values of the trap levels concentration and the space charge region lifetime adopted in the simulation are reported in Table 6.4. The better measured initial performance of this lot described in the previous subsection are confirmed by the 1st trap level concentration value which is smaller than those of all the previous lots (Fig. 6.14(a)). In addition, the grade of the recovery is observable from the value of the 2nd trap level concentration. Although after degradation of 16 hours the 2nd trap level has a relevant impact, it can be concluded that at the end of the recovery process (230°C for 60 min) the BO complex are almost completely deactivated. The last consideration regards the space charge region lifetime. From the simulations results it can be noticed that after the regeneration process this lifetime is close to the starting point value explaining the behavior of the measured J_{02} value responsible to the FF variations. Lastly, from simulation results it is worth noting that the series resistance contribution has not a relevant impact in terms of FOMs confirming the fundamental role of the trap density. On the basis of this study, it is concluded that the effects of degradation and regeneration processes are well reproducible by considering B-O complexes activation and deactivation in the bulk region and in the space charge region. While the adoption of a proper trap distribution in the bulk is suitable to describe the behavior in terms of J_{01} and V_{OC}, the influence of the degradation-regeneration processes on FF and J_{02} could be reproduced only by tuning an equivalent carrier lifetime in the space charge region. The PERC solar cells considered in this section, which have been subjected to LID-CID and regeneration processes, exhibit efficiency recovery up to 98.9%. The extent of the efficiency recovery is directly related to the duration of the process in accordance with [180]. However, in the case of lots previously regenerated (Lot1) the impact of LID-CID is less remarkable, leading to an efficiency recovery of 99.3%.

6.2.4 Conclusions

In this section, the measured FOMs and saturation current densities J_{01} and J_{02} of Cz-Si PERC solar cells from five different lots are analyzed. The first four lots are characterized by a Al_2O_3 passivation film while the last lot features a SiO_x passivation. The cells are subjected to a Current-Induced Degradation process up to 16 hours where the FOMs are monitored at different intervals. Moreover, for each of the first four lot two different regeneration processes, which are different in terms of duration, are performed on the degraded cells and on the undegraded cells while in case of the SiO_x passivated lot the regeneration process is carried out at temperature of 230°C for 60 min only for degraded cells. Starting from the experimental data, in order to reproduce the measured values for each step of the both degradation and regeneration processes, a numerical simulation flow is performed by using a TCAD standard simulator. In particular, with regards to the recombination losses in the bulk region a two-level trap distribution is assumed. The first trap level allows us to fit the initial (non-degraded) solar cell FOMs while the second one is representative of the B-O complexes. The traps level concentration is properly tuned on the basis of each single process condition that has been applied to the cell in order to reproduce the measured data. The curve describing the FOMs degradation levels off after 16h, which means that the B-O defects are almost activated, and in terms of recovery in the case of undegraded cells the regeneration process characterized by a longer time is preferable than the shorter one while in case of degraded cells, the duration of the regeneration process has no marked impact. The SiO_x passivated lot exhibits greater efficiency and V_{OC} than others lot and the J_{01} value confirms the advantages in terms of recombination losses. Regarding the regeneration process we observe that the grade of the recovery in terms of efficiency is slightly higher than previous lots. On the basis of the proposed simulation study, it can be concluded that the adopted trap-model, in combination with a tuning of an equivalent carrier lifetime in the space charge region, correctly reproduce the influence of the degradation-regeneration processes on the FOMs of the presented solar cells.

6.3 Simulation study of multi-wire front contact grids for silicon solar cells

Conventional industrial H-pattern silicon solar cells adopt a grid of screen printed busbar and fingers fabricated starting from silver pastes. Inside PV modules, solar cells are encapsulated by a layer stack of glass and a polymeric material. The total fabrication cost of the module is markedly sensitive to the amount of silver-based paste used for the front-contact grid. With this regard, the silver (Ag) paste consumption of industrial screen-printed crystalline silicon solar cells is within the range 120 mg - 200 mg per wafer [187]. In the recent years, one challenging task for photovoltaic industry is to reduce the consumption of Ag paste. However, paste saving techniques are often associated to an increase of total series resistance leading to Fill-Factor (FF) degradation and significant power loss. Moreover, the front-grid design has a marked impact in terms of light shading losses [169]. Multi-wire (MW) schemes [188], [189] represent an alternative option to busbars (BBs), aimed at reducing the silver paste consumption in silicon solar cells. In the case of MW schemes, busbars are replaced by copper wires. Due to their geometry, MW lead to photogeneration enhancement with respect to standard ribbon busbar [190] thanks to a better light-trapping within the cell layer stack consisting of glass, encapsulant and silicon. Moreover, MWs are straightforwardly implementable on existing cells offering a full compatibility with different device architectures. In particular, only a few technical details of the process have to be modified, by using a different kind of cell stringer [188]. Optical simulations of MW can be helpful in order to study the light trapping properties of the MW scheme. Several authors have theoretically and experimentally studied the effective optical shading of encapsulated solar cells featuring aerosol-printed and plated fingers presenting a circular cross-section similar to that of copper wires [191]. They reported that the effective optical shading ranges between one third to half of the wire diameter. Blakers [191] has calculated the effective shading of a rough half-circular encapsulated finger and, by a comparison to reflection measurements, he presented experimental data to support calculations of the effective optical shading. In [190], the effective reflection on different types of metal fingers has been analysed by theory and experiments. However, one issue that has not been addressed to date is that of the sensitivity of the effective optical shading of wires to their geometry and density, to the thickness of the encapsulant layer as well as to the optical reflectance of the cell front interface. The influence of these parameters on the light trapping enhancement due to MW may have a relevant impact on the cell design. In this section, electro-optical simulations of MW and BBs based solar cells are performed in order to calculate the effective shading factor, the enhancement of conversion efficiency and the paste saving of the MW scheme with respect to the BBs design. In particular, by means of optical simula-

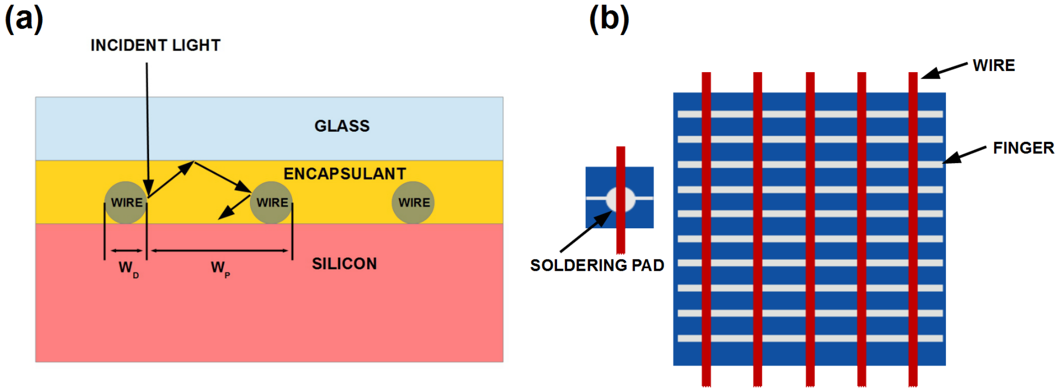

Figure 6.16: (a) Sketch of the encapsulated multi-wire solar cell (cross-section, not to scale) and (b) top view schematic of the contacting grid with the detail of a soldering pad.

tions, the impact of the geometries of the stack layer, of the wire coverage fraction and diameter, and of cell front reflectivity on the wire effective optical shading is analyzed. An extensive analysis of different wire diameters has been carried out investigating coverage fraction values up to 20%. The remainder of the section is organized as follows. Subsection 6.3.1 describes the simulation methodology. Subsection 6.3.2 discusses the results of the effective shading of copper wires in the case of encapsulated industrial crystalline silicon solar cells calculated by means of a ray-tracing simulation tool. In addition, the calculated values of optical effective shading is used to determine the conversion efficiency enhancement with respect to the reference silver BBs scheme, and to calculate the paste saving achievable by the adoption of the MW schemes. Finally, subsection 6.3.3 reports the main conclusions of the study.

6.3.1 Simulation methodology and studied solar cells

In this study, a stack of a 3.2 mm-thick glass layer and 450 μm-thick encapsulant (Fig. 6.16(a)) is considered, representing typical values adopted in commercial modules [192]. Fig. 6.16(b) shows a schematic top view of the cell where standard silver busbar are replaced by copper wires. The two-dimensional simulation domain is the half of the wire pitch W_P. Mirror and absorbing boundary conditions have been assumed at sides and at bottom of the domain, respectively. The considered c-Si solar cell features a p-type 180 μm-thick substrate with 1.5 Ωcm resistivity. A 75 Ω/sq phosphorous doped homogeneous emitter and an aluminium back surface field (Al-BSF) have been assumed [109]. The size of the cell is 15.6 cm x 15.16 cm. Optical simulations have been performed by using a standard raytracer [52] and by considering either a textured front interface with regular upright pyramids or a simpler planar surface. In both cases, the cell is coated by a 75 nm-thick silicon nitride layer. At the silicon/encapsulant interface the wavelength-dependent reflectivity (calculated separately) has been imposed. The assumed wavelength span for the simulation is 30 nm, which has been previously validated as a good trade-off between computational effort and accuracy. The rays distribution is non-uniform to save memory and to reduce the computation time. In particular, the spatial ray density is higher in regions close to the wires (minimum spacing 0.1 μm) while in the mid region between wires the maximum ray spacing is 1 μm. It is assumed that the reflectivity of the encapsulant-wire interface is equal to 1. This assumption has been done in order to study the impact of the circled shape respect to the standard geometry and to compare the values obtained from the simulations with those reported in the literature. Therefore, the wavelength dependence of the Copper/Encapsulant interface has not been considered and this leads to an overestimation of the calculated optical parameters. In particular, an increase of $0.7\%_{\mathrm{rel}}$ is observed for the optical shading factor values with respect to the wavelength dependent case. The optical properties of glass and encapsulant are modeled according to [193] and [194], respectively. The wire effective optical shading factor $\mathrm{K_{shading}}$ is defined as:

$$K_{shading} = \frac{W'}{W_D} \tag{6.5}$$

where W_D is the wire diameter and $W^{'}$ is the width of the ideal planar metal providing the same photo-generated current density ($\mathrm{J_{PH}}$) obtained by the wire scheme. The relative enhancement of photo-generated current ($\mathrm{J_{PH,enh}}$) due to the MW scheme is:

$$J_{PH,enh} = \frac{J_{PH} - J_{PH,ideal}}{J_{PH,ideal}} \tag{6.6}$$

where J_{PH} and $J_{PH,ideal}$ are the photo-generated current densities in the case of wires and in the case of ribbon busbar with ideal optical shading $\mathrm{K_{shading}} = 1$, respectively. The standard reference spectrum ASTM AM1.5G [121] and 1000 W/m^2 irradiance, with light normally incident on the device plane are considered in order to calculate the photo-generated current density. Electrical simulations have been performed with the calculated effective shading of copper wires $\mathrm{K_{shading}}$ in order to determine the conversion efficiency enhancement for the MW cases with respect to the reference silver BBs scheme (3, 4 and 5 BBs). In the MW cases, the optimum number of wires ($\mathrm{N_W}$) is evaluated as the one providing the maximum conversion efficiency. A reasonable range of $\mathrm{N_W}$ (from 3 to 50) is explored and it is observed that it is strongly dependent on the number of busbar and on the wire diameter. For ribbon busbar and wires soldering pads (size set to 1.5 times the wire diameter) ideal shading is assumed and for silver fingers an effective shading factor equal to 0.42 [190]. This assumption is realistic by considering the aspect ratio and the geometry of fingers and pads. The current-voltage characteristics under illumination accounting for optical shading and contact by fingers as well as for emitter resistance have been performed by using a drift diffusion simulator as described in [50], [174], [184], [182] and [185], accounting for physical models as described in [174]. The contribution of the contact grid resistance to the total series resistance as well as the optical shading due to busbar for the reference design or due to wires in the case of MW are accounted for in post-processing by properly correcting the I-V characteristic. In this study, a fixed total coverage fraction of the silver busbar for the reference design (2.8%) is assumed. The finger height is set to 13 μm in the case of BBs scheme. According to the number of BBs and to the finger width (the following finger widths are considered: 25 μm, 45 μm, 65 μm, 85 μm), the number of fingers has been optimized allowing a fair comparison between different grid configurations. The optimum number of fingers varies within the range 74 - 150. In the calculation of the total series resistance, it is included the emitter and the contact resistance, the grid contribution and the resistance due to cell interconnect wires [15]. Such an interconnect wire is assumed to be 1 cm-long and 200 μm-thick. In order to calculate the silver paste savings due to the MW schemes, the fingers past consumption has been determined by assuming a 7 mg/mm^3 silver paste [195]. This results in a total paste weight of 167 mg for a wafer featuring $W_F = 25$ μm and 3 BBs, comparable to values reported in [187], [188], [189].

6.3.2 Results and discussion

6.3.2.1 Spectral dependence of the photo-current density enhancement

Fig. 6.17 shows the radiation wavelength (λ) dependence of the photogenerated current density enhancement $J_{PH,Enh}$ with respect to the reference silver-BBs case. It can be observed that $J_{PH,Enh}$ is approximately constant for λ below 1000 nm due to the weak dependence on photon energy of the optical properties of materials and surface reflectivity. For $\lambda > 1000$ nm, the effectiveness of the light scattering is more pronounced and is affected by a significant dependence of front reflectivity on wavelength. By increasing the number of wires from 10 to 50, $J_{PH,Enh}$ increases due to the stronger mutual influence among wires. Indeed, simulations show that a higher number of wires leads to increased optical absorbance in silicon combined with lower parasitic absorption in the encapsulant layer. Overall, this results in a lower external reflectance. It is worth noting that, despite $J_{PH,Enh}$ is higher in the case of denser wire grid (50 wires), the influence on J_{PH} is compensated by a higher coverage fraction (C_f) which leads to more optical shading. For instance, with $W_D = 300$ μm, J_{PH} decreases from 37.56 mA/cm^2 to 36.97 mA/cm^2 (-1.5%$_{rel}$) when N_W increases from 10 to 50. Despite this, from Fig. 6.17, where none shadowing effect is considered, the expected relative increase in J_{PH} is approximately 7% for higher N_W. However, higher N_W results in lower total series resistance.

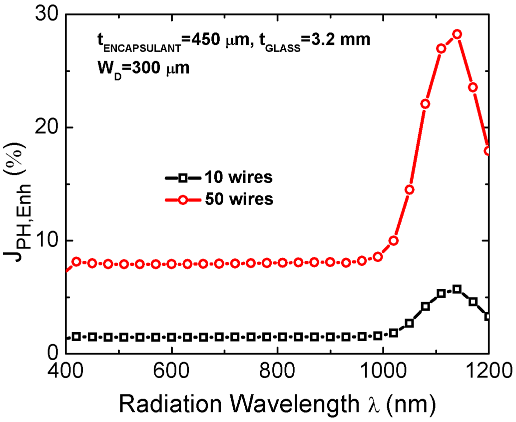

Figure 6.17: Wires-related photo-generated current enhancement ($J_{PH,Enh}$) versus the radiation wavelength (λ) for two different number of wires: 10 and 50. $t_{ENCAPSULANT}$, t_{GLASS} and W_D are the encapsulant thickness, the glass thickness and the wire diameter, respectively.

6.3.2.2 Influence of front reflectivity, wire diameter and wire coverage fraction on the effective optical shading

Two markedly different reflectivity characteristics at the front interface have been analyzed, one for textured interface and the second for planar interface, both coated by 75 nm-thick silicon nitride (called SiN_x) (Fig. 6.18(a)). As expected, the textured cell exhibits a significantly lower reflectance. Fig. 6.18(b) shows the optical shading versus the wire C_f. It can be observed that for a given wire diameter (W_D = 200 μm) at relatively lower C_f (corresponding to a number of wires N_W up to 50) the light trapping due to encapsulated MW is more effective in the case of planar front interface ($K_{shading} = 0.16$) as compared to the textured case ($K_{shading} = 0.22$). Indeed, higher incident power is reflected by the planar front interface resulting in an enhanced scattering from the encapsulant/wire interface although, due to the strong difference in average reflectivity, the textured morphology results in higher J_{PH} ($+5.2\%_{rel}$). For C_f-values above 7% the influence of the front interface reflectivity is less relevant probably due to the reduced wire spacing. In addition, we observe that, at fixed C_f, $K_{shading}$ is strongly dependent on wire diameter. As it can be observed in Fig. 6.18(b), from the optical point of view, MW schemes take advantage from higher diameters, especially when C_f is lower than 20%. Probably this is due to the larger rounded cross section surface area of the wire, which plays a role in lowering $K_{shading}$. The calculated values of effective optical shading factor $K_{shading}$ = 0.22 (C_f up to 3%), and $K_{shading} = 0.46$ (W_D = 40 μm, C_f = 10%) are comparable to those discussed in [196]. In addition, on the basis of thepresented simulations, for C_f lower than 3%, $K_{shading}$ is not markedly affected by the wire diameter. This is relevant for the front grid design since, as it will be shown in the following subsec-

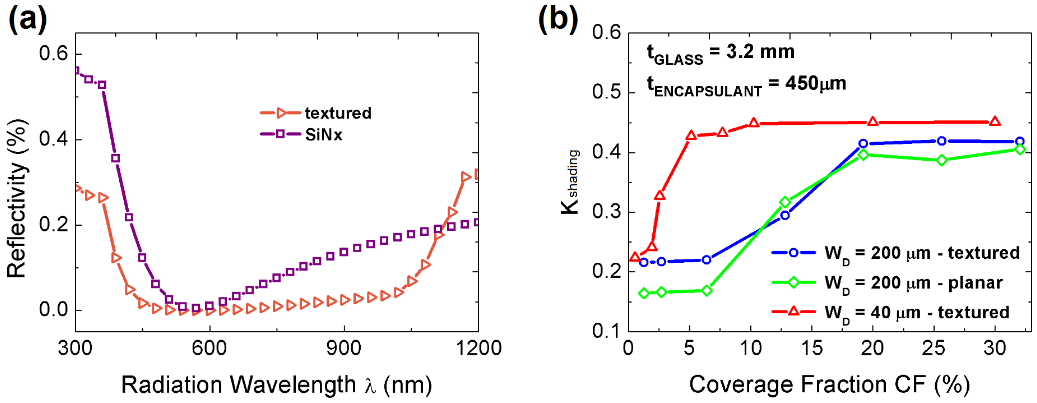

Figure 6.18: (a) Reflectivity (measured) versus radiation wavelength (λ) in the case of textured and planar front interface, both coated by 75 nm-thick silicon nitride ($\mathrm{SiN_x}$) and (b) effective optical shading factor $\mathrm{K_{shading}}$ for wire diameter $\mathrm{W_D}$ = 200 μm (textured and planar front interface) and $\mathrm{W_D}$ = 40 μm (textured front interface). Calculations have been carried out assuming glass thickness $\mathrm{t_{GLASS}}$ = 3.2 mm and encapsulant thickness $\mathrm{t_{ENCAPSULANT}}$ = 450 μm.

tions, the optimum $\mathrm{C_f}$ corresponding to the peak conversion efficiency is relatively low.

6.3.2.3 Influence of encapsulation stack geometry

Simulations show that $\mathrm{K_{shading}}$ is dependent on the geometry of the material stack, in particular on the encapsulant thickness $\mathrm{t_{ENCAPSULANT}}$. Fig. 6.19 shows that for a number of wires comparable to the optimum one (about 20 wires, Subsection 3.2) and glass thickness equal to 3.2 mm ($\mathrm{W_D}$ = 200 μm and $\mathrm{W_D}$ = 40 μm), $\mathrm{K_{shading}}$ is markedly dependent on the encapsulant thickness, when its value is comparable with $\mathrm{W_D}$ (200 μm and 40 μm are considered in this case). However, when $\mathrm{t_{ENCAPSULANT}}$ is several times $\mathrm{W_D}$, the influence of the encaplsulant layer thickness is not appreciable. Therefore, in order to reduce the material cost, for $\mathrm{W_D}$ within the range 100 μm – 300 μm an encapsulant layer thickness of 400 μm is enough to ensure a low $\mathrm{K_{shading}}$.

6.3.2.4 Electrical simulation: calculation of the solar cell main figures of merit under illumination

In this part, the optimum number of wires for different diameters is calculated and the main FOMs of the solar cell with those of the reference grid design are compared. For the reference scheme 3, 4, and 5 silver BBs are assumed. Calculations have been performed for finger width $\mathrm{W_F}$ from 25 μm to 85 μm and for wire diameter $\mathrm{W_D}$ from 100 μm to 400 μm. The materials parameters used in the calculations

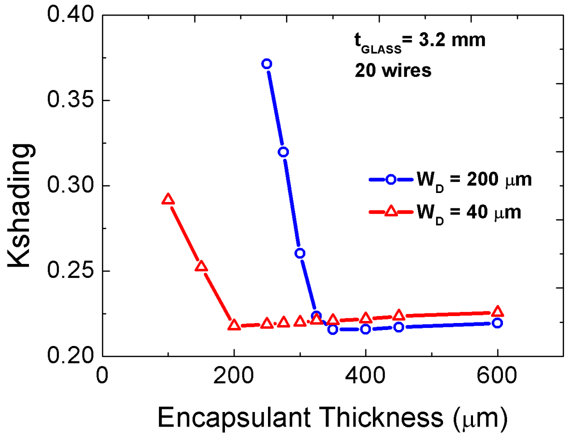

Figure 6.19: Effective optical shading factor K_{shading} versus encapsulant thickness $t_{\mathrm{ENCAPSULANT}}$ for wire diameter $W_D = 200\ \mu m$ and $W_D = 40\ \mu m$ with glass thickness $t_{\mathrm{GLASS}} = 3.2$ mm and for 20 wires.

are summarized in Table 6.5. Fig. 6.20 illustrates the contributions to the series resistance due to fingers, wires, busbar and the cell interconnect wires. The most relevant contribution is that of wires in the case of MW, while the finger resistance has a minor impact.

Table 6.5: Materials parameters used in the calculations.)

Parameter	Value
Silver resistivity (Ω·cm)	$2.7{\cdot}10^{-6}$
Copper resistivity (Ω·cm)	$1.7{\cdot}10^{-6}$
Specific front contact resistivity (Ω·cm^2)	$1.7{\cdot}10^{-6}$
Emitter sheet resistance (Ω/sq)	75

For this reason, in order to save paste, the finger thickness to 6.75 μm is decreased in the case of MW respect to the thickness of 13 μm in the case of silver BBs. Into simulations, in terms of loss parameters, an infinite shunt resistance and the same saturation current density for each configuration of number of finger (N_F) and respective width (W_F) are considered. The performance of the cell are valued considering the Fill Factor (FF) and the conversion efficiency. More in detail, in the case of wire diameter $W_D = 100\ \mu m$, a relatively relevant wire contribution to the total parasitic resistance (Fig. 6.20(a)) due to the low value of the diameter, leads to strong FF degradation (Figs. 6.21(a) and 6.22(a)) which does not allow an efficiency enhancement with respect to the BBs design (Figs. 6.21(b) and 6.22(b)). This does not occur for larger W_D (Fig. 6.20(b)). Moreover, even the conversion efficiency is limited due to the resistive losses and a trade-off between light shading

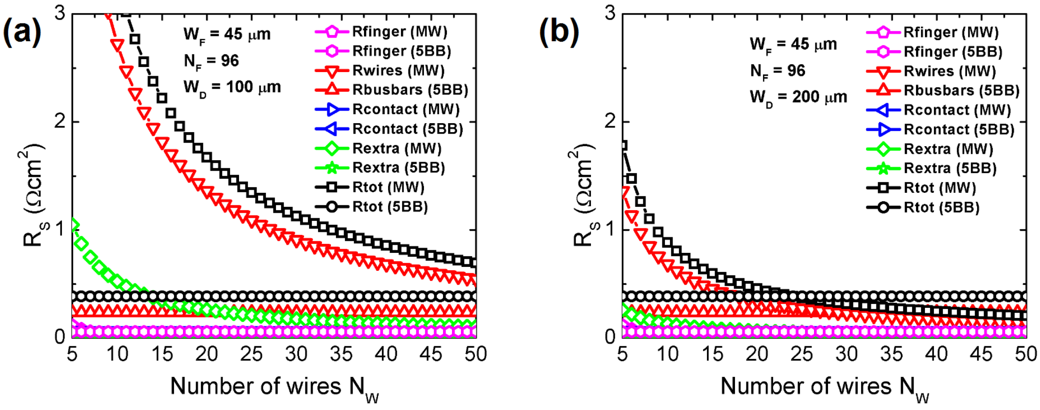

Figure 6.20: Significant calculated contributions to the total parasitic resistance per unit area in the case of multi-wire and busbar grids. Two wire diameters (W_D are illustrated: (a) 100 μm and (b) 200 μm. R_{extra} denotes the cell interconnect wires contribution to the total resistance. The contribution of the metal-semiconductor contact resistance [15] is negligible and other types of contact have not been considered.

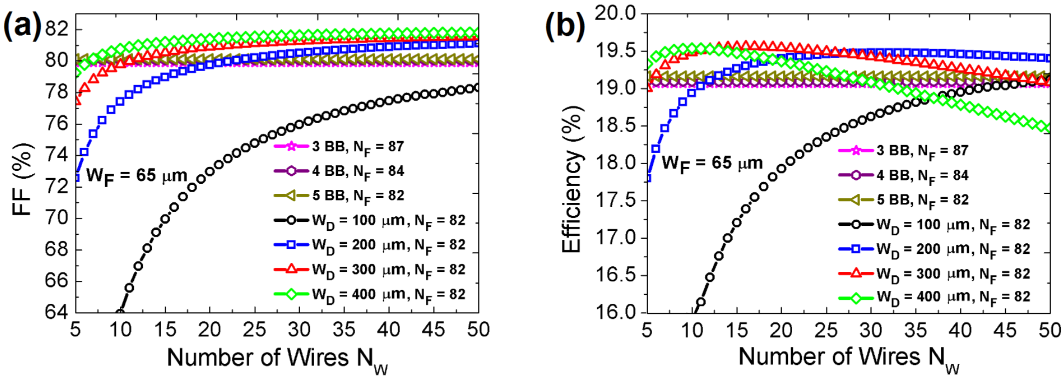

Figure 6.21: Calculated Fill Factor (a) and efficiency (b) in the case of multi-wire and busbar (3, 4, 5 BBs) schemes for finger width W_F = 45 μm. Multiwire have been simulated assuming 96 fingers, while BBs solar cells with an optimized number of fingers N_F.

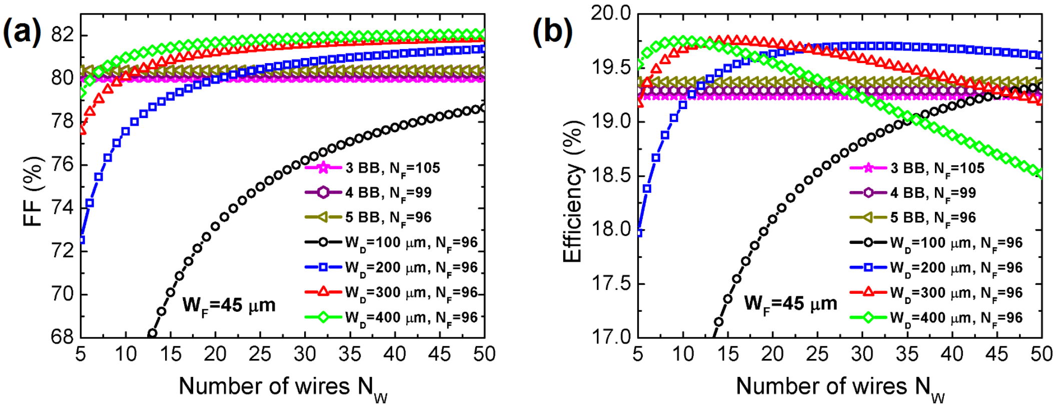

Figure 6.22: Calculated Fill Factor (a) and efficiency (b) in the case of multi-wire and busbar (3, 4, 5 BBs) schemes for finger width $W_F = 65$ μm. Multiwire have been simulated assuming 82 fingers, while BBs solar cells with an optimized number of fingers N_F.

and resistance of the front contact might be considered to obtain the maximum efficiency. In fact, as the wire diameter W_D increases, a lower number of wires NW_W is requested to obtain the maximum efficiency (Figs. 6.21 and 6.22). It is worth noting that the efficiency enhancement of the MW cell with respect to the BBs option depends on wire diameter, fingers width and number of BBs of the baseline (Figs. 6.21 and 6.22). Indeed, the higher is the number of BBs, the lower is the resistance of fingers, leading to higher efficiency of the baseline (BBs-cell). The efficiency increases up to $0.37\%_{abs}$ with respect to the 5 BBs design (W_D = 300 μm, W_F = 45 μm) and up to $0.5\%_{abs}$ compared to 3 BBs reference. In the last case, the silver paste consumption decreases from 123 mg to 30 mg per wafer assuming a paste density of 7 mg/mm^3 (for standard single-print screen printed cells is between 120 mg and 200 mg [187]). A further interesting aspect is the analysis of the impact of the encapsulant stack. In Fig. 6.23 the calculated shortcircuit current density J_{SC} versus the number of wires for encapsulated MW cells is compared to that without encapsulant and glass for wire diameter W_D = 300 μm, and finger width W_F = 45 μm. In addition, the comparison with a three busbar (3 BBs) solar cell is illustrated. It can be observed that at the optimum number of wires in terms of efficiency (N_W = 19 for encapsulated cell and N_W = 8 non-encapsulated cell), J_{SC} is higher in the case of MW thanks to optical effects resulting from the adoption of a circular shape (wire). Moreover, the gain in terms of J_{SC} is higher in the case of encapsulated cell thanks to the advantages provided by this stack [194]. This, in addition to the overall parasitic series resistance reduction, ensures an increase in efficiency in the case of encapsulated cells due to the advantages obtained in terms of optical interactions considering these materials (glass and encapsulant) in the

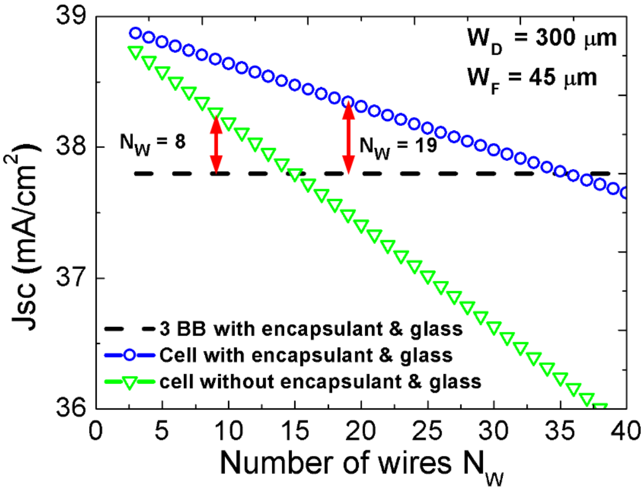

Figure 6.23: Short circuit current J_{SC} versus number of wires for cell with encapsulant and glass or without encapsulant and glass. W_D denotes the wire diameter and W_F the finger width. A comparison with a three busbar (3 BBs) solar cell is shown. The red arrows denote the gain in terms of J_{sc} (with respect to 3 BBs) at the optimum number of wires NW.

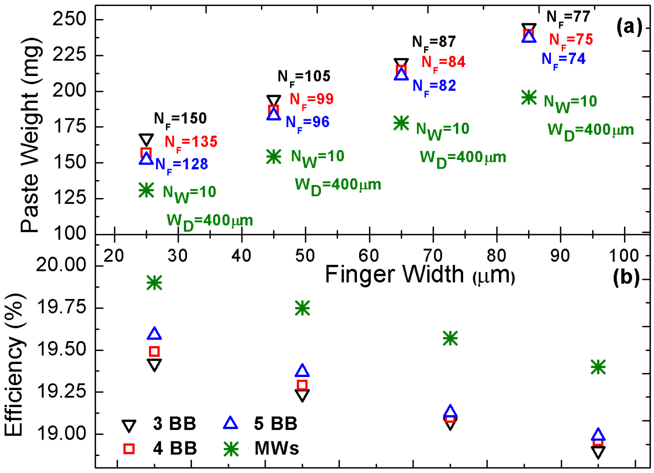

Figure 6.24: Paste Weight (a) and efficiency (b) in the cases of multi-wire (MW) and busbar (3, 4, 5 BBs) scheme for finger width W_F from 25 μm to 85 μm. N_F denotes the optimum number of fingers, NW and W_D denote the optimum number of wires and the optimum wire diameter, respectively.

electro-optical simulations. Finally, Fig. 6.24(a) shows the paste consumption for four cases of finger width W_F with 3 BBs, 4 BBs, 5 BBs (the optimum number of fingers N_F reported in this figure is calculated on the basis of the front grid parameters) and for the MW (the figure illustrates the optimum number of wires N_W and the wire diameter W_D). It is worth noting that, overall the paste weight increases with increasing finger width. Hence, the decrease in the optimum number of fingers is associated to a widening of finger width which leads to an increase of paste volume. In addition, we observe that the relative gain in efficiency is higher for wider finger. The respective calculated efficiencies are shown in the Fig. 6.24(b). Moreover, a decrease in maximum efficiency occurs for wider fingers due to Fill-Factor degradation.

6.3.3 Conclusions

In this study, by using a ray-tracing simulation tool, the impact of geometries and optical properties of the materials on effective optical shading in the case of encapsulated industrial silicon solar cells which adopted multi-wire scheme has been analyzed. Electro-optical simulations of MW and multi-busbar based solar cells are performed in order to calculate the effective shading factor, the enhancement of efficiency and paste saving with respect to BBs design. On the basis of this simulation study, such parameters have been revealed to be strongly dependent on the geometries of the encapsulant as well as on the optical reflectivity of the cell front interface. In particular, for encapsulant thickness close to the wire diameter, the effective optical shading is markedly dependent on the encapsulant thickness. Instead, when the encapsulant thickness is much larger than the wire diameter we obtained an effective optical shading factor of 0.16 for planar front interface and of 0.22 for textured front interface. In addition, it is observed that, at fixed C_f, the effective optical shading is strongly dependent on the wire diameter. In particular, MW schemes take advantage of higher diameters, especially when C_f is lower than 20%. The calculated values of effective optical shading factor is 0.22 for C_f up to 3% independently of the wire diameter and 0.46 for lower wire diameter and $C_f = 10\%$ and these values are comparable to those reported in other works. Indeed, although for a given C_f higher W_D means a lower number of wires, the rounded cross section surface of the wire plays a role in lowering effective shading. The optimum number of wires at different diameters has been calculated and the solar cell main FOMs have been compared with those of the reference grid design assuming 3, 4, 5 silver BBs. It is observed that the most relevant resistance contribution is that of wire in the case of MW, while the finger resistance has minor impact. The efficiency enhancement of the MW cell with respect to the BBs option depends on wire diameter, fingers width and number of BBs of the baseline. In addition, for the given cell design, an absolute enhancement of efficiency up to $0.5\%_{\text{abs}}$ with respect to the

3 BBs design and a paste saving up to 50 mg in case of MW design are calculated.

Chapter 7

Conclusions

The presented thesis on "Modeling and characterization of semiconductor devices for energy efficiency" comprises fundamental studies on one of the most effective technology aimed at producing electrical energy from renewable and sustainable energy source, the photovoltaic technology.

Since the global photovoltaic market constantly demands more efficient and cost-effective technology, the photovoltaic research is driven by the need of investigating novel solar cells architectures in order to enhance the conversion efficiency and to guarantee, at the same time, low-cost manufacturing process.

Nowadays, silicon-based solar cells still represent the most widely used technology in photovoltaic, with a market share of around 93% in 2016. Among silicon-based solar cells, crystalline silicon (c-Si) solar cells cover a significant percentage.

The numerical simulations of solar cells acts as a key factor for the photovoltaic research and industry, since an accurate and predictive modeling is suitable for identifying and analyzing promising solutions aimed at fulfilling the photovoltaic market request.

This thesis reports remarkable numerical simulation studies of silicon-based solar cells. The challenge of the presented work is to explain several behaviors revealed by the experimental characterization of different solar cell architectures (or concepts), and to provide useful findings to the industrial or to the experimental part. All the simulations were performed in collaboration with technological partners, working on the application of such advanced and promising findings on both novel and well-known cell structures. This aspect allows to increase the relevance of the presented modeling activities based on state-of-the-art physical and electrical models.

This thesis, in its first two chapters, reports an overview of the physical mechanisms on the basis on the photovoltaic effect and the main features of a standard solar cell, such as the figures of merit (FOMs) and recombination mechanisms. Moreover, it underlies the basic concepts of TCAD numerical simulation of silicon-based solar cells, including the optical and electrical methods adopted.

From chapter 4 to chapter 6 the main results of the thesis are reported and discussed in detail. The main findings and achievements of each capter are summarized afterwards.

Chapter 4 presents a 3-D numerical simulation flow that allows to reproduce the measured dark and illuminated (1-sun) J–V characteristics of a novel cell scheme, conceived for concentrator photovoltaic applications, based on the EWT concept, the EWT-DGB solar cell fabricated by FBK. The main advantages of EWT-DGB solar cell with respect to a simpler PESC can be summarized in terms of better IR response, low sensitivity to wafer resistivity and quality. A comparison between EWT-DGB and the simpler PESC solar cells under concentrated light (section 4.3) is reported, exploiting the results of an experimental characterization carried out in the range 1–200 suns. A maximum conversion efficiency of 21.4% at 44 suns has been experimentally observed for the EWT-DGB cell. By exploiting TCAD simulations, the FOMs of the PESC and of EWT-DGB cells have been studied by removing the limitations due to the process non-idealities, still maintaining realistic assumptions on physical and electrical parameters. Simulations result in an efficiency close to 24% at 100 suns and to 25% at 50 suns for PESC and EWT-DGB, respectively. Thanks to the modeling activity it can be concluded that EWT-DGB solar cell is suitable for low CF values, in the 10 to 60 sun range, and that its conversion efficiency is rather insensitive to the defect density of adopted substrate.

Chapter 5 outlines an accurate simulation study carried out by using physical models calibrated on the basis of experimental data, aimed at understanding the electrical properties of front junction (FJ) silicon solar cells featuring top/rear poly-Si/SiO_x selective contacts. Furthermore, a rear junction (RJ) design which desensitizes the FF to top electrode resistivity is proposed. In the case of a FJ design, it has been observed that, although J_{SC} and V_{OC} benefit from the absence of TCO, FF is critically influenced by front electrode conductibility. FF degradation can be mitigated by increasing either the poly-Si layers thickness or doping concentration, but TCO is suggested to attain acceptable efficiency. Increased doping concentration in poly-Si may result both in a better high-low junction and in a decrease in resistive losses. When a RJ design is adopted, the presence of a front surface field reduces the lateral transport in the front poly-Si layer, therefore, in case of sufficiently doped poly-Si, the RJ design is more insensitive to TCO properties with respect to the FJ design. This enables higher conversion efficiency combining the lower costs of an industrial type solar cell based on carrier-selective contacts. Conversion efficiency above 23% is obtainable without considering further improvements deriving from using fine-line metallization technology as well as smart wire interconnection.

Chapter 6 reports three comprehensive simulation studies investigating advanced options applicable in standard high-efficiency silicon solar cells, developed in collaboration with Applied Materials Italia.

The first one, section 6.1, concerns the impact of a passivated base in MWT solar cells exploiting a RPC scheme. A numerical simulation methodology which allows to study three-dimensional geometries without requiring cpu and memory intensive simulations is described. The proposed simulation flow allows to straightforwardly carrying out analyses of the impact of different geometrical and process parameters on saturation current density and on main figures of merit. Simulations show that the passivated base may substantially enhance the conversion efficiency (above 20%) with a maximum increase from 1.07 to $1.33\%_{\mathrm{abs}}$ with respect to baseline counterparts depending upon the substrate resistivity and the substrate thickness. The performed analyses highlight that the RPC option in the case of higher resistive substrates MWT solar cells is less effective in terms of efficiency enhancement with respect to the baselines. In addition, a comparison between two different holes diameter has been considered. It can be concluded that for relatively low values of contact fraction smaller hole diameters are preferred with respect to larger ones.

The section 6.2 regards the analysis of PERC solar cells, subjected to a Current-Induced Degradation process up to 16 hours where the performance are monitored at different intervals. Starting from the experimental data, in order to reproduce the measured values for each step of the both degradation and regeneration processes, a numerical simulation flow is performed by using a TCAD standard simulator. In particular, the concentrations of two trap levels (representative of recombination losses in bulk region and of Boron-Oxygen complexes, respectively) are properly tuned on the basis of each single process condition that has been applied to the cell in order to reproduce the measured data. It can be concluded that the adopted trap-model, in combination with a tuning of an equivalent carrier lifetime in the space charge region, correctly reproduce the influence of the degradation/regeneration processes on the FOMs of the presented solar cells.

Lastly, section 6.3 outlines the study of the impact of geometries and optical properties of the materials on effective optical shading in the case of encapsulated industrial silicon solar cells adopting multi-wire scheme. Simulations reveal that the effective shading factor, the enhancement of efficiency and paste saving are strongly dependent on the geometries of the encapsulant as well as on the optical reflectivity of the cell front interface. It has been demonstrated that multi-wire schemes take advantage of higher diameters, especially for coverage fraction lower than 20%. The calculated values of effective optical shading factor is 0.22 for coverage fraction up to 3% independently of the wire diameter and 0.46 for lower wire diameter and coverage fraction equal to 10%. It can be noticed that the efficiency enhancement of the multi-wire cell with respect to the busbar option depends on wire diameter, fingers width and number of busbar of the baseline. An absolute enhancement of efficiency up to $0.5\%_{\mathrm{abs}}$ with respect to the 3 busbar design and a paste saving up to 50 mg in case of multi-wire design are calculated for the given cell design.

Bibliography

[1] International Energy Agency, Paris, France. Key World Energy Statistics, 2017.

[2] Fraunhofer Institute for Solar Energy Systems, ISE, Freiburg, Germany. Photovoltaics Report (July), 2017.

[3] Solar Power Europe. Global Market Outlook for Solar Power, 2017.

[4] Bloomberg New Energy Finance, 2017.

[5] National Centre for Photovoltaic *http://www.nrel.gov/*.

[6] M.A. Green, Y. Hishikawa, W. Warta, E.D. Dunlop, D.H. Levi, J. Hohl-Ebinger, A.W.H. Ho-Baillie. Solar cell efficiency tables (Version 50). *Progress in Photovoltaics: Research and Applications*, v. 25, pp. 668-676, 2017.

[7] K. Yoshikawa, H. Kawasaki, W. Yoshida, T. Irie, K. Konishi, K. Nakano, T. Uto, D. Adachi, M. Kanematsu, H. Uzu, K. Yamamoto. Silicon heterojunction solar cell with interdigitated back contacts for a photoconversion efficiency over 26%. *Nature Energy*, v. 2, pp. 17032, 2017.

[8] A. Louwen, W.G.J.H.M. van Sark, R. Schropp, A. Faaij. A cost roadmap for silicon heterojunction solar cells. *Solar Energy Materials and Solar Cells*, v. 197, pp. 295-314, 2016.

[9] P. Altermatt. Models for numerical device simulations of crystalline silicon solar cells-A review. *Journal of Computational Electronics*, v. 10, pp. 314–330, 2011.

[10] A. Fell, K.R. McIntosh, P.P. Altermatt, G.J.M. Janssen, R. Stangl, A. Ho-Baillie, H. Steinkemper, J. Greulich, M. Müller, B. Min, K.C. Fong, M. Hermle, I.G. Romijn, M.D. Abbott. Input Parameters for the Simulation of Silicon Solar Cells in 2014. *IEEE Journal of Photovoltaics*, v. 5, pp. 1250-1263, 2015.

[11] M. A. Green. SOLAR CELLS Operating Principles, Technology and System Applications. Kensington, N.S.W.: The University of New South Wales, 1998.

[12] Internationale Energy Agency Solar Energy Perspective, Renewable Energy Technologies, 2011.

[13] *www.pveducation.org.*

[14] W. Shockley, H.J. Queisser. Detailed Balance Limit of Efficiency of pn Junction Solar Cells, *Journal of Applied Physics*, v. 32, pp. 510, 1961.

[15] A. Goetzberger, J. Knobloch, and B. Voss. Crystalline Silicon Solar Cells. John Wiley, 1998.

[16] F. Feldmann, M. Nicolai, R. Mueller, C. Reichel, M. Hermle. Optical and electrical characterization of poly-Si/SiO$_\mathrm{x}$ contacts and their implications on solar cell design. *Energy Procedia*, v. 124, pp. 31-37, 2017.

[17] K.R. McIntosh, P.P. Altermatt, G. Heiser. Depletion-region recombination: when does m$_\mathrm{DR}$ = 2?. In *Proc. 16th European Photovoltaic Solar Energy Conference Exhibition*, pp. 2500–253, 2000.

[18] K.R. McIntosh. Lumps, humps and bumps: Three detrimental effects in the current-voltage curve of silicon solar cells. Ph.D. dissertation. Univ. New South Wales, Sydney, Australia, 2001.

[19] V. Khanna, B.K. Das, D. Bisht, Vandana, P.K. Singh. A three diode model for industrial solar cells and estimation of solar cell parameters using PSO algorithm. *Renewable Energy*, v. 78, pp. 105-113, 2015.

[20] B. Thaidigsmann, J. Greulich, E. Lohmüller, S. Schmeißer, F. Clement, A. Wolf, D. Biro, R. Preu. Loss analysis and efficiency potential of p-type MWT-PERC solar cells. *Solar Energy Materials and Solar Cells*, v. 106, pp. 89–94, 2012.

[21] J.M. Gee, W.K. Schubert, P.A. Basore. Emitter Wrap-Through solar cell. In: *Proceedings 23rd IEEE Photovoltaic Specialists Conference*, Louisville, KY, May 1993.

[22] C. Ulzhöfer, S. Hermann, N.P. Harder, P.P. Altermatt, R. Brendel. The origin of reduced fill factors of emitter-wrap-through-solar cells. *Physica status solidi RRL*, v. 2, pp. 251-253, 2008.

[23] B. Thaidigsmann, M. Linse,A. Wolf, F. Clement, D. Biro, R. Preu. The path to industrial production of highly efficient metal wrap through silicon solar cells. *Green*, v. 2, pp. 171–176, 2012.

[24] M. Hendrics, B. Thaidigsmann, T. Fellmeth, S. Nold, A. Spribille, P. Hermann, M. Mittag, I. Hädrich, U. Eitner, F. Clement, D. Biro, R. Preu. Cost-optimized metallization layout for metal wrap through (MWT) solar cells and modules. In: *Proceedings of the 28th European photovoltaic solar energy conference and exhibition*, Paris, pp. 1524–1528, 2013.

[25] M.W.P.E. Lamers, C. Tjengdrawira, M. Koppes, I.J. Bennet, E.E. Bende, T.P. Visser, E. Kossen,B. Brockholz, A.A. Mewew, I.G. Romijn, E. Sauar, L. Carnel, S. Julsrud, T. Naas, P.C. de Jong, A.W. Weeber. 17.9% Metal-wrap-through mc-Si cells resulting in module efficiency of 17.0%. *Progress in Photovoltaics: Research and Applications*, v. 20, pp. 62–73, 2012.

[26] P. Magnone, D. Tonini, R. De Rose, M. Frei, F. Crupi, E. Sangiorgi, C. Fiegna. Numerical simulation and modeling of resistive and recombination losses in MWT solar cells. *IEEE Journal of Photovoltaics*, v. 3, pp. 1215–1221, 2013.

[27] E. Franklin, K. Fong, K. McIntosh, A. Fell, A. Blakers, T. Kho, D. Walter, D. Wang, N. Zin, M. Stocks, E.C. Wang, N. Grant, Y. Wan, Y. Yang, X. Zhang, Z. Feng, P.J. Verlinden. Design, fabrication and characterisation of a 24.4% efficient interdigitated back contact solar cell. *Progress in Photovoltaics: Research and Applications*, v. 24, pp. 411-427, 2016.

[28] P. Ortega, E. Calle, G. von Gastrow, P. Repo, D. Carrio, H. Savin, R. Alcubilla. High-efficiency black silicon interdigitated back contacted solar cells on p-type and n-type c-Si substrates. *Progress in Photovoltaics: Research and Applications*, v. 23, pp. 1448–1457, 2015.

[29] P. Procel, A. Ingenito, R. De Rose, S. Pierro, F. Crupi, M. Lanuzza, G. Cocorullo, O. Isabella, M. Zeman. Opto-electrical modelling and optimization study of a novel IBC c-Si solar cell.*Progress in Photovoltaics: Research and Applications*, v. 25, pp. 452-469, 2017.

[30] K. Masuko, M. Shigematsu, T. Hashiguchi, D. Fujishima, M. Kai, N. Yoshimura, T. Yamaguchi, Y. Ichihashi, T. Mishima, N. Matsubara, T. Yamanishi, T. Takahama, M. Taguchi, E. Maruyama, S. Okamoto. Achievement of More Than 25% Conversion Efficiency With Crystalline Silicon Heterojunction Solar Cell. *IEEE Journal of Photovoltaics*, v. 4, pp. 1433-1435, 2014.

[31] J. Nakamura, N. Asano, T. Hieda, C. Okamoto, H. Katayama, K. Nakamura. Development of heterojunction back contact Si solar cells. *IEEE Journal of Photovoltaics*, v. 4, pp. 1491–1495, 2014.

[32] C. Reichel, F. Granek, M. Hermle, S.W. Glunz. Back-contacted back-junction n-type silicon solar cells featuring an insulating thin film for decoupling charge carrier collection and metallization geometry. *Progress in Photovoltaics: Research and Applications*, v. 21, pp. 1063–1076, 2013.

[33] G.T. Yang, A. Ingenito, O. Isabella, M. Zeman. IBC c-Si solar cells based on ion-implanted poly-silicon passivating contacts. *Solar Energy Materials and Solar Cells*, v. 58, pp. 84-90, 2016.

[34] C. Reichel, F. Feldmann, R. Müller, R.C. Reedy, B.G. Lee, D.L. Young, P. Stradins, M. Hermle, S.W. Glunz. Tunnel oxide passivated contacts formed by ion implantation for applications in silicon solar cells. *Journal of Applied Physics*, v. 118, n. 205701, 2015.

[35] ITPRV 8th edition - report release and key findings, PV CellTEch conference, Malaysia, 2017.

[36] Trina Solar Press Release. Trina Solar Announces New Efficiency Record of 22.61% for Mono-Crystalline Silicon PERC Cell, 2016.

[37] M. Taguchi, A. Yano, S. Tohoda, K. Matsuyama, Y. Nakamura, T. Nishiwaki, K. Fujita, E. Maruyama. 24.7% record efficiency HIT solar cell on thin silicon wafer. *IEEE Journal of Photovoltaics*, v. 4, pp. 96–99, 2014.

[38] Photovoltaics and thin fil, electronics laboratory PV-LAB, Silicon-based heterojunction solar cells, EPFL, 2017.

[39] F. Feldmann, M. Bivour, C. Reichel, M. Hermle, S.W. Glunz. Passivated rear contacts for high-efficiency n-type Si solar cells providing high interface passivation quality and excellent transport characteristics. *Solar Energy Materials and Solar Cells*, v. 120, pp. 270-274, 2014.

[40] A. Ingenito, G. Limodio, P. Procel, G. Yang, H. Dijkslag, O. Isabella, M. Zeman. Silicon Solar Cell Architecture with Front Selective and Rear Full Area Ion-Implanted Passivating Contacts. *Solar RRL*, v .1, 2017.

[41] Y. Tao, E.L. Chang, A. Upadhyaya, B. Roundaville, Y.-.W. Ok, K. Madani, C.-.W. Chen, K. Tate, V. Upadhyaya, F. Zimbardi, J. Keane, A. Payne, A. Rohatgi. 730 mV implied Voc enabled by tunnel oxide passivated contact with PECVD grown and crystallized n+ polycrystalline Si. In: *Proceedings of 42nd IEEE Photovoltaic Specialist Conference*, New Orleans, LA, 2015.

[42] J. B. Heng, J. Fu, B. Kong, Y. Chae, W. Wang, Z. Xie, A. Reddy, K. Lam, C. Beitel, C. Liao, C. Erben, Z. Huang, Z. Xu. >23% High-Efficiency Tunnel Oxide Junction Bifacial Solar Cell With Electroplated Cu Gridlines. In: *IEEE Journal of Photovoltaics*, v. 5, pp. 82-86, 2015.

[43] R. Peibst, Y. Larionova, S. Reiter, M. Turcu, R. Brendel, D. Tetzlaff, J. Krügener, T. Wietler, U. Höhne, J.-D. Kähler, H. Mehlich, S. Frigge. Implementation of N+ and P+ polo junctions on front and rear side of double-side contacted industrial silicon solar cells. In: *Proceedings of 32nd European Photovoltaic Solar Energy Conference. Exhibition*, 2016.

[44] Y. Ohshita, T. Kamioka, K. Nakamura. Technology Trend of High Efficiency Crystalline Silicon Solar Cells. *Association of Asia Pacific Physical Societies*, v. 27, 2017.

[45] S.W. Glunz, F. Feldmann, A. Richter, M. Bivour, C. Reichel, H. Steinkemper, J. Benick, M. Hermle. The irresistible charm of a simple current flow pattern—25% with a solar cell featuring a full-area back contact. In *Proceedings of 31st European Photovoltaic Solar Energy Conference and Exhibition*, Hamburg, Germany, 2015, pp. 259–263.

[46] A. Richter, J. Benick, F. Feldmann, A. Fell, M. Hermle, S.W. Glunz. n-Type Si Solar Cells with Passivated Electron Contact: Identifying Sources for Efficiency Limitations by Wafer Thickness and Resistivity Variation. *Solar Energy Materials and Solar Cells*, v. 173, pp. 95-105, 2017.

[47] R.M. Swanson. The promise of concentrators. *Progress in Photovoltaics: Research and Applications*, v. 8, pp. 93-111, 2000.

[48] Y. Xing, P. Han, S. Wang, P. Liang, S. Lou, Y. Zhang, S. Hu, H. Zhu, C. Zhao, Y. Mi. A review of concentrator silicon solar cells. Renewable and Sustainable Energy Reviews, v. 51, pp. 1697–1708, 2015.

[49] G. Paternoster. Silicon Concentrator Solar Cells: Fabrication, Characterization and Development of Innovative Designs. *Ph.D Dissertation*, University of Trento, 2013.

[50] G. Paternoster, M. Zanuccoli, P. Bellutti, L. Ferrario, F. Ficorella, C. Fiegna, P. Magnone, F. Mattedi, E. Sangiorgi. Fabrication, characterization and modeling of a silicon solar cell optimized for concentrated photovoltaic applications. *Solar Energy Materials and Solar Cells*, v. 134, pp. 407–416, 2015.

[51] A. Slade, V. Garboushian. 27.6% efficient silicon concentrator solar cells for mass production. In: *Proceedings 15th International Photovoltaic Science and Engineering Conference*, Shanghai, China, p. 701, 2015.

[52] Sentaurus TCAD, Release C-2009.06, Synopsys, Zürich, Switzerland.

[53] Sentaurus TCAD, Release G-2012.06, Synopsys, Zürich, Switzerland.

[54] Sentaurus TCAD, Release J-2014.09, Synopsys, Zürich, Switzerland.

[55] Sentaurus TCAD, Release L-2016.03, Synopsys, Zürich, Switzerland.

[56] H. Haug, J. Greulich, A. Kimmerle, E. S. Marstein. PC1Dmod 6.1 - state-of-the-art models in a well-known interface for improved simulation of Si solar cells. *Solar Energy Materials and Solar Cells*, v. 142, pp. 47–53, 2015.

[57] A. Fell, K.R. McIntosh, M. Abbott and D. Walter. Quokka version 2: selective surface doping, luminescence modeling and data fitting. *23rd International Photovoltaic Science and Engineering Conference*, Taipei, 2013.

[58] R. Varache, C. Leendertz, M. Gueunier-Farret, J. Haschke, D. Munoz, L. Korte. Investigation of selective junctions using a newly developed tunnel current model for solar cell applications. *Solar Energy Materials and Solar Cells*, v. 141, pp. 14–23, 2015.

[59] A. Fell, K.C. Fong, K.R. McIntosh, E. Franklin and A.W. Blakers. 3-D simulation of interdigitated-back-contact silicon solar cells with Quokka including perimeter losses. *IEEE Journal of Photovoltaics*, v. 4, pp. 1040–1045, 2014.

[60] M.A. Green. SILICON SOLAR CELLS - Advanced Principles and Practice. Sydney, N.S.W.: Centre for Photovoltaic Devices and Systems, University of New South Wales, 1995.

[61] R.A. Smith. Semiconductors. Cambridge University Press, New York, USA, 2nd edition, 1978.

[62] S.C. Baker-Finch, K.R. McIntosh, D. Yan, K.C. Fong, T.C. Kho. Near-infrared free carrier absorption in heavily doped silicon. *Journal of Applied Physics*, v. 116, 2014.

[63] B.T. Phong. Illumination of computer generated pictures. *Communications of the ACM*, v. 18, pp. 311–317, 1975.

[64] H.A. Macleod. Thin-film optical filters. Adam Hilger Ltd, Bristol, UK, 2nd edition, 1986.

[65] A. Schenk. Finite-temperature full random-phase approximation model of band gap narrowing for silicon device simulation. *Journal of Applied Physics*, v. 84, pp. 3684–3695, 1998.

[66] K. Misiakos, D. Tsamakis. Accurate measurements of the silicon intrinsic carrier density from 78 to 340 K. *Journal of Applied Physics*, v. 74, pp. 3293-3297, 1993.

[67] S.E. Swirhun, J.A. del Alamo, R.M. Swanson. Measurement of Hole Mobility in Heavily Doped n-Type Silicon. *IEEE Electron Device Letters*, v. 32, pp. 168-171, 1986.

[68] J.A. del Alamo, R.M. Swanson. Measurement of Steady-State Minority-Carrier Transport Parameters in Heavily Doped n-Type Silicon. *IEEE Transaction on Electron Devices*, v. 34, pp. 1580-1589, 1987.

[69] P.P. Altermatt, A. Schenk, F. Geelhaar, G. Heiser. Reassessment of the intrinsic carrier density in crystalline silicon in view of band-gap narrowing. *Journal of Applied Physics*, v. 93, pp. 1598-1604, 1991.

[70] D. Klaassen. A unified mobility model for device simulation: I. Model equations and concentration dependence. *Solid State Electronics*, v. 35, pp. 953–959, 1992.

[71] D. Klaassen. A unified mobility model for device simulation: II. Temperature dependence of carrier mobility and lifetime. *Solid State Electronics*, v. 35, pp. 961–972, 1992.

[72] H. Steinkemper, F. Feldmann, M. Bivour, M. Hermle. Numerical Simulation of Carrier-Selective Electron Contacts Featuring Tunnel Oxides. *IEEE Journal of Photovoltaics*, v. 5, pp. 1348-1356, 2015.

[73] F. Feldmann, R. Müller, C. Reichel, M. Hermle. Ion implantation into amorphous Si layers to form carrier-selective contacts for Si solar cells. *Physica status solidi – Rapid Research Letters*, v. 8, pp. 767-770, 2014.

[74] F. Feldmann, M. Bivour, C. Reichel, H. Steinkemper, M. Hermle, S.W. Glunz. Tunnel oxide passivated contacts as an alternative to partial rear contacts. *Sol. Energy Mater. Sol. Cells*, v. 131, pp. 46-50, 2014.

[75] F. Feldmann, M. Simon, M. Bivour, C. Reichel, M. Hermle, S.W. Glunz. Efficient carrier-selective p- and n-contacts for Si solar cells. *Solar Energy Materials and Solar Cells*, v. 131, pp. 100–104, 2014.

[76] F. Feldmann, M. Bivour, C. Reichel, M. Hermle, S.W. Glunz. Passivated rear contacts for high-efficiency n-type Si solar cells providing high interface passivation quality and excellent transport characteristics. *Solar Energy Materials and Solar Cells*, v. 120, pp. 270-274, 2014.

[77] R. Peibst, U. Römer, Y. Larionova, M. Rienäcker, A. Merkle, N. Folchert, S. Reiter, M. Turcu, B. Min, J. Krügener, D. Tetzlaff, E. Bugiel, T. Wietler, R. Brendel. Working principle of carrier selective poly-Si/c-Si junctions: Is tunnelling the whole story?. *Solar Energy Materials and Solar Cells*, v. 158, pp. 60-67, 2016.

[78] G. Paternoster, M. Nicolai, G. de Ceglia, M. Zanuccoli, P. Bellutti, L. Ferrario, E. Sangiorgi, C. Fiegna. Fabrication, simulation and experimental characterization of EWT solar cells with deep grooved base contact. *IEEE Journal of Photovoltaics*, v. 6, pp. 1072-1079, 2016.

[79] M. Nicolai, G. Paternoster, M. Zanuccoli, G. de Ceglia, P. Bellutti, L. Ferrario, E. Sangiorgi, C. Fiegna. Analysis of the EWT-DGB solar cell at low and medium concentration and comparison with a PESC architecture. *Progress in Photovoltaics: Research and Applications*, v. 25, pp. 417-430, 2017.

[80] M. Nicolai, M. Zanuccoli, G. Paternoster, G. de Ceglia, L. Ferrario, P. Bellutti, E. Sangiorgi, C. Fiegna. Numerical Simulation and Experimental Characterization of Emitter Wrap through Solar Cells with Deep Grooved Base Contact (EWT-DGB). *Energy Procedia*, v. 92, pp. 160-169, 2016.

[81] A. Luque, V. Andreev. Concentrator Photovoltaics. Springer-Verlag, 2007.

[82] S. P. Philipps, A. W. Bett, K. Horowitz, S. Kurtz. Current status of concentrator photovoltaic (CPV) technology. National Renewable Energy Laboratory, Golden, CO, USA, Technical Report NREL/TP-6A20-63196, 2015.

[83] J. E. Haysom, O. Jafarieh, H. Anis, K. Hinzer. Concentrated photovoltaics system costs and learning curve analysis. In: *Proceedings 9th International Conferefnce on Concentrated Photovoltaic Systems*, v. 1556, pp. 239-243, 2013.

[84] O. Fidaner, F.A. Suarez, M. Wiemer, V.A. Sabnis, T. Asano, A. Itou, D. Inoue, N. Hayashi, H. Arase, A. Matsushita, T. Nakagawa. High efficiency micro solar cells integrated with lens array. *Applied Physics Letters*, v. 104, n. 10, p. 103902, 2014.

[85] D.S. Ruby, P.A. Basore, M. E. Buck, J. M. Gee, W. K. Schubert, H.L. Tardy. Simplified processing for 23%- efficient silicon concentrator solar cells. In: *Proceedings of 23rd IEEE Photovoltaic Specialist Conference PVSC*, 1993; pp. 172–177.

[86] P. Morvillo, E. Bobeico, F. Formisano, F. Roca. Influence of metal grid patterns on the performance of silicon solar cells at different illumination levels. *Materials Science and Engineering B*, v. 159, pp. 318–321, 2009.

[87] M.A. Green, K. Emery, Y. Hishikawa, W. Warta, E. D. Dunlop. Solar cell efficiency tables (Version 48). *Progress in Photovoltaics: Research and Applications*, v. 24, pp. 905–913, 2016.

[88] E. Van Kerschaver, G. Beaucarne. Back-contact Solar Cells: A Review. *Progress in Photovoltaics: Research and Applications*, v. 14, pp. 107-123, 2006.

[89] J.M. Gee, P. Kumar, J. Howarth, T. Schroeder, J. Franklin, J. Dominguez, D. Tanner. Development of industrial high-efficiency backcontact czochralski-silicon solar cells. *Progress in Photovoltaics: Research and Applications*, v. 19, pp. 887-893, 2011.

[90] N. Mingirulli, D. Stüwe, J. Specht, A. Fallisch, D. Biro. Screen-printed Emitter-Wrap-Through solar cell with single step side selective emitter with 18.8% efficiency. *Progress in Photovoltaics: Research and Applications*, v. 19, pp. 366-374, 2011.

[91] S. Hermann, A. Merkle, C. Ulzhöfer, S. Dorn, I. Feilhaber, M. Berger, T. Friedrich, T. Brendemühl, N.P. Harder, L. Ehlers, K. Weise, R. Meyer, R. Brendel. Progress in emitter wrap-through solar cell fabrication on boron doped Czochralski-grown silicon. *Solar Energy Materials and Solar Cells*, v. 95, pp. 1069-1075, 2011.

[92] F. Kiefer, C. Ulzhöfer, T. Brendemühl, N.P. Harder, R. Brendel, V. Mertens, S. Bordihn, C. Peters, J.W. Müller. High Efficiency N-type Emitter-Wrap-Through Silicon Solar Cells. *IEEE Journal of Photovoltaics*, v. 1, pp. 49-53, 2011.

[93] K. Faika, M. Wagner, P. Fath, E. Bucher. Simplification of EWT (emitter wrap-through) solar cell fabrication using Al-P-codiffusion. In: *Proceedings 28th Photovoltaic Specialists Conference (PVSC)*, pp. 260-263, 2000.

[94] N.P. Harder, S. Hermann, A. Merkle, T. Neubert, T. Brendemühl, P. Engelhart, R. Meyer, R. Brendel. Laser-processed high-efficiency silicon RISE-EWT solar cells and characterization. *Physica Status Solidi C*, v. 6, pp. 736-743, 2009.

[95] J. Cho, H. Lee, D. Hyun, Y. Lee, W. Jung, J. Hong. Efficiency enhanced emitter wrap-through (EWT) screen-printed solar cells with non-uniform thickness of silicon nitride passivation layer in via-holes. *Solar Energy*, v. 90, p. 188–194, 2013.

[96] D.D. Smith, J.M. Gee, M.D. Bode, J.C. Jimeno. Circuit Modeling of the Emitter-Wrap-Through Solar Cell. *IEEE Transaction on Electron Devices*, v.46, pp. 1993-1999, 1999.

[97] A. Fallisch, D. Biro. 2-D SPICE Simulation and Analytical Calculation of Spreading Resistance Effects in Emitter Wrap-Through Cells With Nonsquare Via-Hole Pattern. *IEEE Journal of Photovoltaics*, v.1, pp. 153-158, 2011.

[98] B. Benabadji, A. Zerga. Optimal design of buried emitter of EWT silicon solar cells type by numerical simulation. *Energy Procedia*, v. 44, pp. 126-131, 2014.

[99] M.M. Hilali, P. Hacke, J.M. Gee. Two-Dimensional Modeling of EWT Multicrystalline Silicon Solar Cells and Comparison with the IBC Solar Cell. *IEEE 4th World Conference on Photovoltaic Energy Conversion (WCPEC)*, pp. 1299-1303, 2006.

[100] A.H.Md. Ripon, A.A. Siddique, Sk.Md.G. Mustafa, A.B.M.R. Sazzad. Efficiency enhancement of solar cell: Fusion of texturisation and back contact Emitter-Wrap-Through modeling. *IEEE 32th International Conference on Distributed Computing Systems (ICDCS)*, pp. 264-267, 2012.

[101] C. Ulzhöfer, P.P. Altermatt, N.P. Harder, R. Brendel. Loss analysis of emitter-wrap-through silicon solar cells by means of experiment and three-dimensional device modeling. *Journal of Applied Physics*, v. 107, p. 104509, 2010.

[102] J. Schmidt, C. Berge, A.G. Aberle. Injection level dependence of the defect-related carrier lifetime in light-degraded boron-doped Czochralski silicon. *Applied Physics Letters*, v. 73, pp. 2167–2169, 1998.

[103] F. Wolny, T. Weber, M. Müller, G. Fischer. Light induced degradation and regeneration of high efficiency Cz PERC cells with varying base resistivity. *Energy Procedia*, v. 38, pp. 523–530, 2013.

[104] A. Herguth, R. Horbelt, S. Wilking, R. Job, G. Hahn. Comparison of BO regeneration dynamics in PERC and Al-BSF solar cells. *Energy Procedia*, v. 77, pp. 75–82, 2015.

[105] B. Sopori, P. Basnyat, S. Devayajanam, S. Shet, V. Mehta, J. Binns and J. Appel. Understanding light-induced degradation of c-Si solar cells. In: *Proceedings 38th IEEE Photovoltaic Specialists Conference*, Austin, TX, USA, pp. 3–8, 2012.

[106] S. Solmi, A. Parisini, R. Angelucci. Dopant and carrier concentration in Si in equilibrium with monoclinic SiP precipitates. *Physical Review B*, v. 53, pp. 7836–7841, 1996.

[107] R, De Rose, M. Zanuccoli, P. Magnone, M. Frei, E. Sangiorgi, C. Fiegna. Understanding the impact of the doping profiles on selective emitter solar cell by two-dimensional numerical simulation. *IEEE Journal of Photovoltaics*, v. 3, no. 1, pp. 159–167, 2013.

[108] R. De Rose, M. Zanuccoli, P. Magnone, E. Sangiorgi, C. Fiegna. Open issues for the numerical simulation of silicon solar cells. In: P*roceedings of 12th international conference on ultimate integration on silicon (ULIS)*, pp. 1–4, 2011.

[109] P. Magnone, R. De Rose, D. Tonini, M. Frei, M. Zanuccoli, A. Belli, M. Galiazzo, E. Sangiorgi, C. Fiegna. Numerical simulation on the influence of via and rear emitters in MWT solar cells. *IEEE Journal of Photovoltaics*, v. 4(4), pp. 1032–1039, 2014.

[110] R, De Rose, M. Zanuccoli, P. Magnone, E. Sangiorgi, C. Fiegna. Loss analysis of silicon solar cells by means of numerical device simulation. In: *Proceeding of 14th International Conference on Ultimate Integrate on Silicon*, pp. 205-208, 2013.

[111] M. Zanuccoli, R. De Rose, P. Magnone, M. Frei, H.W. Guo, M. Agrawal, E. Sangiorgi, C. Fiegna. Numerical simulation and modeling of rear point contact solar cells. In: *Proceedings of the 37th IEEE photovoltaic specialist conference*, pp. 1519–1523, 2010.

[112] M. Nicolai, M. Zanuccoli, P. Magnone, D. Tonini, E. Sangiorgi, C. Fienga. Theoretical study of the impact of rear interface passivation on MWT solar cells. *Journal of Computational Electronics*, v. 15, pp. 277-286, 2015.

---

[113] J. Dziewior, W. Schmid. Auger coefficients for highly doped and highly exited silicon. *Applied Physics Letters*, v. 31, pp. 346-348, 1977.

[114] S. Glunz, S. Rein, J. Lee, W. Warta. Minority carrier lifetime degradation in boron-doped Czochralski silicon. *Journal of Applied Physics*, v. 90, pp. 2397–2404, 2001.

[115] T. Trupke, M.A. Green, P. Würfel, P.P. Altermatt, A. Wang, J. Zhao, R. Corkish. Temperature dependence of the radiative recombination coefficient on intrinsic crystalline silicon. *Journal of Applied Physics*, v. 93, pp. 1598-1604, 2003.

[116] P.P. Altermatt, A. Schenk, F. Geelhaar, G. Heiser. Reassessment of the intrinsic carrier density in crystalline silicon in view on band-gap narrowing. *Journal of Applied Physics*, v. 93, pp. 1598-1604, 2003.

[117] M. Cid, N. Stem. Homogeneous Gaussian profile P+-type emitters: Updated parameters and metal-grid optimization. *Materials Research*, v. 5, pp. 427–432, 2002.

[118] M. Li, L. Zeng, Y. Chen, L. Zhuang, X. Wang, H. Shen. Realization of colored multicrystalline silicon solar cells with SiO_2 /SiN_x:H double layer antireflection coatings. *International Journal of Photoenergy*, v. 2013, Art. no. 352473, 2013.

[119] E. D. Palik, Handbook of Optical Constants of Solids. Orlando, FL, USA: Academic, 1998.

[120] S. Baker-Finch, K. R. McIntosh. Reflection of normally incident light from silicon solar cells with pyramidal texture. *Progress in Photovoltaics: Research and Applications*, v. 19, pp. 406–416, 2011.

[121] ASTM G159-98 ASTM Standard G173. Standard tables for reference solar spectral irradiances: direct normal and hemispherical on 37° tilted surface. *Annual Book of ASTM Standards*, v. 12.02, pp. 1–155, 2008.

[122] Z. Wang, P. Han, H. Lu, H. Qian, L. Chen, Q. Meng, N. Tang, F. Gao, Y. Jiang, J. Wu, W. Wu, H. Zhu, J. Ji, Z. Shi, A. Sugianto, L. Mai, B. Hallam, S. Wenham. Advanced PERC and PERL production cells with 20.3% record efficiency for standard commercial p-type silicon wafers. *Progress in Photovoltaics: Research and Applications* v. 20, pp. 260–268, 2012.

[123] M. Wolf, H. Rauschenbach. Series resistance effects on solar cell measurements. *Advanced Energy Conversion*, v. 3, pp. 455-479, 1963.

[124] P. J. Verlinden, M. Aleman, N. Posthuma, J. Fernandez, B. Pawlak, J. Robbelein, M. Debucquoy, K. Van Wichelen, J. Poortmans. Simple power-loss analysis method for high-efficiency interdigitated back contact (IBC) silicon solar cells. *Solar Energy Materials and Solar Cells*, v. 106, pp. 37-41, 2012.

[125] M. Nicolai, M. Zanuccoli, F. Feldmann, M. Hermle, C. Fiegna. Analysis of silicon solar cells with poly-Si/SiO_x carrier-selective base- and emitter-contacts. *IEEE Journal of Photovoltaics*, v. 8, pp. 103-109, 2018.

[126] M. Bivour, S. Schröer, M. Hermle, S.W. Glunz. Silicon heterojunction rear emitter solar cells: Less restrictions on the optoelectrical properties of front side TCOs. *Solar Energy Materials and Solar Cells*, v. 122, pp. 120-129, 2014.

[127] F. Feldmann, C. Reichel, R. Müller, M. Hermle, The application of poly-Si/SiO_x contacts as passivated top/rear contacts in Si solar. *Solar Energy Materials and Solar Cells*, v. 159, pp. 265-271, 2017.

[128] B. Nemeth, D. L. Young, M. R. Page, V. LaSalvia, S. Johnston, R. Reedy, P. Stradins. Polycrystalline silicon passivated tunneling contacts for high efficiency silicon solar cells. *Journal of Material Research*, v. 31, pp. 671-681, 2016.

[129] M.K. Stodolny, M. Lenes, Y. Wu, G.J.M. Janssen, I.G. Romijn, J.R.M. Luchies, L.J. Geerligs. n-Type polysilicon passivating contact for industrial bifacial n-type solar cells. *Solar Energy Materials and Solar Cells*, v. 158, pp. 24-28, 2016.

[130] U. Römer, R. Peibst, T. Ohrdes, B. Lim, J. Krügener, E. Bugiel, T. Wietler, R. Brendel. Recombination behavior and contact resistance of n+ and p+ poly-crystalline Si/monocrystalline Si junctions. *Solar Energy Materials and Solar Cells*, v. 131, pp. 85-91, 2014.

[131] M. Rienacker, M. Bossmeyer, A. Merkle, U. Römer, F. Haase, J. Krugener, R. Brendel, R. Peibst. Junction resistivity of carrier-selective polysilicon on oxide junctions and its impact on solar cell performance. *IEEE Journal of Photovoltaics*, v. 7 , pp. 11-18, 2017.

[132] Y. Liu, Y. Sun, W Liu and J. Yao. Novel high-efficiency crystalline-silicon-based compound heterojunction solar cells: HCT (heterojunction with compound thin-layer). *Physical Chemistry Chemical Physics*, v. 16, pp. 15400-15410, 2014.

[133] J.Y. Gan, R.M. Swanson. Polysilicon emitters for silicon concentrator solar cells. In: *Proceedings of 21st IEEE Photovoltaic Specialist Conference*, Kissimmee, EL, USA, 1990.

[134] A. Das, D.S. Kim, K. Nakayashiki, B. Rounsaville, V. Meemongkolkiat, A. Rohatgi. Boron Diffusion with Boric Acid for High Efficiency Silicon Solar Cells. *Journal of The Electrochemical Society*, v. 157, pp. 684-687, 2010.

[135] U. Römer, R. Peibst, T. Ohrdes, B. Lim, J. Krugener, T. Wietler, R. Brendel. Ion Implantation for Poly-Si Passivated Back-Junction Back-Contacted Solar Cells. *IEEE Journal of Photovoltaics*, v. 5, pp. 507-514, 2015.

[136] M.G. Young, H. Mohammed, L. Cousar, S.C. Pop, R. Schulze, J. Wang, D. Hutchings, S. Shumate. Modeling of the Hydrogen Selective Emitter for n-type Silicon Solar Cells. In: *Proceedings of 42nd IEEE Photovoltaic Specialist Conference*, New Orleans, LA, 2015.

[137] M. Zanuccoli, P. Magnone, E. Sangiorgi, C. Fiegna. Analysis of the impact of geometrical and technological parameters on recombination losses in interdigitated back-contact solar cells. *Solar Energy*, v. 116, pp. 37–44, 2015.

[138] Z. Holman, M. Filipic, A. Descoeudres, S. De Wolf, F. Smole, M. Topic, C. Ballif. Infrared light management in high-efficiency silicon heterojunction and rear-passivated solar cells. *Journal of Applied Physics*, v. 113, pp. 013107, 2013.

[139] N.C.-C. Lu, L. Gerzberg, C.-Y. Lu, J.D. Meindl. A Conduction Model for Semiconductor-Grain-Boundary-Semiconductor Barriers in Polycrystalline-Silicon Films. *IEEE Transactions on Electron Devices*, v. 30, pp. 137-149, 1983.

[140] S. Jin. Boron activation and diffusion in polycrystalline silicon with flash-assist rapid thermal annealing. *Ph.D Dissertation*, University of Florida, 2011.

[141] B. Lombos, S. Yee, M. Pietrantonio, M. Averous. Grain Boundaries Introduced Deep Levels IN Polysilicon. *Journal de Physique Colloques*, v. 43, pp. 199-206, 1982.

[142] A. Kumar, P.I. Widenborg, F. Law, H. Hidayat, G.K. Dalapati, A.G. Aberle, S. Jin. Study of Large-Grained n-Type Polycrystalline Silicon Thin Films made by the Solid Phase Crystallization Method. In: *Proceedings of 39th IEEE Photovoltaic Specialist Conference*, Tampa, FL, USA, 2013.

[143] A. Richter, S.W. Glunz, F. Werner, J. Schmidt, Andres Cuevas. Improved quantitative description of Auger recombination in crystalline silicon. *Physical Review B*, v. 86, pp. 1-4, 2012.

[144] J. del Alamo, J. van Meerbergen, F. D'Hoore, J.Nijs. High-low junctions for solar cell applications. *Solid-State Electronics*, v. 24, pp. 533-538, 1981.

[145] M. Nicolai, M. Zanuccoli, P. Magnone, D. Tonini, E. Sangiorgi, C. Fiegna. Theoretical study of the impact of rear interface passivation on MWT silicon solar cells. *Journal of Computational Electronics*, v. 15, pp. 277-286, 2016.

[146] M. Nicolai, M. Zanuccoli, M. Galiazzo, M. Bertazzo, E. Sangiorgi, C. Fiegna. Simulation Study of Light-induced, Current-induced Degradation and Recovery on PERC Solar Cells. *Energy Procedia*, v. 92, pp. 153-159, 2016.

[147] M. Nicolai, M. Zanuccoli, P. Magnone, M. Galiazzo, D. Tonini, M. Bertazzo, E. Sangiorgi, C. Fiegna. Simulation Study of Multi-wire front Contact Grids for Silicon Solar Cells. *Energy Procedia*, v. 77, pp. 129-138, 2015.

[148] E. VanKerschaver, R. Einhaus, J. Szlufcik, J. Nijs, R. Mertens. A novel silicon solar cell structure with both external polarity contacts on the back surface. In: *Proceedings of the 2nd world conference on photovoltaic energy conversion*, Wien, pp. 1479–82, 1998.

[149] M. Zanuccoli, R. De Rose, P. Magnone, E. Sangiorgi, C. Fiegna. Performance analysis of rear point contact solar cells by threedimensional numerical simulation. *IEEE Transactions on Electron Devices*, v. 59, pp. 1311–1319, 2012.

[150] B. Fischer. Loss analysis of crystalline silicon cells using photoconductance and quantum efficiency measurements. *Ph.D. dissertation*, University of Konstanz. Cuvillier, Chapter 2.3, 2003.

[151] J. Renshaw, M.H. Kang, V. Meemongkolkiat, A. Rohatgi, D. Carlson, M. Bennet. 3D-modeling of a back point contact solar cell structure with a selettive emitter. In: *Proceedings of 34th IEEE photovoltaic specialist conference PVSC*, pp. 375–379, 2009.

[152] A.G. Aberle, G. Heiser, M.A. Green. Two-dimensional numerical optimization study of the rear contact geometry of high efficiency silicon solar cells. *Journal of Applied Physics*, v. 75, pp. 5391–5405, 1994.

[153] P. Saint-Cast, M. Rüdiger, A. Wolf, M. Hofmann, J. Rentsch, R. Preu. Advanced analytical model for the effective recombination velocity of locally contacted surfaces. *Journal of Applied Physics*, v. 108, p. 013705, 2010.

[154] S. Lee. Cost effective process for high-efficiency solar cells. *Solar Energy*, v. 83, pp. 1285–1289, 2009.

[155] F. Khan, S.H. Baek, S. Singh, P. Singh, M. Husain, J.H. Kim. Influence of Al content on surface passivation properties of Al rich ZnO films for solar cell application. *Solar Energy*, v. 110, pp. 595–602, 2014.

[156] A.G. Aberle. Crystalline Silicon Solar Cells: Advanced Surface Passivation and Analysis. Centre for Photovoltaic Engineering. University of New South Wales, Sydney, 1999.

[157] M. Kim, D. Kim, D. Kim, Y. Kang. Impact of laser pulse width on laser ablation process of high performance PERC cells. *Solar Energy*, v. 110, 208–213, 2014.

[158] M. Kim, D. Kim, D. Kim, Y. Kang. Analysis of laser-induced damage during laser ablation process using picosecond pulse width laser to fabricate highly efficient PERC cells. *Solar Energy*, v. 108, pp. 101–106, 2014.

[159] T. Dullweber, S. Gatz, H. Hannebauer, T. Falcon, J. Schmidt, R. Brendel. 19.4% efficient large area rear-passivated screenprinted silicon solar cells. In: *Proceedings of the 26th European photovoltaic solar energy conference and exhibition*, pp. 811–816, 2011.

[160] J. Greulich, B. Thaidigsmann, S. Rein. Analysing the lateral series resistance of high-performance metal wrap through solar cells. *Solar Energy Materials and Solar Cells*, v. 124, pp. 24–30, 2014.

[161] J. Greulich. Simulation and characterization of novel large-area silicon solar cells for industrial production. *Ph.D. dissertation*, Fraunhofer-Institute for Solar Energy Systems ISE, Chapter 6, 2013.

[162] B. Thaidigsmann, A. Drews, T. Fellmeth, P. Saint-Cast, A. Wolf, F. Clement, R. Preu, D. Biro. Synergistic effects of rear-surface passivation and the metalwrap through concept. *IEEE Journal of Photovoltaics*, v. 2(2), pp. 109–112, 2012.

[163] B. Thaidigsmann, M. Hendrichs, S. Nold, E. Lohmüller, A. Wolf, F. Clement, D. Biro, R. Preu. P-Type MWT solar cells: current status and future expectations. In: *Proceedings of the 28th European photovoltaic solar energy conference and exhibition*, pp. 1099–1104, 2013.

[164] E. Lohmüller, B. Thaidigsmann, M. Popsischil, U. Jäger, S. Mack, J. Specht, J. Nekarda, M. Retzlaff, A. Krieg, F. Clement, A. Wolf, D. Biro, R. Preu. 20% Efficient passivated large-area metal wrap through solar cells on boron-doped Cz silicon. *IEEE Electron Device Letters*, v. 32(12), pp. 1719–1721, 2011.

[165] J. Rentsch, L. Gautero,A. Lemke, S. Eigner, M. Zimmer, F. Walter, M. Hofmann, R. Preu. Single side etching-Key technology for industrial high efficiency processing. In: *Proceedings of 23rd Europen photovoltaic solar energy Conference*, Velencia, 2008.

[166] P.P. Altermatt, S. Steingrube, Y. Yang, T. Dezhdar, S. Koc, B. Veith, S. Herman, R. Bock, K. Bothe, J. Schmidt, R. Brendel. Highly predictive modelling of entire Si solar cells for industrial applications. In: *Proceedings of 24th Europen Photovoltaic Solar Energy Conference Exhibition*, Hamburg, 2009.

[167] A. Wolf, D. Biro, J. Nekarda, S. Stumpp, A. Kimmerle, S. Mack, R. Preu. Comprehensive analytical model for locally contacted rear surface passivated solar cells. *Journal of Applied Physics*, v. 108, p. 124510, 2010.

[168] J.M. Lòpez-Gonzàlez, I. Martin, P. Ortega, A. Orpella, R. Alcubilla. Numerical simulations of rear point-contacted solar cells on 2.2 Ωcm p-type c-Si substrates. *Progress in Photovoltaics: Research and Applications*, v. 23, pp. 69–77, 2015.

[169] M. Zanuccoli, P.F. Bresciani, M. Frei, H.W. Guo, H. Fang, M. Agrawal, C. Fiegna, E. Sangiorgi. 2-D numerical simulation and modeling of monocrystalline selective emitter solar cells. In: *Proceedings of the 35th IEEE photovoltaic specialist conference*, pp. 2262–2265, 2010.

[170] G. Segev, A. Kribus. Performance of CPV modules based on vertical multi-junction cells under non-uniform illumination. *Solar Energy*, v. 88, pp. 120–128, 2013.

[171] A. Florakis, T. Janssen, J. Poortmans, W. Vandervorst. Process modeling for doped regions formation on high efficiency crystalline silicon solar cells. *Journal of Computational Electronics*, v. 13, pp. 95–107, 2014.

[172] G. Alì, F. Butera, N. Rotundo. Geometrical and physical optimization of a photovoltaic cell by means of a genetic algorithm. *Journal of Computational Electronics*, v. 13, pp. 323–328, 2014.

[173] M. Zanuccoli, I. Semenihin, J. Michallon, E. Sangiorgi, C. Fiegna. Advanced electro-optical simulation of nanowire-based solar cells. *Journal of Computational Electronics* v. 12, pp. 572–584, 2013.

[174] R. De Rose, M. Zanuccoli, P. Magnone, D. Tonini, M. Galiazzo, G. Cellere, M. Frei, H.W. Guo, C. Fiegna, E. Sangiorgi. 2-D numerical analysis of the impact of the highly-doped profile on selective emitter solar cell performance. In: *Proceedings of the 37th IEEE photovoltaic specialist conference*, pp. 2556–2559, 2011.

[175] A. Kimmerle, A. Wolf, U. Belledin, D. Biro. Modelling carrier recombination in highly phosphorous-doped industrial emitters. In: *Proceedings of the SiliconPV 2011 Conference, Energy Procedia*, v. 8, pp. 275–281, 2011.

[176] J. Greulich, N. Wöhrle, M. Glatthaar, S. Rein. Optical modeling of the rear surface roughness of passivated silicon solar cells. *Energy Procedia*, v. 27, pp. 234–239, 2012.

[177] B. Terheiden, T. Ballmann, R. Horbelt, Y. Schiele, S. Seren, J. Ebser, G. Hahn, V. Mertens, M.B. Koentopp, M. Scherff, W. Müller, Z.C. Holman, A. Descoeudres, S. De Wolf, S. Martin de Nicolas, J. Geissbuehler, C. Ballif, B. Weber, P. Saint-Cast, M. Rauer, C. Schmiga, S.W. Glunz, D.J. Morrison, S. Devenport, D. Antonelli, C. Busto, F. Grasso, F. Ferrazza, E. Tonelli, W. Oswald. Manufacturing 100-mm-thick silicon solar cells with efficiencies greater than 20% in a pilot production line. *Physica Status Solidi A*, v. 212, pp. 13–24, 2015.

[178] K.M. Broek, I.J. Bennett, M.J. Jansen, N.J.C.M. van der Borg, W. Eerenstein. Light and current induces degradation in p-type multicrystalline cells and development of an inspection method and a stabilization method. In: *Proceedings of 27th Europen Photovoltaic Solar Energy Conference Exhibition*, pp. 3167–3171, 2012.

[179] S. Wilking, J. Engelhardt, S. Ebert, C. Beckh, A. Herguth, G. Hahn. High speed regeneration of BO-defects: improving long-term solar cell performance within seconds. In: *Proceedings of 29th Europen Photovoltaic Solar Energy Conference Exhibition*, pp. 366-372, 2014.

[180] M. Martire, M. Bertazzo, M. Zamuner, M. Galiazzo. LID recovery tool for PERC solar cells. In: *Proceedings of 31th Europen Photovoltaic Solar Energy Conference Exhibition*, pp. 879-883, 2015.

[181] T. Mchelidze, J. Weber. Direct detection of carrier traps in Si solar cells after light-induced degradation. *Physica Status Solidi RRL*, v. 9, pp. 108-110, 2015.

[182] M. Zanuccoli, J. Michallon, I. Semenihin, C. Fiegna, A. Kaminski-Cachopo, E. Sangiorgi, V. Vyurkov. Numerical simulation of vertical silicon nanowires based heterojunction solar cells. *Energy Procedia*, v. 38, pp. 216-222, 2013.

[183] M. Zanuccoli, R. De Rose, P. Magnone, M. Frei, H.W. Guo, M. Agrawal, E. Sangiorgi, C. Fiegna. Numerical simulation and modeling of rear point contact solar cells. In: *Proceedings of 37th IEEE Photovoltaic Specialist Conference*, pp. 1519–1523, 2011.

---

[184] R. De Rose, K. Van Wichelen, L. Tous, J. Das, F. Dross, C. Fiegna, M. Lanuzza, E. Sangiorgi, A.U. De Castro, M. Zanuccoli. Optimization of rear point contact geometry by means of 3-D numerical simulation. *Energy Procedia* v. 27, pp. 197-202, 2012.

[185] P. Procel, V. Maccaronio, F. Crupi, G. Cocorullo, M. Zanuccoli, P. Magnone, C. Fiegna. Analysis of the impact of doping levels on performance of back contact – back junction solar cells. *Energy Procedia* v. 55, pp. 128-132, 2014.

[186] I. Semenikhin, M. Zanuccoli, M. Benzi, V. Vyurkov, E. Sangiorgi, C. Fiegna. Computational efficient RCWA method for simulation of thin film solar cells. *Optical and Quantum Electronics*, v. 44, pp. 149-154, 2012.

[187] H. Hannebauer, T. Dullweber, T. Falcon, X. Chen, R. Brendel. Record low Ag paste consumption of 67.7 mg with dual print. *Energy Procedia*, v. 43, pp. 66-71, 2013.

[188] S. Braun, G. Hahn, R. Nissler, C. Pönisch, D. Habermann. Multi-busbar solar cells and modules: high-efficiencies and low silver consumption. *Energy Procedia*, v. 38, pp. 334-339, 2013.

[189] S. Braun, R. Nissler, C. Ebert, D. Habermann, G. Hahn. High Efficiency Multi-busbar Solar Cells and Modules. *IEEE Journal of Photovoltaics*, v.4, pp. 148-153, 2014.

[190] R. Woehl, M. Hörteis, S.W. Glunz. Analysis of the Optical Properties of Screen-Printed and Aerosol-Printed and Plated Fingers of Silicon Solar Cells. *Advances in OptoElectronics*, Article ID 759340, 2008.

[191] A.W. Blakers. Low loss metallisation of solar cells. In: *Conference Record of the 23rd IEEE Photovoltaic Specialists Conference*, pp. 347-351, 1993.

[192] M. Paggi, M. Corrado, M.A. Rodriguez. A multi-physics and multi-scale numerical approach to microcracking and power loss in photovoltaic modules. *Composite Structure*, v. 95, pp. 630-638, 2013.

[193] Enki Technology, 2192 Bering Drive, San Jose, CA 9513, 2014.

[194] K.R. McIntosh, J.N. Cotsell, J.S. Cumpston, A.W. Norris, N.E. Powell, B.M. Ketola. An optical comparison of silicone and EVA encapsulants for conventional silicon PV modules: A ray-tracing study. *34th IEEE Photovoltaic Specialist Conference*, Philadelphia, pp. 544-549, 2009.

[195] M.A. Green. Ag requirements for silicon wafer-based solar cells. *Progress in Photovoltaics: Research and Applications*, v. 8, pp. 911-916, 2011.

[196] M.F. Stuckings, A.W. Blakers. A study of shading and resistive loss from the fingers of encapsulated solar cells. *Solar Energy Materials and Solar Cells*, v. 59, pp. 233-242, 1999.

Acknowledgments

In this final part, I want to express my gratitude to all the people who supported me during the last three years. I would like to thank my supervisor Prof. Claudio Fiegna for the opportunity of working toward the Ph.D. by joinining his research group. He has been always present with his expertise and with his precious advices. I am enormously grateful to my unofficial 'co-supervisor', Dr. Mauro Zanuccoli for his encouragement and for the fruitful dicussions. He shared with me each single step of my path.

A special thank to Prof. Paolo Magnone for his advices during the first part of my Ph.D. programme. During the doctorate period I have been honoured to collaborate with members of prestigious research groups who contributed to the success of the activities presented in this work: the groups of Dr. Giovanni Paternoster of Fondazione Bruno Kessler (FBK, Trento, Italy), of Ing. Marco Galiazzo of Applied Materials Italia s.r.l (AMAT, San Biagio di Callalta, Italy) and of Dr. Martin Hermle of Fraunhofer ISE (Freiburg, Grermany). Thanks to all of them. I had the opportunity to spent six months in a stimolating working environment: the Modeling and Characterization group of Fraunhofer ISE led by Prof. Stefan Glunz. I would like to thank Jonas Schön for the availability, Heiko Steinkemper and Frank Feldmann for their helpful knowledge-transfer and for their time. Last but not least, thanks to Ino Geisenmeyer for all that he did for me.

I dedicate this work, the spent time, and everything I learnt to my wonderful wife!

List of Abbreviations

1-D (2-D, 3-D)	One-dimensional (two-, three-)
a-Si	amorphous silicon
a-Si:H	hydrogenated amorphous silicon
Al-BSF	Aluminum-Back Surface Field
Al-p+	Aluminum-doped p+ silicon
AM	Air Mass
AM1.5D	Standard solar spectrum ("air mass 1.5 direct")
AM1.5G	Standard solar spectrum ("air mass 1.5 global")
AMAT	Applied Materials Italia s.r.l.
ARC	Anti-Reflection layer
AZO	Aluminum Zinc Oxide
B	Boron
BBs	Busbars
BC	Back contact
BC-BJ	Back contact back junction (solar cell)
BGN	Band gap narrowing
BSF	Back Surface Field
BSRV	Back Surface Recombination Velocity
BSRVeff	Effective Back Surface Recombination Velocity
BSRVpass	Back Surface Recombination Velocity at passivated interface
c-Si	crystalline silicon
CAGR	Compound annual growth rate
C_f	Coverage fraction
C_{fr}	Contact fraction
CF	Concentrator Factor
CID	Current Induced Degradation
CMOS	Complementary Metal–Oxide–Semiconductor
CPV	Concentrator Photovoltaic
Cz	Czochralski
DARC	Double-Anti-Reflection layer
DOS	density of states

DRIE	Deep reactive ion etching
ECV	Electrochemical capacitance-voltage
EQE	External Quantum Efficiency
EVA	Ethyl vinyl acetate
EWT	Emitter Wrap Through
EWT-DGB	Emitter Wrap Through with Deep Grooved Base
FBK	Fondazione Bruno Kessler
FC	Front Contact solar cell
FCA	Free carrier absorption
FDTD	Finite Difference Time Domain
FEM	Finite element method
FF	Fill factor
FJ	Front Junction
FOMs	Figures of merit
Fraunhofer ISE	Fraunhofer Institute for Solar Energy Systems
FSF	Front surface field
FZ	Floating Zone
HDOP	heavy and deep phosphorus diffusion
HE	Homogenous Emitter
HJ	Heterojunction
i:a-Si	intrinsic amorphous silicon
IBC	Interdigitated back contacts
IQE	Internal Quantum Efficiency
IR	Infra-red
ITO	Indium tin oxide
IV	Current-voltage
LBSF	Local back surface field
LDOP	lowly-doped and shallow diffusion
LFC	Laser Firing Contact
LID	Light Induced Degradation
LPCVD	Low-Pressure chemical vapor deposition
MPP	Maximum power point
MW	MultiWire
MWT	Metal Wrap Trhough
MWT-RPC	Metal Wrap Trhough Rear Point Contact
NREL	National Renewable Energy Laboratory
O	Oxygen
OC	Open-circuit
P	Phosphorus
PECVD	Plasma-enhanced chemical vapor deposition
PERC	Passivated Emitter and Rear Cell
PERL	Passivated Emitter, Rear Locally diffused cell

PESC	Passivated Emitter Solar Cell
poly-Si	Polysilicon
PV	Photovoltaic
QSSPC	Quasi-steady state photoconductance
RPC	Rear Point Contact
RJ	Rear Junction
SC	Short-circuit
SCR	Space charge region
SE	Selective Emitter
SEM	Scanning Electron Microscopy
SHJ	Silicon heterojunction
SIMS	Secondary ion mass spectrometry
SiN	Silicon Nitride
SRH	Shockley Read Hall
SRV	Surface Recombination Velocity
SLT	Single Level Trap
TCAD	Technology Computer-Aided Design
TCO	Transparent Conductive Oxide
TMF	Transfer matrix formalism
TMM	Transfer Matrix Method
TOPCon	Tunnel oxide passivated contact
UV	Ultraviolet

List of Symbols

Symbol	**Unit**	**Description**
A	[cm^2]	area of solar cell
α_{Si}	[cm^{-1}]	silicon absorption coefficient
α_{FCA}	[cm^{-1}]	absorption coefficient due to FCA
B	[cm$^{-3}\cdot$s^{-1}]	radiative recombination coefficient
c	[m$\cdot$s^{-1}]	speed of light in vacuum
$\mathrm{C_{fr}}$	[%]	metalization fraction
$\mathrm{C_n}$	[cm$^6\cdot$s^{-1}]	material-specific Auger coefficient for electrons
$\mathrm{C_p}$	[cm$^6\cdot$s^{-1}]	material-specific Auger coefficient for holes
$\mathrm{d_h}$	[μm]	p-hole depth (EWT-DGB solar cell), hole diameter (MWT-RPC)
$\mathrm{D_n}$	[cm$^2\cdot$s^{-1}]	diffusion coefficient for electrons
$\mathrm{D_p}$	[cm$^2\cdot$s^{-1}]	diffusion coefficient for holes
$\mathrm{d_{deg}}$	[μm]	thickness of test fixture
E	[eV]	electric field
ε	[eV]	level of energy
$\mathrm{E_C}$	[eV]	bottom edge of the conduction band
$\mathrm{E_g}$	[eV]	energy band-gap
$\mathrm{E_{ph}}$	[eV]	photon energy
$\mathrm{E_t}$, $\mathrm{E_{TRAP}}$	[eV]	energy trap level
$\mathrm{E_V}$	[eV]	top edge of the valence band
η	[%]	conversion efficiency
η_{C}	[%]	collection efficiency
ϕ	[photons $\cdot$ s^{-1} m^{-2}]	power flux
φ	[V]	electrostatic potential
G	[cm^{-3}]	optical generation rate
$\mathrm{G_L}$	[cm^{-3}]	local carrier generation rate
h	[J$\cdot$s]	Plank's constant
H	[μm]	finger height
$\mathrm{H_B}$	[μm]	busbar height
$\mathrm{h_s}$	[μm]	Hole spacing
$\mathrm{I_{mpp}}$	[A]	maximum power point current

I_{SC}	[A]	short circuit curent
I_0	[photons · s^{-1} m^{-2}]	incident power flux
J_{inc}	[fA/cm^2]	total incident current density
J_{PH}, J_L	[fA/cm^2]	photogenerated current density
J_{SC}	[mA/cm^2]	short circuit current density
J_T	[mA/cm^2]	saturation current density ascribed to the tunneling mechanism
J_0, J_H	[fA/cm^2]	saturation current density
k	[eV·K^{-1}]	Boltzman's constant
k_{deg}	[V/cm/K]	thermal conductivity of test fixture
L	[μm]	finger length
L_B	[μm]	busbar length
L_T	[μm]	transport length
λ	[nm]	wavelength
$m_{t,e}$	[-]	electrons effective tunneling mass
$m_{t,h}$	[-]	holes effective tunneling mass
m_0	[-]	electrons rest mass
μ	[cm^{2}V^{-1}s^{-1}]	carrier mobility
μ_{eff}	[cm^{2}V^{-1}s^{-1}]	effective carrier mobility
μ_{phon}	[cm^{2}V^{-1}s^{-1}]	phonon effect on carrier mobility
μ_{scatt}	[cm^{2}V^{-1}s^{-1}]	scattering effect on carrier mobility
ν	[Hz]	frequency
n_i	[cm^{-3}]	intrinsic carrier concentration
N_A	[cm^{-3}]	acceptor concentrations
N_D	[cm^{-3}]	donor concentrations
N_{INC}	[-]	Number of incident photons
N_{poly}	[cm^{-3}]	Poly-si doping concentration
N_S	[cm^{-3}]	doping concentration value at the interface
P_{in}	[W]	incident power
P_{Refl}	[W]	reflected power
P_{Tran}	[W]	transitted power
q	[C]	elementary charge
$q\phi_B$	[eV]	silicon work function
$q\phi_M$	[eV]	metal work function
$q\chi$	[eV]	silicon electron affinity
R	[%]	Reflectance
R_{AUG}	[cm^{-3}]	Auger recombination
R_{bus}	[Ωcm^2]	busbar resistance
R_{finger}	[Ωcm^2]	finger resistance
R_s, $R_{s,tot}$	[Ωcm^2]	series resistance
R_{SH}	[Ω/sq]	shunt resistance

$R_{s,fr}$	[Ωcm^2]	front surface contribution to series resistance
$R_{spreading}$	[Ωcm^2]	spreading resistance
R_{RAD}	[cm^{-3}]	Radiative recombination
ρ	[Ccm^{-3}]	local carrier density
ρ_C	[Ωcm]	contact resistivity
ρ_m	[Ωcm]	metal resistivity
ρ_s	[Ωcm]	substrate resistivity
S_e	[cm/s]	electrons surface recombination velocity
S_h	[cm/s]	holes surface recombination velocity
T	[K]	absolute temperature
T_P	[-]	tunneling probability
$t_{e,s}$	[μm]	emitter thickness
$t_{ENCAPSULANT}$	[μm]	glass thickness
t_{GLASS}	[cm]	encapsulant thickness
t_{poly}	[nm]	Poly-si thickness
τ_n	[μs]	effective minority carriers (electrons) lifetime
$\tau_{n\text{-}H}$	[μs]	n-hole effective lifetime (EWT-DGB solar cell)
U	[cm^{-3}s^{-1}]	recombination rate
${U_{SRH}}^{NET}$	[cm^{-3}s^{-1}]	recombination rate due to SRH mechanisms
${U_{rad}}^{NET}$	[cm^{-3}s^{-1}]	recombination rate due to radiative mechanisms
V_{mpp}	[V]	maximum power point voltage
v_{OC}	[V]	normalized open circuit voltage
V_{OC}	[V]	open circuit voltage
W_B	[μm]	busbar width
W	[μm]	finger width
W_{BASE}	[μm]	base contact width
W_{SPACE}	[μm]	space region width
$W_{spacing}$	[μm]	finger spacing